EFFECT OF MICROSTRUCTURE ON THE MECHANICAL PROPERTIES OF Ti_2AlC AT ROOM AND HIGH TEMPERATURES

A Dissertation

by

ROGELIO BENITEZ JR.

Submitted to the Office of Graduate and Professional Studies of
Texas A&M University
in partial fulfillment of the requirements for the degree of

DOCTOR OF PHILOSOPHY

Chair of Committee,	Miladin Radovic
Committee Members,	Anastasia Muliana
	Ibrahim Karaman
	Dimitris C. Lagoudas
Head of Department,	Andreas A. Polycarpou

August 2015

Major Subject: Mechanical Engineering

Copyright 2015 Rogelio Benitez Jr.

ABSTRACT

This study reports on the mechanical properties of Ti_2AlC systematically designed with various grain sizes and $TiAl_x$ impurity contents at room and elevated temperatures. Room temperature cyclic compressive testing of Ti_2AlC of the several microstructures was carried out in combination with resonant ultrasound spectroscopy (RUS) tests and post mortem electron backscatter diffraction (EBSD). Results show that the complex mechanical response of Ti_2AlC at room temperature can be divided in four stress regions with distinct underlying mechanisms: (a) Region I linear elastic behavior; (b) Region II in which stress strain hysteric behavior is observed due to reversible dislocation flow in the soft grains; (c) Region III in which accumulation of dislocation walls (DWs) result in cyclic hardening and lager hysteretic loops; (d) Region IV in which microcracking contributes additionally to the before mentioned deformation mechanisms. The transition stresses between regions were found to be strongly dependent on grain size, with coarse grain structures having lower transition stresses than fine grain size and with negligible effects of $TiAl_x$ on the transition stresses. In addition, EBSD analysis reveals that the microstructure evolves during loading through the formation of low angle grain boundaries that give rise to the observed strain hardening effects. Room temperature quasi-static tests show that the compressive strength follows a Hall-Petch relationship with the grain length, and not the thickness; an observation supported by the fact that only basal plane dislocations have been previously observed in MAX phases. The fine grain structures fabricated in this study exhibit the

highest strength reported to date Ti_2AlC. High temperature quasi-static compression testing shows that the compressive strength of the fine grain structures degrades more than the coarse grain structure, regardless of the presence of $TiAl_x$ intermetallic. Post-mortem EBSD analysis indicate texturing of individual grains for easy slip, more so in fine grain structures. This texturing contributes to the softening observed above the brittle to plastic transition temperature. Microvoid formation and grain refinement are also observed for both fine and coarse structures, with refinement in coarse grains occurring within the grains.

DEDICATION

To Rogelio Rene, Laurita and all my loving family.

ACKNOWLEDGEMENTS

I want to express my sincere gratitude to my advisor, Dr. Miladin Radovic for giving me the opportunity to participate in a fascinating project; for his guidance, continuous advice, and support during my years as a doctoral student.

I also want to thank my committee members Dr. Anastasia Muliana, Dr. Ibrahim Karaman and Dr. Dimitris C. Lagoudas for serving in my committee and for their helpful suggestions to my work.

My great appreciation also goes to Dr. Gwenaelle Proust and Wen H. Kan, University of Sydney, and to Australian Center for Microscopy and Microanalysis for their help with carrying out EBSD analysis.

Thanks to the members of my research group, Huili Gao, Morgan O'Neil, Peter Lovelace, Peipei Gao and Liangfa Hu for their help preparing samples and for providing assistance with XRD and SPS. Additionally, I want to thank Ankush Kothalkar for his meaningful discussions.

I express my sincere gratitude to Dr. Karen Lozano (UTRGV) and Dr. Arturo Fuentes (UTRGV) for their constant advice and the initial push I needed to pursue my PhD.

I acknowledge the Diversity Fellowship from Texas A&M, the GEM Fellowship, National Science Foundational (NSF) and Air Force Office of Scientific Research (AFOSR) for supporting my doctoral studies.

Last, but not least, I express my deepest gratitude to my family for their encouragement, support, prayers and patience during all these years. Thanks to my wife and my son, Laura and Rogelio Rene; my parents Rogelio and Minerva Benitez; my sister, nephew and niece, Madelin, Leonardo and Aranza Gonzalez; as well as my in-laws and my extended family. This achievement could have not been completed without any one of you.

This work was supported by the Air Force Office of Scientific Research (AFOSR) under grant FA9550-09-1-0686 and National Science Foundation Division of Civil, Mechanical, and Manufacturing Innovation (NSF-CMMI) under grant 1233792. The FE-SEM acquisition was supported in part by the National Science Foundation under Grant No. DBI-0116835. In addition, the author is also grateful for support of International Program Development Fund Fund and DVC Research/International Research Collaboration Award at the University of Sydney. The author acknowledges the facilities, and the scientific and technical assistance, of the Australian Microscopy & Microanalysis Research Facility at the University of Sydney, especially the assistance of Dr. Patrick Trimby, in assisting with the EBSD analysis.

NOMENCLATURE

Al	Aluminum
b	Burgers vector
BPTT	Brittle-to-Plastic Transition Temperature
BSE	Backscatter Electron
C	Carbon
CG	Coarse Grain
CP	Commercial Powder
CRSS	Critical Resolve Shear Stress
CS	Commercial Sample
D	Distance Between Dislocations
d_{AL-AL}	Distance Between Aluminum Layers
DP	Dislocation Pileup
DW	Dislocation Wall
E	Young's Modulus
EBSD	Electron Backscatter Diffraction
ECAS	Electric Current Assisted Sintering
EDM	Electrical Discharge Machining
EDS	Energy-Dispersive X-Ray Spectroscopy
EPSC	Elasto-Plastic Self-Consistent Model
FG	Fine Grain

G	Shear Modulus
GL	Gauge Length
GND	Geometric Necessary Dislocations
HAGBs	High Angle Grain Boundaries
IKB	Incipient Kink Band
IPF	Inverse Pole Figure
KB	Kink Band
K_{1C}	Fracture Toughness
KNE	Kinking Non-linear Elastic
LAGBs	Low Angle Grain Boundaries
l	Grain Length
L_o	Initial Length
M	Taylor Factor
MC	Microcracking Model
MG	Medium Grain Size
MDW	Mobile Dislocation Wall
RF	Reversible Flow Model
RP	Reacted Powder
RUS	Resonant Ultrasound Spectroscopy
SC	Sintered Composite
SEM	Scanning Electron Microscopy
SHPB	Split-Hopkins Pressure Bar

SHS/PHIP	Self-propagating High Temperature Combustion Synthesis with Pseudo Hot Isostatic Pressing
SPS	Spark Plasma Sintering
t	Grain Thickness
TEM	Transmission Electron Microscopy
Ti	Titanium
TiC	Titanium Carbide
UCS	Ultimate Compressive Strength
UHP	Ultra High Purity
v	Poisson's ratio
w	Dislocation Core Width
WC	Tungsten Carbide
W_d	Energy Dissipation per Unit Volume per Load-Unload Cycle
XCG	Extra Coarse Grain Size
XRD	X-ray Diffraction
γ_c	Critical Kinking Angle
ε_{NL}	Non-linear elastic strain
ε_{eff}	Effective Strain
ε_{ext}	Strain by Extensometer
θ	Maximum Misorientation Angle
$\Delta\varepsilon_{PL}$	Irrecoverable Plastic Strain
ρ_{dis}	Dislocation Density

σ	Stress (compressive)
σ_f	Fracture Stress
σ_t	Threshold Stress
σ_{th}	Theoretical Strength
$\sigma_{I\text{-}II}$	Transition Stress between Region I and Region II
$\sigma_{II\text{-}III}$	Transition Stress between Region II and Region III
$\sigma_{III\text{-}IV}$	Transition Stress between Region III and Region IV
τ_{PN}	Peierls-Nabarro Stress

TABLE OF CONTENTS

Page

LIST OF FIGURES

Page

LIST OF TABLES

Page

1 INTRODUCTION

MAX phases are ternary carbides and nitrides with nano-laminated hexagonal structure (space group *P63/mmc*) whose unique combination of metallic and ceramic-like properties have sparked great interest since the first MAX phase, namely Ti_3SiC_2, was synthesized in bulk [1-3]. In general, MAX phases are very appealing materials because they have high stiffness, strength, thermal shock resistance, electrical and thermal conductivity combined with low density, hardness, and ease of machinability [3, 4]. From more than 60+ different MAX phases, Ti_2AlC is considered one of the best candidates for high temperature applications because of its good mechanical properties, creep resistance, but above all because of its excellent oxidation resistance due to the formation of spallation-resistant self-healing layer of Al_2O_3 on surfaces exposed to air and water vapor [2, 4-13].

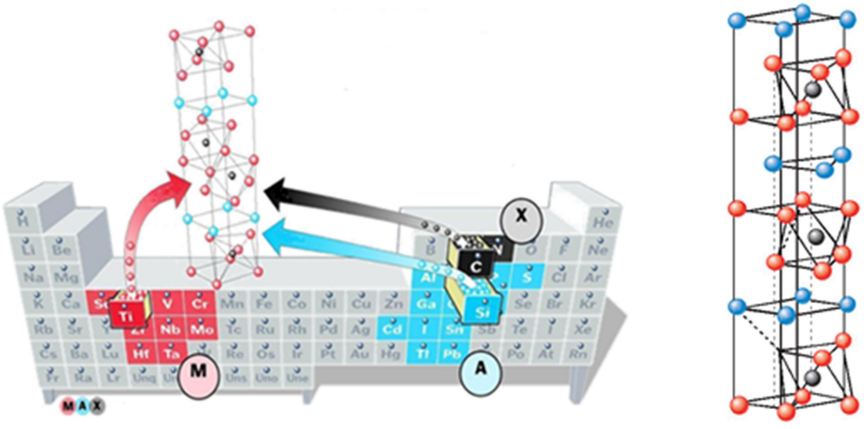

Figure 1-1: Possible elements that may be used to form MAX phases (left) and crystal structure of Ti_2AlC (right). Left image adapted from www.ltu.se and right reprinted from [4].

The unique mechanical properties of Ti_2AlC, and to the further extent of all other MAX phases, can be attributed to their plastically anisotropic nano-laminated structure, in which numerous dislocations form and easily glide only in the basal planes, at least at room temperature [14]. Furthermore, basal plane dislocations arrange themselves in pileups along slip plane or as dislocation walls normal to basal planes as can be seen in Figure 1-2. Consequently, MAX phases have fewer than five independent slip systems and therefore cannot behave as ductile materials in the classical sense [4]. However, what makes their mechanical behavior different from other inherently brittle solids is their ability to deform by buckling, kinking and kink band, KB, formation [15-18].

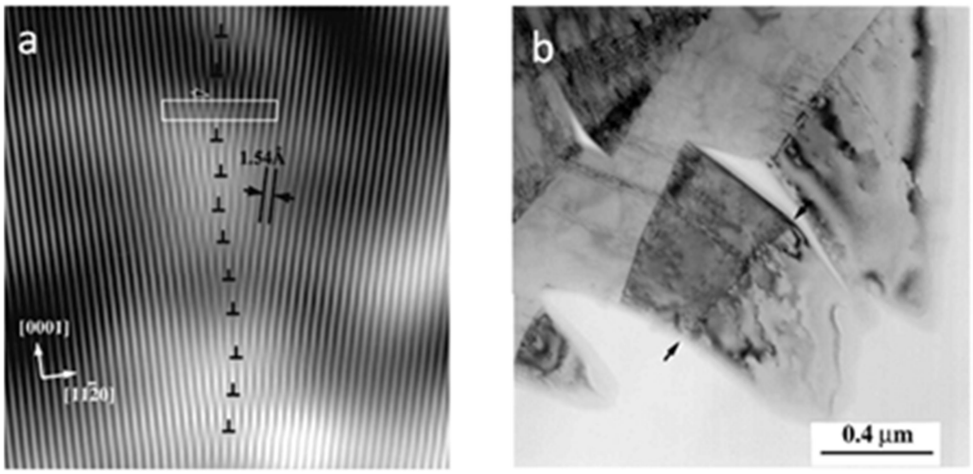

Figure 1-2: Transmission electron microscopy (TEM) showing basal plane dislocations arranged in a wall (a); and area containing kink band in Ti_3SiC_2 deformed at room temperature; reprinted from [19].

First described by Orowan [15] and later by Frank and Stroh [16], kinks form in the area of maximum shear stress in the elastically buckled grains, and consist of regularly spaced basal plane dislocations arranged in two dislocation walls (DW) of the opposite sign [16]. Both kinking and dislocation glide in (and only in) basal planes lead to the highly anisotropic plastic behavior of MAX phases where the orientation of the individual grain relative to the applied load dictates their mechanical behavior [4, 20, 21]. Therefore, it has been postulated that grains whose basal planes are oriented at approximately 45^{o} to the loading direction in compression having high Schmid factor, hereinafter referred to as soft grains (green grains in Figure 1-3), can easily deform by glide of basal plane dislocations once the local stress in the grain reaches the critical resolved shear stress (CRSS). However, grains whose basal planes are parallel to the loading direction, hereinafter referred to as longitudinal hard grains (blue grains in Figure 1-3), can deformed by kinking once the local stress reaches the critical value [16], while the grains whose basal planes are perpendicular to the loading direction, hereinafter referred to as transversal hard grains (red grains in Figure 1-3), can hardly deform in any other way but elastically.

1.1 Properties and Applications of Ti_2AlC Phases

Select room temperature elastic and mechanical properties of Ti_2AlC, along with Ti_3AlC_2 and Ti_3SiC_2, the three most studied MAX phases, are presented in Table 1-1.

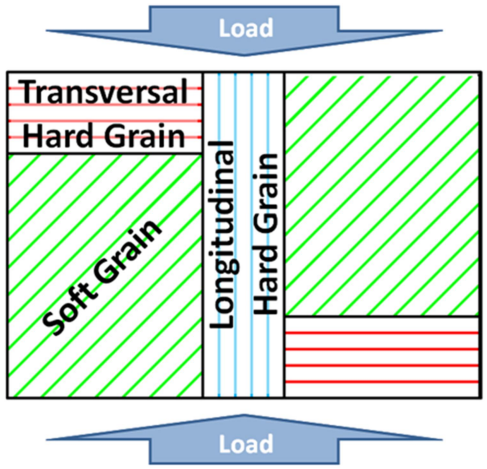

Figure 1-3: Schematic representation of individual grain orientations relative to applied load in three idealized orientations as determined by their basal planes.

Table 1-1: Density, Young's modulus E, shear modulus G, Poisson's ratio v, fracture toughness K1C, and compressive strength σ, at room temperature of Ti_2AlC, Ti_3AlC_2, and Ti_3SiC_2 as compiled in [4].

	Ti_2AlC	*Ti_3AlC2*	*Ti_3SiC_2*
Density (g cm^{-3})	4.1	4.2	4.52
E (GPa)	277	297	339-343
G (GPA)	118	124	139
v	0.19	0.2	0.2
K_{1C} (MPa $m^{1/2}$)	6.5	6.9 – 9.5	8 - 16
σ (MPa)	540	764	1050

Of the three, Ti_2AlC has the lowest density and is the preferred for high temperature applications because of its oxidation resistance [2, 4-8]. In addition, it is machinable [1, 5], and has better damage tolerance than binary carbides with the additional benefit of being thermal shock resistant [22]. The natural application for these materials is in the high temperature regime. Currently some applications under development include heating elements, gas burner nozzles, and industrial die inserts by Kanthal [2]. Other applications that have been proposed by 3-ONE-2, LLC include glove molds, diamond/Ti3SiC2 composite for concrete drilling, and non-stick coatings in cooking ware, among others [2]. They have also potential to be used as electrical contacts [23], and most recently their potential for in-core nuclear applications, including structural and fuel coatings for Gen IV nuclear reactors, is being investigated [24, 25].

1.2 Problem Statement

The nanolaminated structure and its inherent plastic anisotropy give MAX phases a very unique set of mechanical properties. When cyclic loaded, even at room temperature, they exhibit reversible hysteretic behavior [26-37]. However, when loaded at high temperatures they undergo a Brittle-to-Plastic Transition Temperature (BPTT) [17, 26, 30, 38-49]. Although these last two characteristics of their mechanical behavior have been widely reported, the fundamental underlying mechanisms are still the subject of debate. The goal of this work is to explore these mechanisms through investigating the effect of microstructure on the mechanical properties of Ti_2AlC. It is expected that results obtained on bulk polycrystalline Ti_2AlC samples in this work, can be extended to

the over 60 MAX phase compounds that have been discovered to date. It is important to reiterate that Ti_2AlC was chosen for this study since it is one of the most promising MAX phase for high temperature applications due to its high oxidation resistance provided by a self-forming Al_2O_3 protective coating that is resistant to spallation during thermal cycling, and in addition has crack healing capability in Ti_2AlC [2, 4-9, 11, 12, 50-60].

1.3 Research Objectives

The overall goal of this study is to expand the fundamental understanding on the effect of microstructure on the mechanical properties of MAX phases, in general, and Ti_2AlC in particular, at room and high temperatures under quasi-static loading conditions. Specifically the main objectives of this study are:

1. To identify the underlying mechanism(s) and the effects of microstructure on the hysteretic behavior of Ti_2AlC by taking a new approach through the combination of compression testing, RUS, and EBSD analysis.
2. To reconcile the scatter in reported UCS values by performing a systematic study on the effect of grain size and impurity on the UCS of Ti_2AlC at room temperature.
3. To understand the effect of grain size and impurities on the high temperature mechanical properties of Ti_2AlC and uncover the underlying mechanism behind the BPTT in MAX phases.

1.4 Dissertation Organization

This dissertation consists of 5 sections. Section 2 reports and discusses on the on the hysteretic behavior of Ti_2AlC at room temperature and the discovery of four regions of stress both fine (FG) and course (CG) grain Ti_2AlC with substantially different underlining deformation mechanisms. In Section 3, the effect of microstructure on the room temperature compressive strength and hysteretic behavior is discussed. The high temperature compressive response of Ti_2AlC is investigated in Section 4. Finally, Section 5 provides a summary and offers suggestions on future work.

2 ROOM TEMPERATURE STRESS-STRAIN HYSTERESIS IN Ti_2AlC REVISITED

2.1 Synopsis

Room temperature cyclic compressive testing of high purity fine (FG) and coarse (CG) grain Ti_2AlC were carried out in combination resonant ultrasound spectroscopy (RUS) tests and post mortem electron backscatter diffraction (EBSD). Results of this study show that room temperature mechanical response of Ti_2AlC is complex can be divided in four stress regions with distinct underlying mechanisms: (a) Region I (FG: 0 to 175 MPa; CG: 0 to 100 MPa) is characterized by a linear elastic behavior; (b) Region II (FG: from 175 to 350 MPa; CG from 100 to 200 MPa) displays a stress strain hysteric behavior due to reversible dislocation flow in the soft grains; (c) Region III (FG: from 350 to 1100 MPa; CG from 200 to 650 MPa) where accumulation of Dislocation Walls (DWs) result in cyclic hardening and contribute to lager hysteretic loops and thus larger energy dissipation per each loading cycle than that observed in Region II; (d) Region IV (FG: from 1100 MPa to failure, CG from 600 MPa to failure) is characterized by the occurrence of microcracking, in addition to the other deformation mechanisms mentioned above, contributing to the energy dissipated in each loading cycle.

2.2 Introduction

One of the most intriguing properties of MAX phases is their hysteretic stress-strain behavior that was reported for the first time in Ti_3SiC_2 during cyclic tension and compression loading, and later on for other MAX phases such as Ti_2AlC, Ti_3AlC_2, and Ti_3GeC_2 among others [26-30]. When MAX phases are subjected to cyclic loading-unloading at room temperature, their stress-strain response is non-linear elastic (see Figure 2-1), and in some MAX phases such as Ti_2AlC, all but the first stress-strain hysteresis loops are closed, reversible and reproducible [28]. The amount of mechanical energy dissipated during each loading-unloading cycle is quite impressive for stiff solids like MAX phases, i.e. about 25% and 24% for Ti_3SiC_2 and Ti_2AlC[1] per each loading cycle [27, 61].

The first attempt to explain the hysteretic behavior in MAX phases, was a microscale dislocation model for kinking nonlinear elastic (KNE) deformation proposed by Barsoum et al. usually referred to as KNE model[62-65]. The KNE model builds on the theory of Frank and Stroh's, who laid the theoretical foundation for kinking, and according to KNE model damping in MAX phases occurs due to reversible formation, growth and annihilation of incipient kink bands (IKBs) under the stress. IKBs consist of multiple coaxial dislocation loops stacked in parallel basal planes on the top of each other (see Figure 4a in [4]). IKB are proposed to be precursors to fully developed kink bands (KBs), as their growth and dissociation result in the formation of two dislocation

[1] Those values were estimated from [27, 61] for $T_{i3}SiC_2$ and Ti_2AlC, respectively.

walls of opposite signs, usually referred to as mobile dislocation walls (MDWs). According to the KNE model, IKBs should form in the longitudinal hard grains (or kinking grains) under loading once the applied stress reaches a threshold value. When the stress is removed, dislocation loops forming IKB shrink back and annihilate, resulting in permanent recovery of deformation strain and energy dissipation[32], Figure 2-2b.

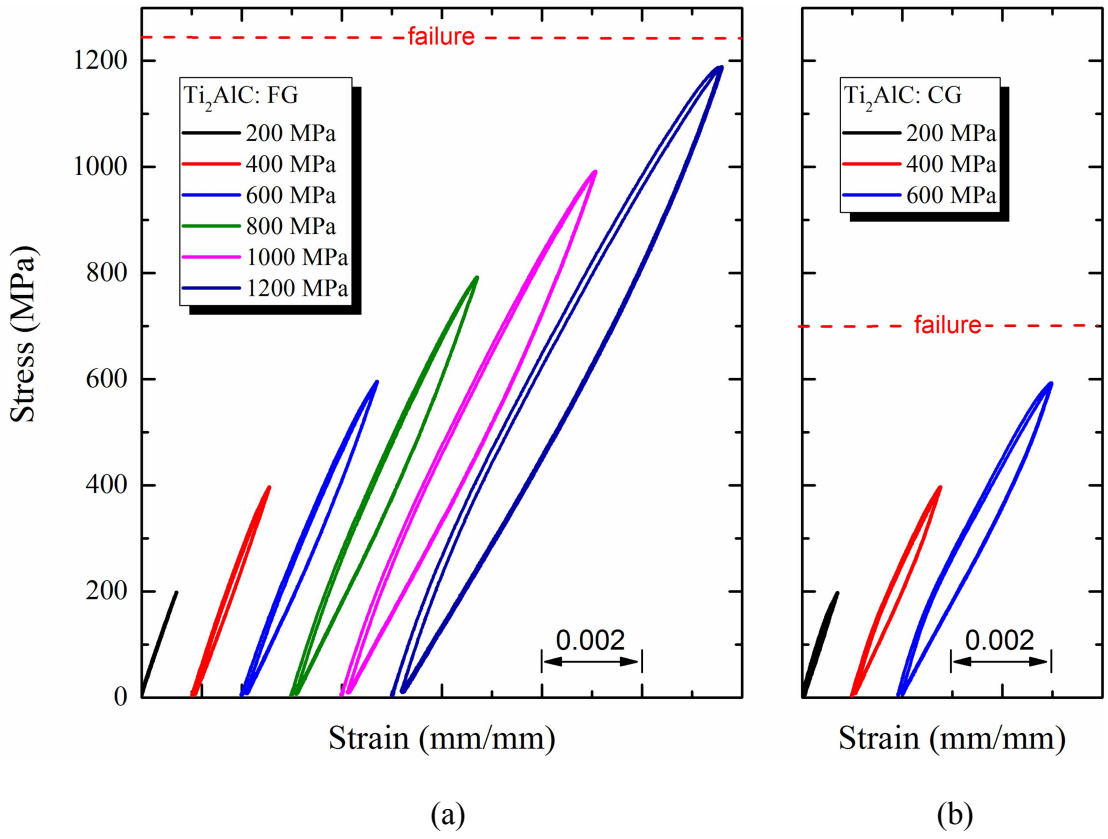

Figure 2-1: Stress-strain behavior of Ti_2AlC MAX phase in compression at loading frequency of 0.5 Hz; (a) Fine grain (FG) structure and (b) Coarse grain (CG) structure.

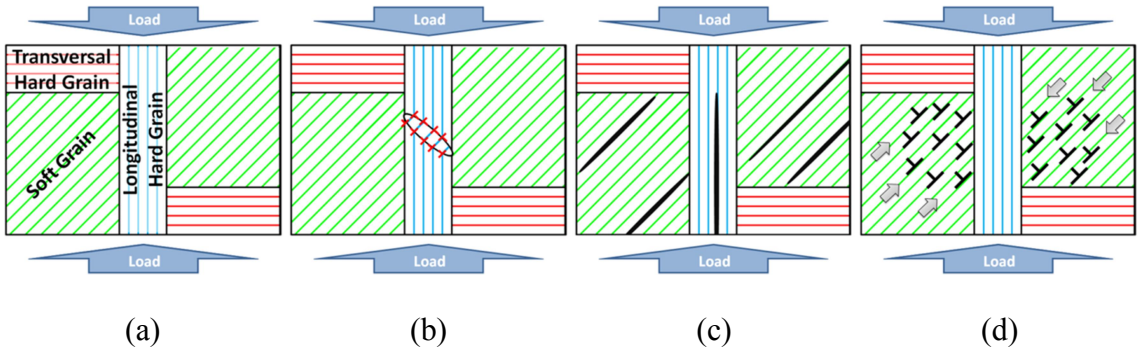

Figure 2-2: Schematic representation of different mechanisms proposed to explain hysteretic stress-strain behavior of MAX phases. Green, red and blue lines denote orientation of basal plans in each grain. (a) Schematic of hypothetical microstructure consisting of soft (green), hard (red) and kinking (blue) grains; (b) Formation of IKB under the stress in kinking grain according to KNE model [27, 62, 64, 66]; (c) Stress induced delamination according to microcracking model [36]; (d) Dislocation glide in soft grains according to reversible flow model [37].

The KNE model predicts that the dissipated energy per unit volume per cycle (W_d) and the non-liner elastic strain (ε_{NL}) should be linear function of σ^2, where σ is the maximum applied stress per cycle, while W_d should be a linear function of ε_{NL}. These relationships are in good agreement with experimental observations. Moreover, the underlying micromechanism of the KNE model offers an effective explanation to other findings such that W_d increases with grain size and porosity [31, 61, 66]. The KNE model, however does not account for the contribution of eventual reversible deformation in any but kinking grains, which raises an issue with the strain compatibility in polycrystalline structures. In other words, deformation of the grains in which IKBs form due to their favorable orientation relative to applied stress has to be accommodated by elastic or plastic deformation of surrounding grains not favorably oriented for kinking, or otherwise large incompatibility stresses in neighboring grains and eventual intergranular cracking (Zener-Stroh type cracks [67-69]) would appear, resulting in hysteresis loop

that are not fully closed and reproducible after large number of loading cycles. In addition, this model does not address the fact that the first loading-unloading hysteresis loop might be open. Furthermore, one of the challenges of the KNE model is that although permanent KB have been observed in MAX phases, there are no documented observations of IKBs [34].

Recently, an alternate model with a radically different underlying mechanism was proposed to explain the nonlinear hysteretic behavior of MAX phases, further referred to as microcracking model (MC) [36]. This model is based on the work of Walsh [70] and Lawn and Marshall [71] and proposes that damage (i.e. microcracks and delamination) accumulation and the resulting friction between the delamination crack faces (Figure 2-2c) cause the observed hysteretic behavior in MAX phases. Nevertheless, contrary to many previous observations Poon et al. reported that Ti_2AlC initially behaved as linear elastic solid showing hysteretic loops only beyond a "yield point" of 540 MPa [36]. The crack density calculated using this model was found to be in agreement with crack densities measured using scanning electron microscopy (SEM) images taken after loading to various strain levels. This model captures the nonlinearity of the stress-strain behavior for loading above 540 MPa, and can potentially explain opening of the first loop due to microcracking. However, upon careful examination of the micrographs presented in that study, significant amount of intergranular secondary phase (most likely $TiAl_x$) grains can be observed and neither their existence nor their potential effect on mechanical response are addressed in this study. In addition, it is very

unlikely that microcracking would result in stable and reproducible hysteretic loops in up to 100 cycles that have been reported for MAX phases elsewhere [27].

A most recent study by Jones et al. [37], further referred to as reversible flow (RF) model, also disregards IKBs formation and annihilation as the main hysteretic mechanism in the MAX phases based on the interpretation of results obtained by: (i) in-situ synchrotron X-ray diffraction during cyclic compression testing; and (ii) elasto-plastic self-consistent (EPSC) modeling [72-74] that is derived from Eshelby's homogeneous inclusion method [75, 76]. According to this model, macroscopically observed hysteretic behavior of MAX phases is attributed to plastic anisotropy or Bauschinger-like effect. More specifically, this model proposes that the residual elastic lattice strains that buildup in hard grains upon initial loading-unloading cycle as a result of anisotropic deformation and easy yielding and flow of only soft grains, are sufficient to drive reverse flow of soft grains, giving rise to some permanent plastic strain in the first loading-unloading cycle and reversible hysteretic behavior in any subsequent loading cycle (Figure 2-2d). Although not explicitly stated in the original work by Jones et al. [37], the flow in soft grains is assumed to occur predominantly by reversible dislocation glide in basal planes to and from dislocation pile-ups on the grain boundaries. Furthermore, the authors of the RF model argue against the concept of IKB formation due to the fact that their formation would not lead by itself to residual (plastic) strains and observed opening of the hysteresis loop during the first load-unload cycle. Although their numerical predictions using the EPSC model capture some of the qualitative details of the experimental responses, they do not quantitatively predict or

explain all of the features observed in the mechanical tests. For example, predicted residual (plastic) strains after the first loading-unloading cycle up to 400 MPa are larger than measured ones (compare Figures 2 and 5 in [37]). In addition, contrary to many experimental observations [28, 33, 34, 61, 62, 77], the RF model predicts that W_d should be a linear function of σ. Last but not least, although the RF model takes into account incompatibility stresses that develop due to plastic anisotropy, this model also attributes energy dissipation during cyclic loading exclusively to one mechanism, namely reversible dislocation flow in soft grains. The latter is in disagreement with some previous studies showing that the energy dissipated only by reversible glide of dislocations is insufficient to account for W_d obtained in experimental work [78].

Building on the RF model, Guitton at al. [21] used in-situ neutron diffraction to study the response of another MAX phase, namely Ti_2AlN, showing hysteretic behavior under cyclic compressive loading. Their results demonstrate strong variation of heterogeneous strains in all grains with different orientations as a result of anisotropic elastic and plastic deformation during loading that is even more pronounced above a threshold stress of around 200 MPa above which mechanical response becomes hysteretic. Moreover, deformation in grains with basal plans parallel to the applied load (longitudinal hard grains) was found to be most likely elastic at all applied stresses, as it is proposed by the RF model. However, contrary to the RF model, results of this work indicate that when applied stress exceeds critical value of around 200 MPa, reversible "plastic" deformation occurs not only in soft grains, but also in transversal hard grains, i.e. in all grains in which the angle between the [0001] direction and the direction of

applied stress is below approximately 70°. The latter is attributed to the plastic bending of transversal hard grains caused by complex multi-axial stress state and complex interconnections of the grains in polycrystalline structure.

The objective of the work described in this section is to further investigate to what extent the observed hysteretic behavior of Ti_2AlC can be attributed to the development of the complex stress state (i.e. incompatibility stresses), microcracking, dislocation glide, and/or incipient kinking. In this study, high purity Ti_2AlC with fine and coarse microstructures were exposed to cyclic compressive loading and complemented with subsequent resonant ultrasound spectroscopy (RUS) tests and electron backscatter diffraction (EBSD) analysis in an attempt to shed more light on the room temperature hysteretic stress-strain behavior of MAX phases. By performing small incremental steps in the applied cyclic stress and monitoring the changes in the residual (plastic) strain, area of hysteresis loops, elastic properties, and microstructure, four regions with distinct underlying mechanisms were identified.

2.3 Experimental Procedure

High purity Ti_2AlC samples were prepared via a two-step processing in which Ti_2AlC powders were synthesized and subsequently densified by spark plasma sintering (SPS)[2]. For the Ti_2AlC powder synthesis, elemental powders of Ti (99.5%, -325 mesh) Al (99.5%, -325 mesh) and TiC (99.5%, 2 μm), all from Alpha Aesar, USA, were mixed

[2] Less common but more appropriately referred to as Electric Current Assisted Sintering (ECAS)

with molar ratio of Ti:Al:TiC = 1.00:1.05:0.95 optimized to achieve high purity powders, by ball milling for 24 hrs. The mixture was placed in alumina boats and pressureless sintered in a tube furnace (GSL1600X, MTI Corporation, USA) at 1400°C under UHP argon. The sintered compact of reacted powder was then drill milled and subsequently sieved to produce -170 mesh Ti_2AlC powders which were then densified by SPS for 45 minutes at 1300°C under UHP argon. In order to study the effect of grain size, a coarse grain sample was prepared following the previous steps but with an additional heat treatment of 24 hours at 1300°C in the tube furnace operated under argon atmosphere to promote grain growth.

The density of the sintered samples was measured by the alcohol immersion method (200 proof ethanol) based on Archimedes' principle, using the procedure that is described in more detail elsewhere [79, 80]. The microstructure and phase composition of the sintered samples was characterized by field emission SEM (Quanta 600 FEG, FEI, USA) equipped with BSE detector and Energy Dispersive Spectroscopy (EDS) system (Oxford Instruments, UK), using both polished and polished and etched surfaces. The sample's grain size and the volume percent of intermetallic impurity on the samples were determined from SEM images using Image J software. X-ray diffraction (XRD) spectra were collected using a diffractometer (D8 Discover, Bruker, USA) with Cu K_α radiation at 40 kV and 40 mA, to complement phase identification and quantification. The spectra were acquired in 8^o– 80^o 2θ range with 0.024^o step and a rate of 3.5 ^{o}/min.

In addition, EBSD analysis was used to characterize the microstructure of the as-sintered and selected samples after exposure to compressive cyclic loading (see below).

These samples were mounted into 25 mm diameter epoxy blocks and mechanically polished using SiC grinding papers and diamond suspensions with the final polishing using 60 nm OP-S colloidal silica for 15 minutes in order to provide a very smooth and flat surface. The epoxy blocks holding the samples were then coated with silver paint in order to provide the necessary electron grounding during the EBSD process. These samples were placed in a pre-tilted 70^{o} specimen holder to provide the high tilt angle required for EBSD. The EBSD scans were carried out using a Zeiss Ultra field emission gun SEM equipped with Oxford Instruments AZtec integrated EDS and EBSD system, with X-Max 20 mm^2 silicon drift EDS detector and Nordlys-nano EBSD detector. The scans were done with a step size of 0.2 μm within a scanned area of 250 μm x 250 μm for all the samples. All the scans were done with an accelerating voltage of 20 KeV at either 4x4 or 8x8 binning. Data acquisition and analysis were done using Oxford Instrument's AZTecHKL and HKL Tango software.

Uniaxial cyclic compression tests were performed on cylindrical samples with dimensions of 9 mm in diameter and 17 mm in length, cut by wire electron discharge machining (Wire-EDM) and loaded in a servo-hydraulic testing machine (MTS-810, MTS, USA) at a frequency of 0.5 Hz. At each testing step, the sample was cyclically loaded and unloaded twice to the same magnitude of the maximum stress while an axial extensometer (632.13E-23, MTS, USA), was attached directly on the sample. After each testing step, the sample was taken from the loading rig for RUS (Quasar RUSpec, Magnaflux, USA) and placed back to the rig for the next testing step. In each subsequent testing step, the magnitude of the maximum stress was incremented by a small steps of

50 MPa. Those steps were repeated until sample failure occurred. The sample's elastic constants were measured with a RUS using the procedure described elsewhere [30]. RUS was chosen for its superb ability to detect defects in stiff solids independent of their location in the sample and its superior precision and repeatability in the determination of elastic constants [81, 82]. Note that due to the polycrystalline nature of the samples and since the sample size was much larger than the grain size, elastic isotropy was assumed in the calculation of elastic moduli. RUS spectra were collected prior to mechanical testing and after each increase in stress amplitude.

2.4 Results and Discussion

2.4.1 Microstructural Characterization of As-Processed Samples

Backscatter SEM micrographs of polished FG and CG sample in Figure 2-3a and Figure 2-3b illustrate uniform composition of Ti_2AlC samples with some porosity and small amount of two other phases, identified by EDS to be closest to Al_2O_3 (black in Figure 2-3a and Figure 2-3b) and $TiAl_x$ (medium gray phase in Figure 2-3a and Figure 2-3b). The latter makes up about 3 vol % as determined by image analysis of BSE SEM images. XRD results (not shown here) also confirmed the high purity of the processed samples, i.e. no XRD peaks belonging to other phases but Ti_2AlC were observed. Moreover, EBSD analysis of as-processed samples in different locations showed that all samples contained less than 3.3 % of Al_2O_3, 1.4% TiAl, and 0.16% TiC impurities. Note that the porosity observed in the micrographs is in good agreement with the measured

relative density of 98%. From the etched micrographs (Figure 2-3c) the average grain diameter and thickness for the fine grain (FG) were determined to be 6 μm ± 3 μm and 5 μm ± 2 μm, respectively, by measuring sizes of more than 100 grains. For the coarse grain (CG) structure (Figure 2-3d), the average grain diameter of 17 μm ± 10 μm and thickness of 8 μm ± 3 μm was determined using the same procedure. The fine grain size microstructure with the low aspect ratio was chosen for this study to limit kinking to high stresses.

2.4.2 Cyclic Compression Testing

Selected but typical stress-strain responses for both FG and CG Ti_2AlC, shown in Figure 2-1**,** resemble that of MAX phases reported elsewhere whereby the first load-unload cycle, or first loop, exhibits some irrecoverable deformation or plastic strain, while the second load-unload loop is closed at lower stresses, or nearly closed at higher stresses [28]. Two quantities were extracted from the stress-strain curves at each maximum applied stress: (i) W_d from second load-unload cycle; and (ii) the first loop irrecoverable plastic strain ($\Delta\varepsilon_{PL}$) otherwise commonly referred to as the opening of the first loop. Note that $\Delta\varepsilon_{PL}$ determined in each subsequent testing step corresponds only to

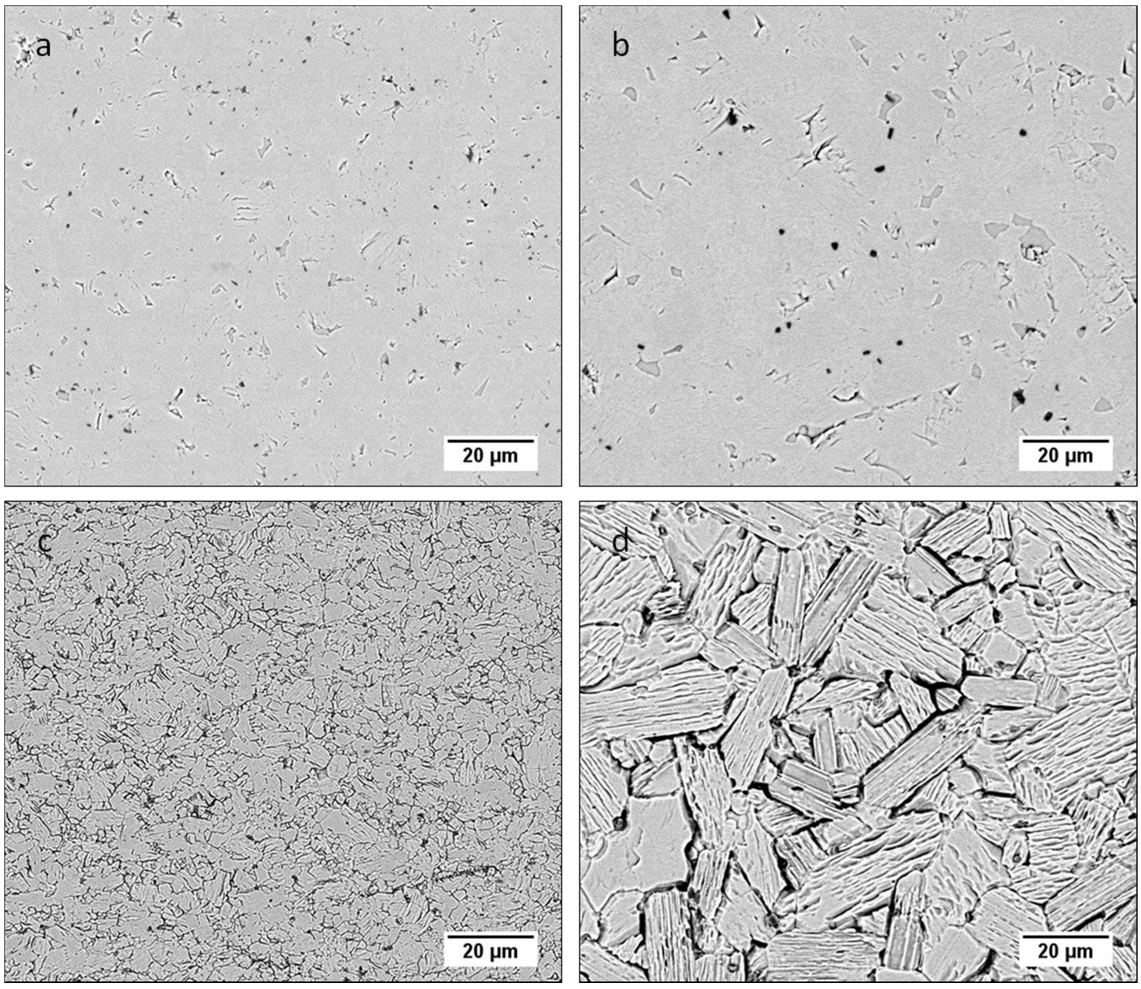

Figure 2-3: Backscatter SEM micrographs of: (a) polished FG Ti_2AlC sample sintered at 1300°C for 45 minutes, (b) polished CG Ti_2AlC sample sintered at 1300°C for 45 minutes with an additional heat treatment of 24 hours at 1300°C; both micrographs show same small porosity, small dark areas of Al_2O_3 and grey areas of $TiAl_x$ as identified by EDS; (c) and (d) are backscatter SEM images of etched FG and CG specimens, respectively, showing differences in grain sizes between the two microstructures.

the irrecoverable strain produced by loading to the stress that is 50 MPa larger than that in the previous testing step. The relative Young's modulus, i.e. modulus after cyclic loading divided by the modulus of the untested sample, was determined from the RUS

results after each testing step, to place greater emphasis on the changes of the elastic properties as these will indicate eventual damage accumulation in the sample.

The results for uniaxial compression testing in conjunction with RUS are summarized on a single plot for each microstructure, Figure 2-4a for FG and Figure 2-4b for CG. These plots show W_d, first loop irrecoverable strain due to step increase of 50 MPa denoted as $\Delta\varepsilon_{PL}$, and relative Young's modulus as a function of σ^2. Results in Figure 2-4 clearly indicate four different stress regions, further denoted as Region I – IV, with substantially different mechanical responses of Ti_2AlC. The threshold stresses between different regions are denoted by dashed lines in Figure 2-4 and summarized in Table 2-1, while underlying mechanisms in each region are discussed in more the following section.

2.4.2.1 Region I

In this stress region (FG: 0 to 175 MPa; CG: 0 to 100 MPa), Ti_2AlC exhibits a linear elastic behavior, without any detectable hysteresis. Consequently, no energy dissipation is detected. One FG sample exhibited its first hysteresis at 150 MPa and the second one at 200 MPa and thus the average value of 175 MPa was chosen as the upper bound of Region I. Similarly, the CG sample first exhibited hysteresis at an average stress of 100 MPa. Note that the irrecoverable strain and relative Young's Modulus do not change in this stress range, Figure 2-4. Therefore, it can conclude that the macroscopic mechanical behavior of Ti_2AlC is linear elastic in Region I.

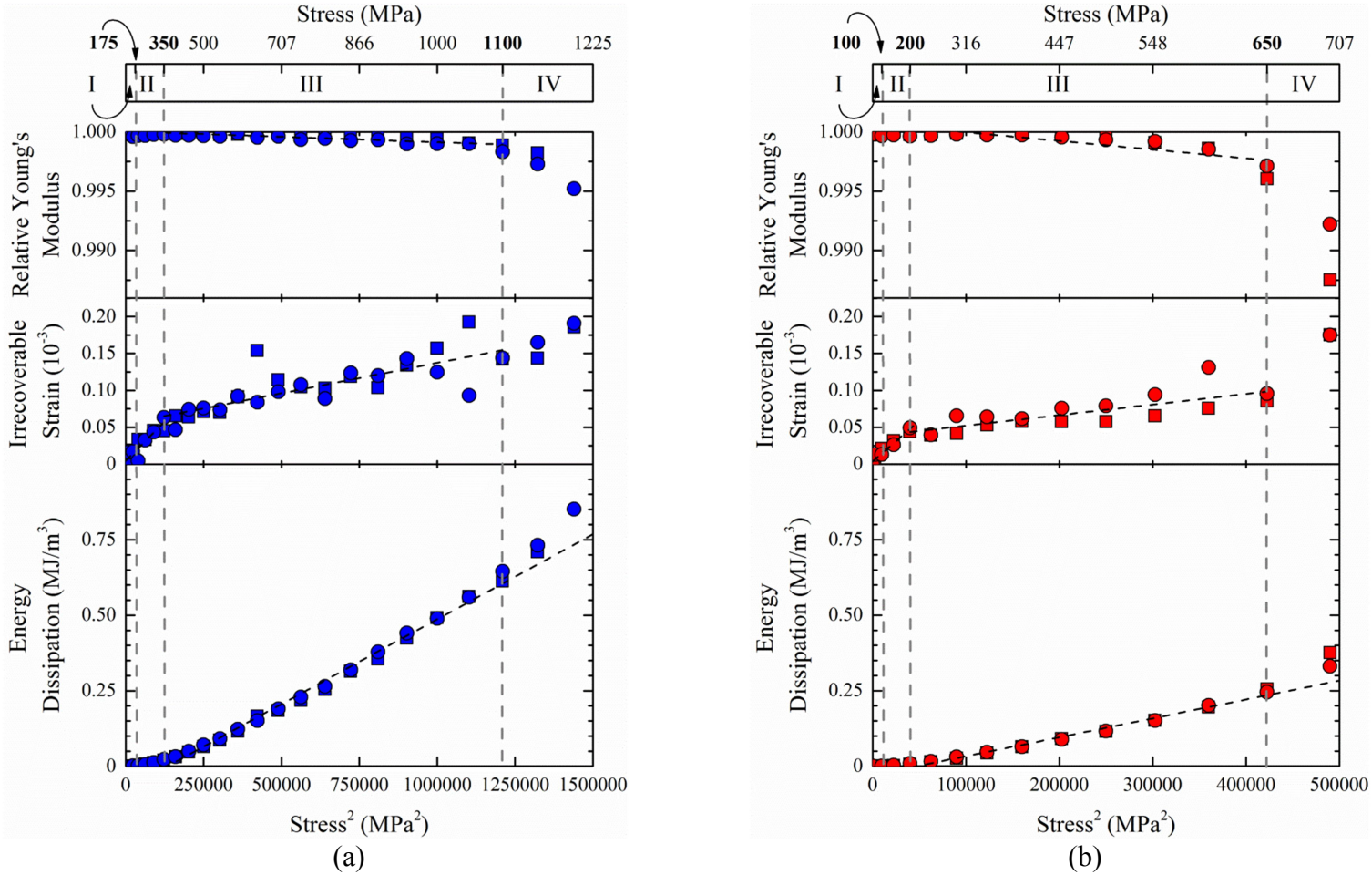

Figure 2-4: Results for mechanical testing of (a) FG and (b) CG. Bottom plots: Energy Dissipation per Unit volume per load-unload cycle (W_d) as a function of maximum applied stress squared; Middle plots: Irrecoverable strain from first load unload cycle as a function of maximum applied stress squared; Top plots: Relative Young's modulus as a function of maximum applied stress squared. Topmost scales indicate stress regions with different mechanical behavior observed in this study. Squared and circular symbols denote results obtained using two different samples for both microstructures.

Table 2-1: Threshold stresses between Regions I and II (σ_{I-II}), Regions II and III (σ_{II-III}) and Regions III and IV (σ_{III-IV}) determined from Figure 2-4 for both FG and CG microstructures. * σ_{th} is threshold stress as defined in KNE model. It is calculated from the intercept of the Wd vs σ^2 plot with σ^2-axis as described in [28].

Sample	σ_{I-II} (MPa)	σ_{II-III} (MPa)	σ_{III-IV} (MPa)	σ_{th}^{*} (MPa)
FG	175	350	1100	379
CG	100	200	650	218

2.4.2.2 Region II

This stress region (FG: from 175 to 350 MPa; CG from 100 to 200 MPa) is characterized by a gradual increase of dissipated energy per loading cycle, in conjunction with a steep increase in irrecoverable strain in the first loop with increasing maximum applied stress, and no observable change in elastic moduli, Figure 2-4. Note that the change of the first loop irrecoverable strain with stress shows more gradual progression with increasing stress (i.e. a change in slope is observed) at above 350 MPa for FG, and above 200 MPa for CG. Therefore, those stresses were defined as transition stresses between Regions II and III, σ_{II-III}. The lower transition stresses for Region II (σ_{I-II}) are much lower than threshold stresses of σ_t = 379 MPa for FG and σ_t = 218 MPa for CG, predicted using the KNE model (Table 2-1) [28]. Note that at stresses levels below the σ_t, the KNE model does not predict any hysteretic behavior and energy dissipation [62, 64, 66], which is in contradiction with results presented here. However,

the upper transition stress for Region II happens to be very close to the σ_t predicted by KNE model. Since IKBs are not expected below σ_t it is reasonable to assume that the hysteretic behavior and small amount of energy dissipation per cycle observed in this region can be attributed to the development of complex incompatibility stresses state as a result of elastic/plastic anisotropy, and reversible glide of basal plane dislocations in soft grains, as it is suggested by the RF model [37]. This conclusion can be further supported by the fact that irrecoverable strain measured during the first load-unload cycle increases rapidly with increasing maximum stresses. Note that loading within this stress region does not result in any damage since the Young's modulus does not change. The later, completely rules out microcracking as the underlying mechanism responsible for the observed opening of the first loop and hysteretic stress-strain behavior. Therefore, it is reasonable to conclude that stresses in this region are sufficient to cause small hysteresis through reversible dislocation glide due to reversible glide of basal plan dislocations in soft grains.

2.4.2.3 Region III

Mechanical response of Ti_2AlC in this region (FG: from 350 to 1100 MPa; CG from 200 to 650 MPa) is characterized by a steeper increase of W_d but a more gradual increase of $\Delta\varepsilon_{PL}$ with increasing maximum compressive stress than in Region II, Figure 2-4. Energy dissipated per cycle seems to increase linearly with σ^2 in this region, as it is indicated by the best fit line on W_d vs. σ^2 plot in Figure 2-4. This result is in good agreement with previous experimental results and predictions of KNE model [27, 62, 64,

66], and challenges the RF model that predicts a linear increase in W_d with increasing σ [37]. However, further analysis of the results summarized in Figure 2-5, actually shows that a slightly better fitting can be achieved by assuming that W_d is a function of both σ^2 and σ (i.e. assuming that $W_d = k + k' \cdot \sigma + k'' \cdot \sigma^2$), than only σ^2 (i.e. assuming that $W_d = k + k'' \cdot \sigma^2$) as suggested by the KNE model. This finding, together with the fact that $\Delta\varepsilon_{PL}$ in Region III increases much more slowly with increasing stress than in Region II, suggest that some other deformation mechanism(s), beside reversible dislocation glide in soft grains as proposed in the RF model, must be operative and is (are) responsible for the observed hysteretic stress-strain behavior. Note that whatever deformation mechanism(s) is (are) operative in Region III, it (they) must result in cyclic strain strengthening during loading because $\Delta\varepsilon_{PL}$ increases with a much slower pace with increasing stress than in Region II, but energy dissipation is much larger. To further elucidate the underlying mechanisms in this region, the evolution of the microstructure was studied using EBSD and is discussed in more detail in section 2.4.3.

It is worth nothing here that irrecoverable (plastic) strain $\Delta\varepsilon_{PL}$ or opening of the first loop --- measured after each testing step to the stress that is 50 MPa higher than the previous cycle --- is cumulative as illustrated in Figure 2-6**.** This Figure clearly shows that the accumulated opening of the first loop after two consecutive cyclic loadings to 250, 500 and 750 MPa (red line) is the identical to that obtained after cyclic loading directly to 750 MPa (black line). Note that both hysteresis loops at 750 MPa, namely one obtained in direct loading to 750 MPa and one obtained after consecutive cyclic loading,

are of the same size. However the consecutive cycling loading results in some slightly stiffer mechanical response, which again in is manifestation of cyclic hardening.

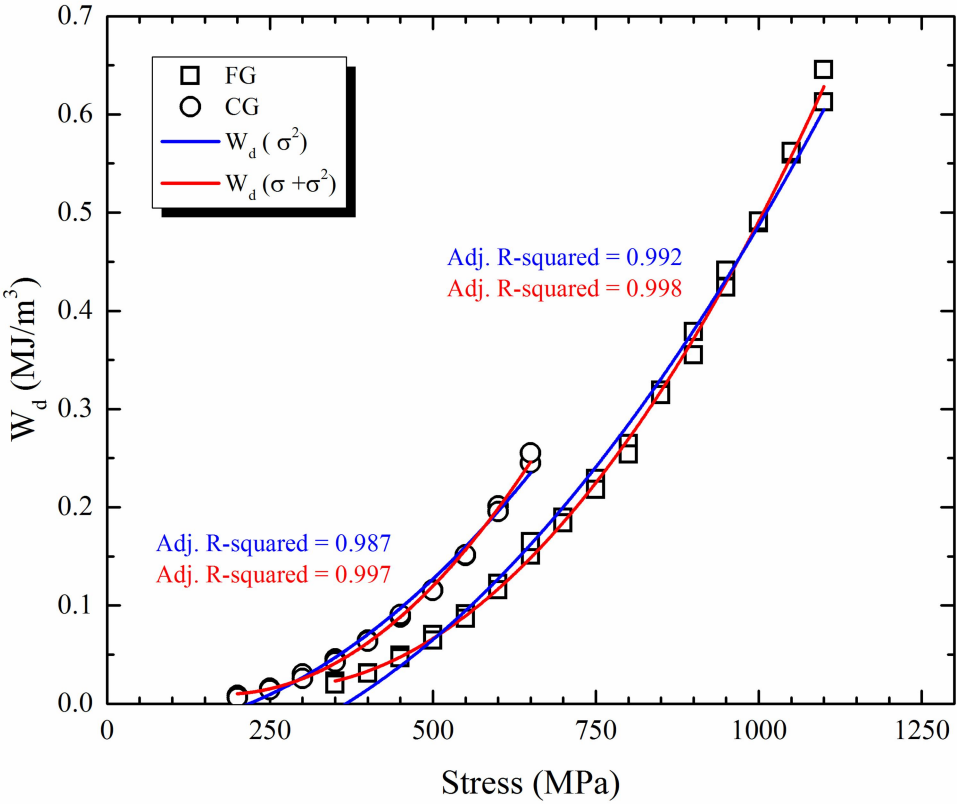

Figure 2-5: W_d per loading cycle plotted as a function of maximum loading stress in each cycle for FG (square symbols) and CG (round symbols) structure. Solid lines are the results of fitting assuming two different functions, namely $W_d=\sigma_t + k\cdot\sigma^2$ (blue) and $W_d=\sigma_t + k'\cdot\sigma + k''\cdot\sigma^2$ (red). Results are obtained using two different samples for each microstructure.

Last but not least, possible formation of microcracks in this region has to be discussed in more detail. The relative Young's modulus determined using RUS decreases monotonically with increasing stress, Figure 2-4. However, this decrease is very small, i.e. around 0.1% for FG after loading to 1100 MPa and 0.2 % for CG structure after loading to 650 MPa, and it approaches the sensitivity limits of RUS that

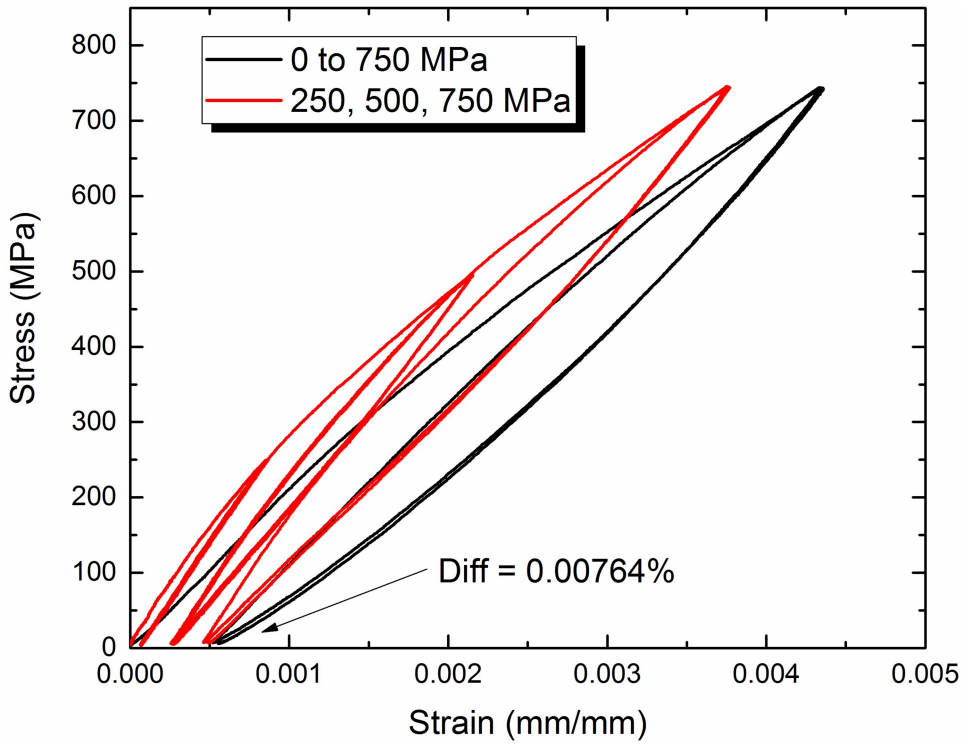

Figure 2-6: Stress strain curves obtained during cyclic loading to 750 MPa (black line), and consecutive cyclic loading to 250, 500 and 750 MPa.

has been reported to be around 0.17% [81]. In addition, results in Figure 2-7 show that that the decrease in FG structure does not exceed 0.02 % after 100 cycles up to 700 MPa. Although, these results cannot completely rule out the formation of microcracks which size and/or amount could be small to affect significantly the changes in Young's modulus, it is reasonable to conclude here that their opening and closing during cycling loading cannot be the dominant hysteretic mechanism as it is suggested in the MC model. In addition, the fact that cyclic hardening rather than softening occurs in this stress region (note that $\Delta\varepsilon_{PL}$ in this region increases much more slowly with increasing stress than in Region II) additionally supports this conclusion since formation of

microcracks during loading would result in a much steeper increase of $\Delta\varepsilon_{PL}$, i.e. cyclic softening, with increasing stress in this region when compared to Region II.

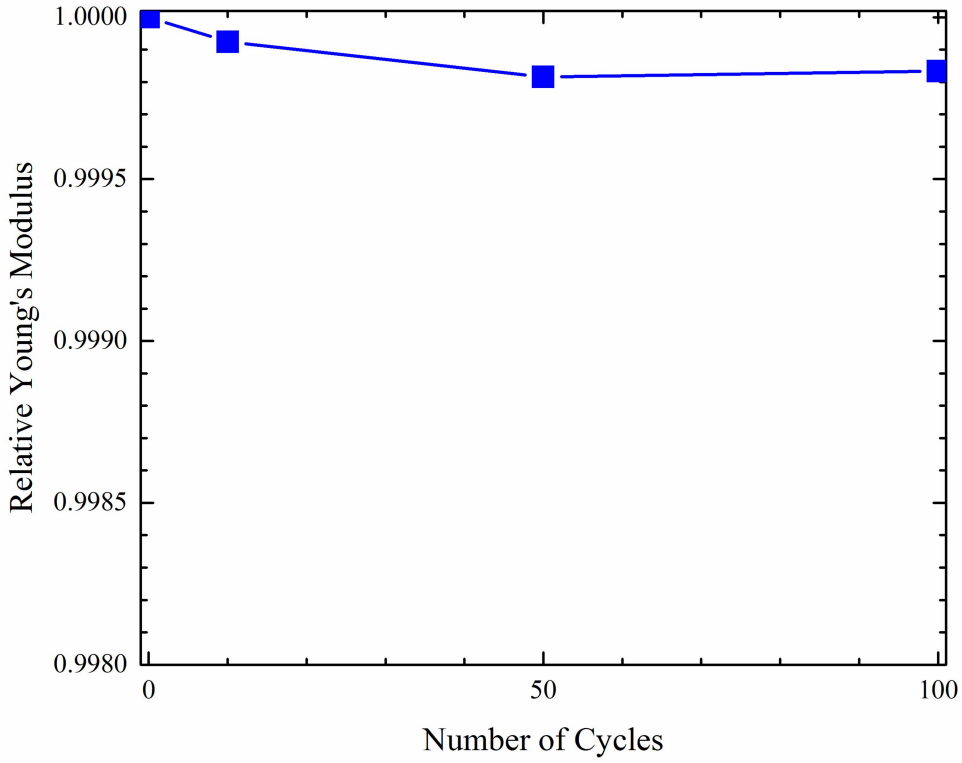

Figure 2-7: Changes of the relative Young's modulus of the FG structure as a function of number of cycles up to 700 MPA.

2.4.2.4 Region IV

This stress region (FG: from 1100 MPa to failure at ≈ 1200 MPa, CG from 600 MPa to failure at ≈ 710 MPa) is characterized by a significant increase in W_d with increasing stress, exceeding the values predicted by the KNE model that are denoted by dotted lines on the bottom plots in Figure 2-4. More importantly, a steep decrease of

elastic modulus, Figure 2-4, and even slight opening of the second hysteresis loop can be observed in this region (not shown here). These results suggest that microcracks start to form above the σ_{III-IV} transition stress producing a sudden and pronounced drop in relative elastic modulus and slight opening of the second loop. At these high stresses, the dissipation due to friction between microcracks faces also adds to the dissipation mechanism from Region III thereby increasing the overall W_d dissipated in each loading cycle as it is predicted by the MC model. It is worth noting that here that Poon et al. also reported [36] accumulation of microcracks at stresses of 540 MPa in the samples having slightly higher grain size than the CG samples in this study. This critical stress value is very close to the value of σ_{III-IV}, 650 MPa, reported here for CG structure. Last but not least, it is important to mention that the FG sample failed at 1.2 GPa which is the highest compressive strength ever reported for Ti_2AlC.

2.4.3 EBSD Results

To grasp a better understanding of underlying hysteretic mechanism in Region III, and to specifically explore the reason behind the cyclic hardening observed in that region, EBSD analysis was performed on FG and CG samples cycled twice to 500 MPa and compared to data acquired on as-sintered samples. EBSD is a valuable tool in analyzing evolution of deformation in polycrystalline MAX phases [83] because kink bands and dislocation walls result in change of crystallographic orientation (misorientation) within individual grains. Therefore, the latter two features can be easily identified by analyzing misorientations on inverse pole figure (IPF) maps obtained by

EBSD. Note that any eventual basal plane slip cannot be detected in EBSD results since it does not produced in any major misorientation within individual grains.

Figure 2-8 and Figure 2-9 summarize the EBSD results for FG and CG samples, respectively, in the as-sintered condition (top rows) and for samples cycled to 500 MPa (bottom rows). The IPF maps of as processed samples in Figure 2-8a and Figure 2-9a, show that both FG and CG samples have almost random texture with a weak alignment of the basal planes perpendicular to the loading direction applied during processing, as it is indicated by larger amount of red grains especially in FG structure. Comparison of IPF maps before and after loading (Figure 2-8a and Figure 2-8b for the FG structure and Figure 2-9a and Figure 2-9b for the CG structure) show clearly that the microstructure evolves during loading, i.e. the color in each individual grain becomes less uniform after deformation. The latter suggests development of crystallographic misorientation in individual grains during cyclic compressive loading. To further analyze misorientation development in each grain, the low angle grain boundaries (LAGBs) resulting in misorientation angles between 2^o to 10^o are plotted as red lines in Figure 2-8c, Figure 2-8d, Figure 2-9c, and Figure 2-9d, together with black lines that denote high angle grain boundaries (HAGBs) with misorientation angles across boundary exceeding 10^o. Comparison of those results reveals much larger number of LAGBs and DWs in FG and CG samples cyclically loaded to 500 MPa than in as-sintered samples.

To further analyze if some of above mentioned microstructural features form predominantly in some grains because of their preferential orientation relative to the

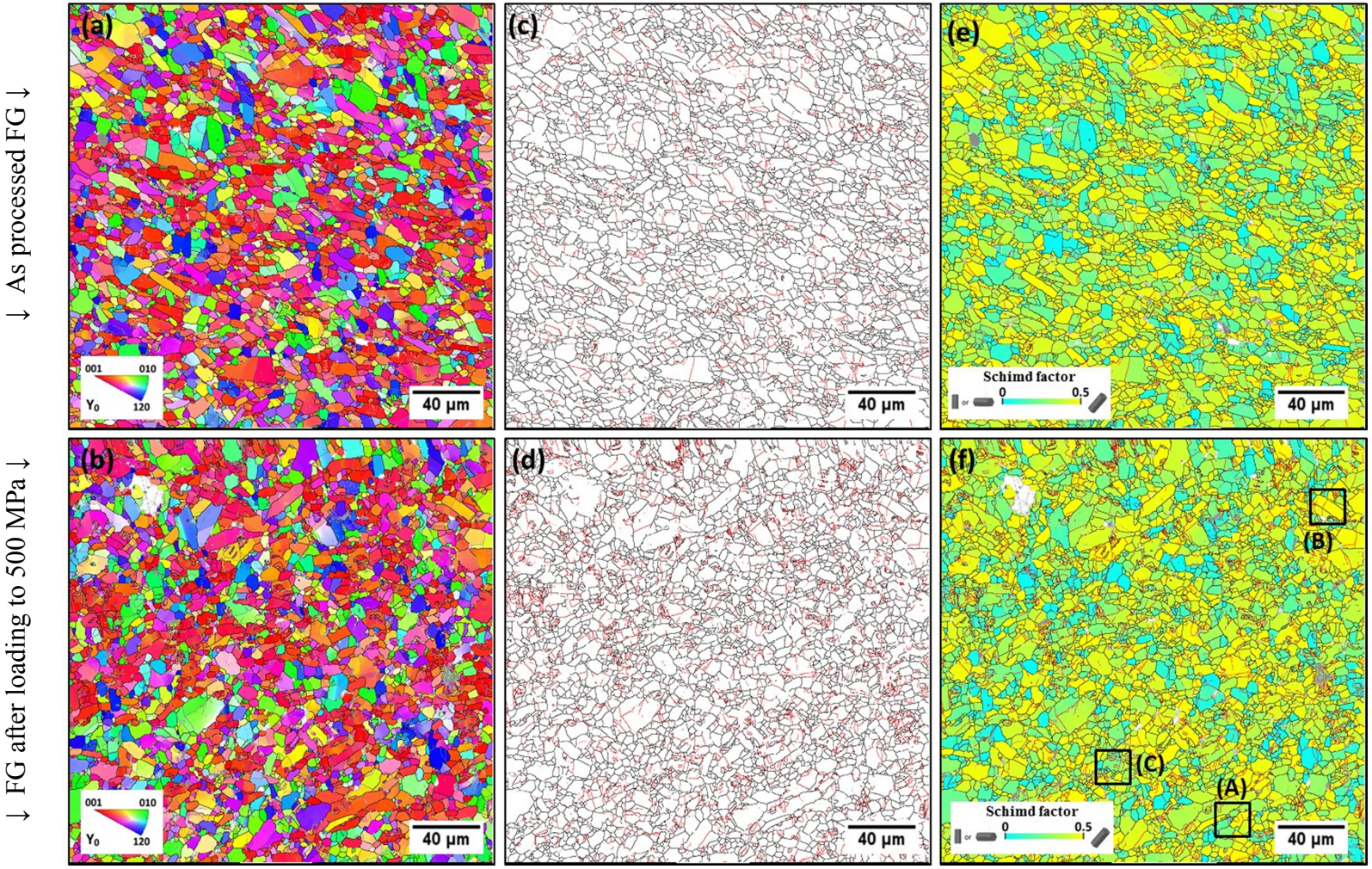

Figure 2-8: EBSD results for FG as-sintered sample (top row) and FG cycled to 500 MPa (bottom row). Both compressive loads during sintering and cyclic loading were applied in the vertical direction. (a) and (b) are inverse pole figures (IPF) maps, with the y-axis in the vertical direction; (c) and (d) Low (red lines) and high (black lines) angle grain boundaries maps; (e) and (f) Schmid factor maps with low (red lines) and high (black lines) angle grain boundaries.

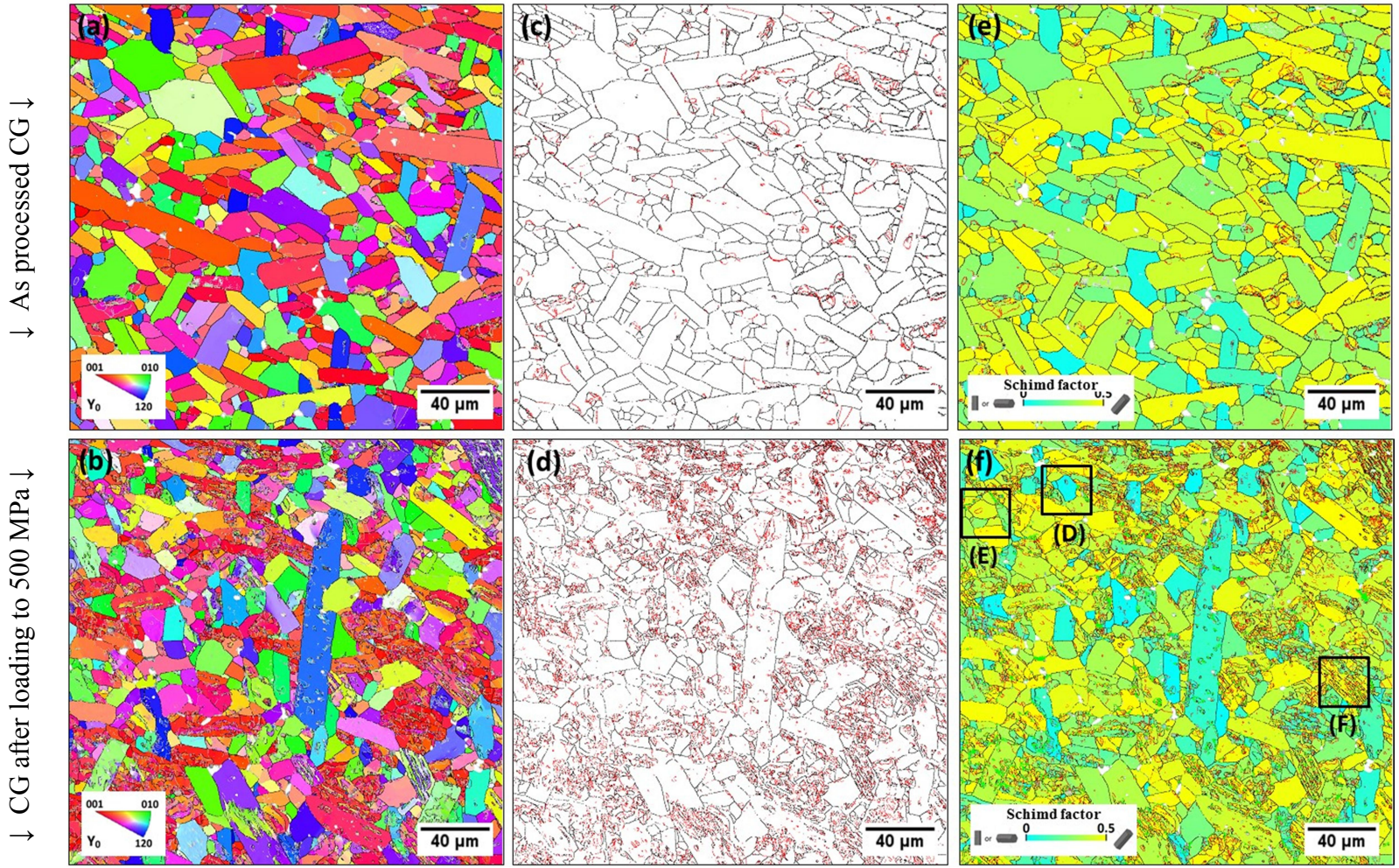

Figure 2-9: EBSD results for CG as-sintered sample (top row) and CG cycled to 500 MPa (bottom row). Both compressive loads during sintering and cyclic loading were applied in vertical direction. (a) and (b) are inverse pole figures (IPF) maps, with the y-axis in the vertical direction; (c) and (d) Low (red lines) and high (black lines) angle grain boundaries maps; (e) and (f) Schmid factor maps with low (red lines) and high (black lines) angle grain boundaries.

applied load, LAGBs and HAGBs are plotted over Schmid factor maps in Figure 2-8e, Figure 2-8f, Figure 2-9e, and Figure 2-9f. Schmid factors on those maps were determined for easy slip (0001) $[11\bar{2}0]$ and therefore light blue grains denote longitudinal and transverse hard grains having Schmid factor close to zero, while yellow grains denote soft grains with Schmid factor close to 0.5.

Careful inspection of these results show that LAGBs form in all grains independent of their Schmid factor. At the same time, some of the grains are free of any LAGBs, independent of their orientation relative to the applied load. This suggests that deformation of each individual grain is governed not only by its orientation relative to direction of applied load, but also by orientation of all neighboring grains and thus incompatibility stresses that develop due to their plastic anisotropy. The later cannot be overemphasized because it demonstrates the importance of incompatibility stresses that develop during loading in Region III on the overall mechanical response of the MAX phases. In addition, this finding challenges models used to capture the mechanical response of the MAX phases, such as EPSC, that are based on homogeneous inclusion method in which mechanical response of grains surrounding each individual grain is homogenized. Although, more work is needed to fully understand evolution of inhomogeneous evolution of LAGBs in polycrystalline MAX phases during loading at room temperature, it is worth noting that those features seem to form preferentially, but not exclusively, in grains with middle to high Schmid factors (0.25-0.5). The latter is in good agreement with recently published results of in–situ neutron diffraction studies during cycling loading of Ti_2AlN that demonstrate plastic deformation of the grains in

which the angle between the [0001] direction and the direction of applied stress is below approximately 70^{o} [21].

A closer look at the geometry of LAGBs in Figure 2-8 and Figure 2-9 also reveals that they tend to form three different configurations. Figure 2-10 shows selected but typical configurations of LAGBs in grains denoted as A, B, C, D and E in Figure 2-8e and Figure 2-9e, together with their Schmid maps and misorientation angle profile along LAGBs. Observed LAGB configurations can be categorized as:

(i) straight lines that span from grain boundary to grain boundary through the grain, Figure 2-10b and Figure 2-10c;

(ii) closed loops in the middle of grain, Figure 2-10 c**,** d and e; and

(iii) open loops (curved lines) that start at grain boundaries and curl into the grains, Figure 2-10a**.**

Assuming that LAGBs consist of dislocation walls, the distance between dislocations can be expressed as $D = \frac{b/2}{\sin(\theta/2)}$ where Burgers vector $b = \frac{1}{3}\langle 11\bar{2}0\rangle = 3.05$ Å [3]. Since the distance between Al plans in Ti_2AlC is $d_{Al\text{-}Al} = 6.8$ Å [84], it can be shown that maximum misorientation angle of 12.96^{o} can be achieved by having one dislocation in every Al basal plane. The results in Figure 2-10 show that misorientation profile across LAGBs ranges from 3^{o} to 6^{o}. This indicates that observed LAGBs consists of dislocation walls with one dislocation located in every $\approx 9^{th}$, or every $\approx 4^{th}$ Al basal plane.

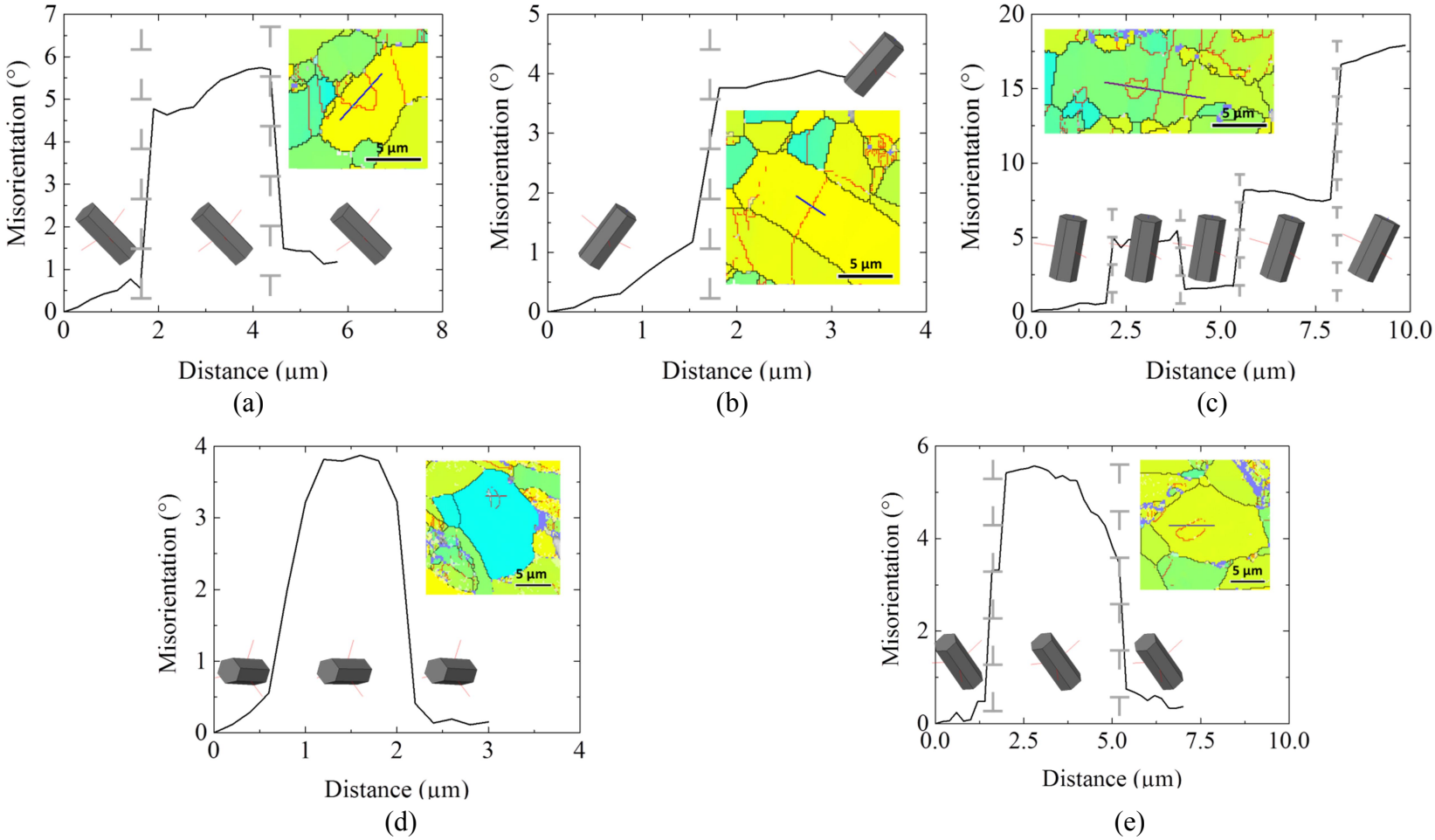

Figure 2-10: Misorientation profiles and unit cell orientation with respect to the vertically applied load for low angle grain boundaries (LAGBs) or dislocation walls (DWs), and dislocation loops in (a) grain A, (b) grain B, (c) grain C in Figure 2-8e as well as (d) grain D and (e) grain E in Figure 2-9e. Inserts show magnified Schmid factor maps for corresponding grains with low (red lines) and large (black lines) angle grain boundaries.

Straight LAGBs that span from grain boundary to grain boundary through the grain have been observed and reported in deformed MAX phases in large numbers of studies, as it was discussed elsewhere [3, 4], Those LAGBs are associated with deformation of individual grains by kinking and they confine KBs. Note that not all parallel sets of straight LAGBs confine KBs, as it is illustrated in Figure 2-10c, because those walls consist of dislocations of the same sign. Therefore, it is reasonable to conclude that straight dislocation walls do not form exclusively by growth of IKBs to fully developed KBs. It follows that another mechanism needs to be invoked to explain the presence of the walls consisting of dislocations of the same sign that that proposed by Orowan [15] and Frank and Stroh [16]. One possibility is simple bending of individual grains caused by anisotropic plastic deformation of surrounding grains.

However, the formation of closed (Figure 2-10c, d and e) and open DW loops (Figure 2-10a) in deformed MAX phases have never been reported before. The loops resemble the configuration of IKBs and partially dissociated IKBs, respectively, as predicted by KNE model [27, 28] since misorientation profile across those loops indicate that they consist of dislocation walls of opposite signs. However, in contrast to IKBs, LAGB loops observed here have relatively large diameter, exceeding in some cases 5 μm. In addition the loops form in all grains, not only in longitudinal hard grains, and they do not completely collapse upon unloading, as proposed by the KNE model. Although more work is needed to fully understand the structure of the loops and the mechanisms that leads to their formation, results indicate that highly inhomogeneous distributions of incompatibility stresses develop during loading are responsible for their

formation in all grains independent of their orientation and that they are stable. Those stresses also prevent their total collapse or annihilation during unloading as would be expected from the attractive force between two dislocation walls of opposite sign.

Herein, the difference between observed evolution of microstructure in FG and CG structure during compressive loading (Figure 2-8 and Figure 2-9) has to be discussed in more detail. When doing that, one has to consider that both microstructures were analyzed after cyclic loading to 500 MPa, which is in the middle of stress Region III for FG structure and but closer to the upper limit for stress Region III in the CG structure. Comparison of Figure 2-8d and Figure 2-9d shows that the amount of LAGBs (as straight DWs or DWs forming closed and open loops) is much higher in the CG structure than in the FG one. For example, a large number DW loops can be seen in single grains in the CG structure, as it is illustrated in longitudinal hard grain encircled with a dashed line in Figure 2-9b and f. This is not surprising because compared to the FG structure, the CG structure shows smaller resistance not only dislocation glide in basal planes (Hall–Petch effect) but also to the formation of IKBs [3, 28, 62]. While the former results in higher incompatibility stresses in the CG structure due to easier dislocation piling up in soft grains, the latter results in easier formation of IKBs. Also, as the number of IKB-like DW loop seem to be smaller in the FG structure, they appear to form mostly in grains close to soft orientation for reasons that are not entirely clear at this moment.

Results of EBSD analysis also show that the number of grains (where grain is defined as area surrounded by HAGBs) in the examined area of 250 x 250 μm^2 increases from 3,634 in the as-processed to 4,021 in the cyclically loaded FG sample, and from

896 in as-processed to 3,958 in cyclically loaded CG sample. While the slight increase in the number of grains in the FG structure could be attributed to statistical difference between two examined areas, the significant increase in the CG structure is strong evidence that grain refinement and development of substructure takes place during cyclic loading. Careful inspection of Figure 2-9f, suggests that subgrains form mostly in grains with high Schmid factor, i.e. soft grains, as it is illustrated in Figure 2-11. Although more work is needed to fully understand the mechanisms responsible for the substructure development, the misorientation profiles across the subgrains and their configuration resemble that previously observed in deformed Ti_3SiC_2 by TEM (Figure 2-11c). Note that the combination of kinking and delamination in Figure 2-11c results in misorientation of up to approximately 30^o, similar to that shown in Figure 2-11a and formation of subgrains (circled by dashed line in Figure 2-11c) similar to those observed in the examined sample (Figure 2-11b). This conclusion is further supported by the fact that highly fragmented grains contain areas with poor EBSD indexing (purple in Figure 2-11b) due to delamination and microcracking.

In conclusion for this section, EBSD results showing complex microstructural development during cyclic loading have to be put in conjecture with results of mechanical testing. Observed refinement of microstructure due to the accumulation of LAGBs forming either straight or looped DWs, and further formation of subgrains are in good agreement with observed cyclic strengthening in Region III (i.e. much more gradual increase in $\Delta\varepsilon_{PL}$ with increasing stress than in Region II) as those microstructural features are effective barriers for dislocation glide. However, since energy dissipated per

loading cycle in this stress region increases rapidly with increasing stress, reversible glide of dislocation to and from pile ups cannot be major dissipation mechanism as proposed by the RF model [37], because it would be hindered effectively by LAGBs or HAGBs that forms during the first loading cycle. Therefore, it is reasonable to conclude that the major energy dissipation mechanism in Region III is reversible movement (or bowing) of LAGBs --- not much unlike that proposed by the KNE model [28, 61, 62] --- whose number increases with increasing stress. However, in contrast to the KNE model, results presented here show that LAGBs forming DWs and loops appear in all grains independent on their orientation and that DW loops do not collapse after unloading. Both those findings can be attributed to development of complex stress states due to generations of local incompatibility stresses as a result of the high plastic anisotropy of MAX phases.

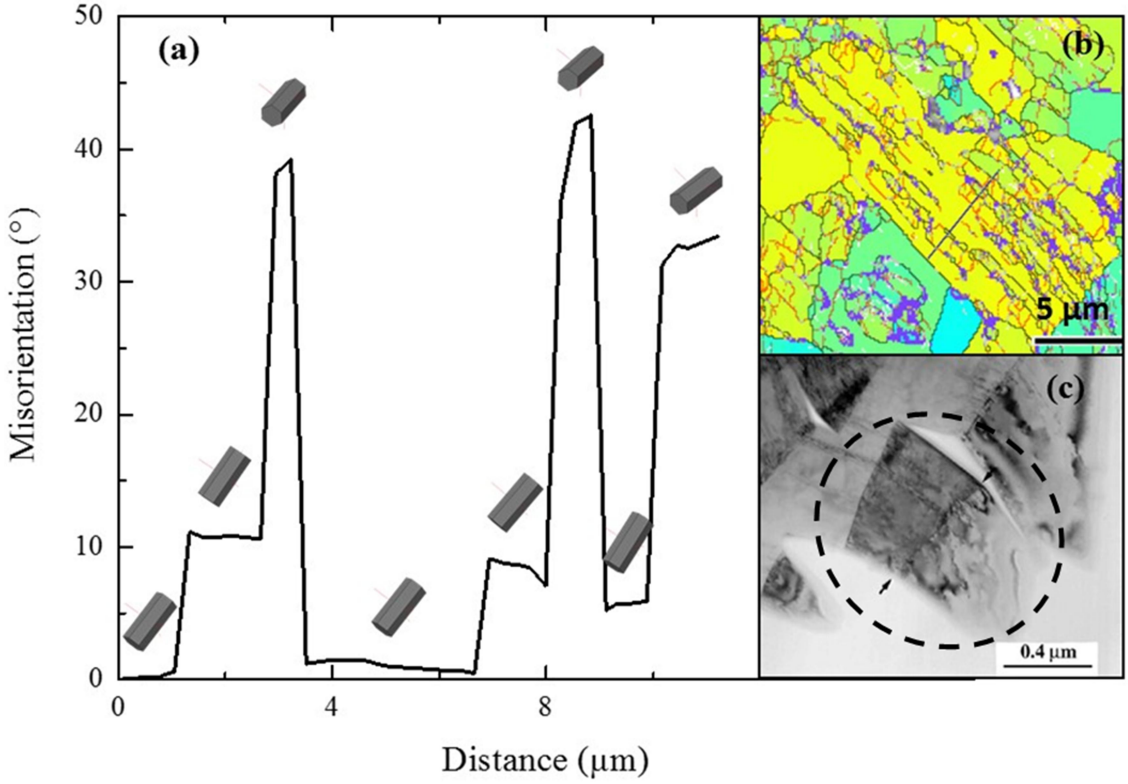

Figure 2-11 Misorientation profile and unit cell orientations with respect to the vertically applied load across grain F in Figure 8e. (b) Magnified Schmid factor map for corresponding grain with low (red lines) and large (black lines) angle grain boundaries, and unindexed areas (purple). (c) TEM of kinking and low angle grain boundaries in deformed Ti_3SiC_2 adapted from [19].

2.5 Conclusions

The results of uniaxial cyclic loading in compression, together with results of elastic modulus measurements and EBSD show that the room temperature mechanical response of both fine (FG) and course (CG) grain Ti_2AlC is quite complex and can be separated in the following four different stress regions (Region I – IV) with substantially different underlining deformation mechanisms:

- **Region I** (FG: 0 to 175 MPa; CG: 0 to 100 MPa) characterized completely linear elastic behavior;
- **Region II** (FG: from 175 to 350 MPa; CG from 100 to 200 MPa) is which hysteric behavior can be observed characterized by slightly open hysteretic loop in first loading-unloading cycle, and closed loops any subsequent loading cycle to the same stress level. In this region, small amount of energy dissipation per each cycle observed can be attributed to the development of complex incompatibility stresses as a result of elastic/plastic anisotropy, and reversible glide of basal plane dislocations in soft grains, as suggested by the reversible flow model [37].
- **Region III** (FG: from 350 to 1100 MPa; CG from 200 to 650 MPa) in which stress strain behavior is qualitative similar to that in Region II, but with a much steeper increase in energy dissipated per loading cycle and more gradual increase in the irrecoverable strain or opening of the first loop than in the previous stress region. EBSD results show complex developments of the microstructure with accumulation of a large number of dislocation walls (DWs) that span from grain boundary to grain boundary and closed or open DW loops resembling IKBs; all of which would lead cyclic hardening. The reversible movement (or bowing) of LAGBs --- not much unlike what was proposed by the KNE model [28, 61, 62]--- was proposed as a major energy dissipation mechanism in this region. It is worth noting here that EBSD results of this study provide first experimental evidence of the formation of closed dislocation loops in MAX phases.

- **Region IV** (FG: from 1100 MPa to failure, CG from 600 MPa to failure) in which stress strain behavior is qualitative similar to ones observed in Regions II and III, but shows a drop in elastic modulus due damage (microcracks) formation. Friction at the microcracks' surfaces contributes to the energy dissipated in each loading cycle, in addition to the other mechanisms mentioned above.

Results highlighted above are significant, because they show that neither proposed models namely Kinking Non-Linear Elastic, Microcracking and Reversible Flow models can be single-handedly implemented to describe the complex mechanical behavior of that the MAX phases over the entire range of stresses.

3 EFFECT OF MICROSTRUCTURE ON THE MECHANICAL PROPERTIES OF Ti_2AlC

3.1 Synopsis

This section investigates the effect microstructure, specifically the grain size and $TiAl_x$ impurity, on the compressive strength and hysteretic behavior of Ti_2AlC at room temperature. Given the plate-like nature of the MAX phase grains, lengths and thicknesses of over 100 grains for each microstructure were measured. A Hall-Petch like relationship between compressive strength and the grain length was observed, but not such a relationship was observed with the grain thickness. Results from cyclic compression testing in combination with resonant ultrasound spectroscopy show that room temperature mechanical response of Ti_2AlC can be divided into four stress regions regardless of the variation in grain size and/or impurity. The grain size relationship on the transition stresses for stress regions was also investigated. All transition stresses, between the different regions follow a Hall-Petch relationship.

3.2 Introduction

Since Ti_2AlC is one of the most attractive MAX phases for wide variety of applications, it is not surprising that numerous studies published to date reported on its mechanical properties. However, a review of those studies shows great variation of its compressive strength at room temperature. Compressive strength values span from the lowest reported of 393 MPa to the highest one of 1057 MPa, as it is are summarized in

Table 3-1 [5, 6, 17, 33, 34, 36, 48, 77, 85-88]. It is clear from Table 3-1 that the lowest and highest values of reported compressive strengths correspond to samples with largest and smallest grain sizes, respectively, indicating a possible Hall-Petch relationship. Hall-Petch type relationship between compressive strength and grain size has been proposed before for some other MAX phases, such as V_2AlC [3], $(Ti,Nb)_2AlC$ [22], and $Ti_3(Si,Ge)C_2$ [28, 89]. However, at the first glance, the rest of the compressive strengths values in Table 3-1 that range from 540 MPa to 910 MPa, do not seem to have a clear dependency on their grain size. The later suggest that some other microstructural factors might contribute to the mechanical response of $T_{i2}AlC$ under compressive loading, besides gran size.

The final microstructure of Ti_2AlC depends strongly on processing route [90]. In general, there are two types of reaction synthesis of Ti_2AlC. The first route uses the binary carbide Al_4C_3 with Ti and C powders as reactants processed in the 1300°C – 1600°C temperature range. Since aluminum carbide is a very stable compound and slow to react with Ti and C, long processing times of 4 to 48 hours are required to produce Ti_2AlC [5]. The second and more widely used approach is to use elemental powders of Al in combination with Ti, C and/or TiC as reactants primarily to reduce processing time. A significant reduction in processing time is achieve because aluminum melts at 660°C, forming a liquid that promotes fast reaction and sintering. This type of reaction is commonly referred to as solid-liquid reaction and has been shown to produce high purity Ti_2AlC after reaction sintering in as short as 1 hour [6, 84, 91-93]. Alternately, these same reactants have been used in self-propagating high-temperature synthesis

Table 3-1: Summary of compressive strengths and processing conditions for Ti_2AlC from literature.

Compressive Strength (MPa)	Microstructure: Length (μm)	Microstructure: Thickness (μm)	Microstructure: Impurities Detected	Processing Conditions: Sintering Method	Processing Conditions: Temperature (°C)	Processing Conditions: Time hrs	Reference #
393	100 – 200	-	-	Hot Press	1600	4	[17]
540 ± 21	25	-	Al_2O_3 & $TiAl_x$	Hot Isostatic Press	1300 – 1400	15 – 48	[5]
560	41 ± 12	16 ± 4	None	Hot Press	1450	1	[6]
655 ± 32	10 ± 2	5 ± 2	None	Hot Press	1350	2	[88]
670	15	-	Ti_3AlC_2	Hot Press	1400	1	[85]
865 ± 55	20 ± 10	8 ± 2	None	Hot Isostatic Press	1400	2	[33, 34, 77, 87]
910	-	-	-	-	-	-	[36]
1037	6	1	$TiAl_x$	SHS/PHIP		25 sec	[86]
1057 ± 84	3.05	-	$TiAl_x$	SHS/PHIP	-	*25 sec	[48]

(SHS) to produce high purity Ti_2AlC in the order of seconds [48, 86, 94-96]. One drawback of using pure aluminum powder as a reactant is that it evaporates during sintering, and therefore its amount in the initial powder mixture has to be adjusted to compensate for the aluminum that volatizes during synthesis [11, 59, 91], or otherwise the final product would have a large amount of secondary phases such as TiC or $TiAl_x$ [90, 97]. The evaporation rates of aluminum depend on many processing factors, including chamber pressure (vacuum or inert), gas purge rates, and heating rates among others, such that tuning the correct initial stoichiometry quickly becomes more an art than a science. In addition, since Ti_2AlC is stable only in very narrow range, see Figure 3-1, such that the final stoichiometry has to be near perfect to avoid formation of secondary phases [3]. Therefore, when analyzing the spread of compressive strengths in Table 3-1, the effect of undesired secondary phases should be accounted for, because their eventual presence can also affect mechanical behavior of Ti_2AlC. Although many sources claim high purity in their samples, their claims are based solely on X-ray diffraction (XRD) results, and not supported by any other more accurate analysis [6, 33, 77, 85]. This approach could be potentially misleading since small amounts of impurities, especially $TiAl_x$ may accumulate in triple grain junctions or as a thin film in grain boundaries, such that their size and amount may be so small as to be undetectable. In addition, since present impurities are products of incomplete reactions and/or of less than ideal stoichiometry in final product, they may form with distorted stoichiometry and/or crystal lattice which might result in peak broadening, to such an extent, that the peaks might be lost in the background signal.

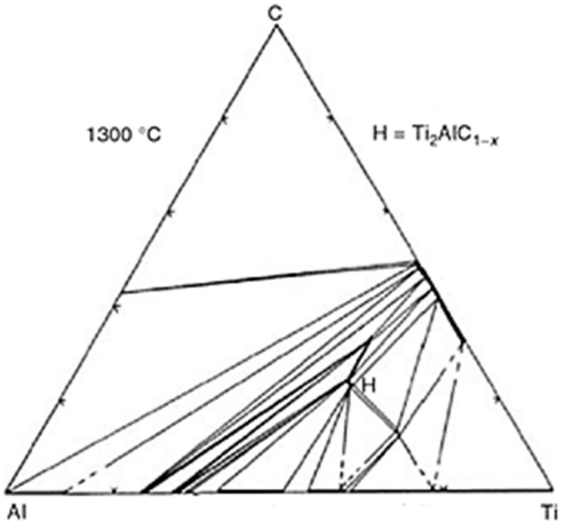

Figure 3-1: Al-Ti-C ternary phase diagram. Small area labeled H is for Ti_2AlC. Adapted from [98].

It is also well established by now that Ti_2AlC, and to further extent other MAX phases, do not behave as a typical brittle ceramic before they fail in compression. In other words, their stress-strain behavior is not linear-elastic, but rather non-linear hysteretic resulting in large hysteresis loops when samples are exposed to cyclic loading [28, 29, 33-37, 61, 62, 64-66, 77, 87, 99]. Therefore, the mechanical energy dissipation during loading-unloading cycle per unit volume (W_d) and the stress at which the first hysteresis loops can observed (σ_t) is another import quality that describes the mechanical response of MAX phases. It is well documented that W_d and σ_t in MAX phases also depend on their microstructure, i.e. it is grain size dependent with coarse grain structure dissipating more energy than fine grain structure. According to the Kinking Nonlinear Elastic (KNE) model [27-29, 61, 62]--- i.e. the first model proposed to explain the hysteretic behavior of the MAX phases --- this behavior has been attributed

to easier incipient kink bands (IKBs) formation in coarse grained structure, as it is described in more details elsewhere [27, 45, 62].

However, recently alternate models have been proposed for the reversible hysteretic behavior in MAX phases. Poon et al. [36] proposed that the hysteretic behavior of MAX phases can be attributed to the formation of delamination microcracks and the friction between crack faces during cyclic loading, which in turn, can be also scaled to the grain size. Most recently, Jones et al. [37] also challenged the relevance of IKB formation on the hysteretic behavior and instead proposed another underlying hysteretic mechanism, namely reversible flow or dislocation glide of basal plane dislocations in soft grains, i.e. grains in which critical resolved shear stress (CRSS) is first reach because of their favorable orientation relative to direction of applied load. Further referred to as the Reversible Flow (RF) model, this model is based on observations of inhomogeneous residual lattice strains that develop during loading of polycrystalline Ti_3SiC_2 in compression and the results of corresponding elasto-plastic self-consistent modeling (ESPC) [72-74]. Since this model proposes that the stress-strain hysteretic behavior in MAX phases can be attributed to reversible glide of basal plane dislocation, both W_d and the onset stress for micro-yielding due to dislocation glide in soft grains should obey a Hall-Petch type dependency on the grain size, as it is discussed in more details elsewhere [37]

Section 2 of this manuscript, reconciles the three single mechanistic models and proposes that the cyclic compressive behavior of Ti_2AlC, can be divided into four stress regions, each with a different dominant hysteretic underlying mechanism [100]. Analysis

of the results obtained from cyclic compression testing of high purity Ti_2AlC in this study, more specifically changes of W_d and irrecoverable strain after first loading ($\Delta\varepsilon_{PL}$), in combination with the results of resonant ultrasound spectroscopy (RUS) and electron backscatter diffraction (EBSD) studies suggest the following stress regions with distinct mechanical response: (i) Regions I at the low stress range in which the mechanical response is linear elastic; (ii) Region II above micro-yielding stress denoted as $\sigma_{I\text{-}II}$ in which a small stress-strain hysteresis is observed during cyclic loading, in conjunction with a rapid increase in permanent deformation in the first loading and unloading cycle --- a behavior attributed reversible glide in soft grains; (iii) Region III at stresses higher than micro-yielding stress denoted as $\sigma_{II\text{-}III}$ and in which formation and movement of dislocation walls (DWs) give rise to cyclic hardening and increased hysteretic behavior; and (iv) Region IV at very high stresses exceeding some critical stress denoted as $\sigma_{III\text{-}IV}$ where microcracking appears and ultimately effects observed hysteretic behavior by increasing the total energy dissipated in each loading-unloading cycle. In addition, the results reported in Section 2.4 for two microstructures with different grain sizes, suggest that all transition stresses, namely $\sigma_{I\text{-}II}$, $\sigma_{II\text{-}III}$, $\sigma_{III\text{-}IV}$, and the compressive strength are function of grain size. In this section, the effect of microstructure including grain size and $TiAl_x$ intermetallic impurity on the ultimate compressive strength and hysteric behavior of Ti_2AlC at room temperature is investigated in more details. It is, to the author's knowledge, the first systematic study on the effect microstructure on the room temperature mechanical properties of MAX phases.

3.3 Experimental Procedures

The samples tested in this study were fabricated using three processing routes, utilizing powders synthesis in house as well as commercially available powders (MAXthal 211, Sandvik Heating Technology, Sweden) to produce samples with different grain sizes and various amounts of intermetallic impurities. The processing parameters for all samples are summarized in Table 3-2 and briefly describer below.

Commercial sample (CP-CG): commercially available Ti_2AlC (3-ONE-2, Voorhees, NJ) was prepared by cold compaction followed by pressureless sintering of MAXthal 211 at 1500 ^oC for 4 hour in the vacuum of 10^{-2} torr .

Commercial Powder (CP-FG): Spark Plasma Sintering (SPS)[3] (SPS25-10, Thermal Technology LLC, USA) was used fabricate high density samples from MAXthal 211 commercial powder. In short, the as-received powders were mounted in a graphite die and placed inside the SPS chamber. The sample was heated to 1300°C at 50°C min^{-1} for 15 minutes under an applied pressure of 100 MPa and cooled near to room temperature at a rate of 50°C min^{-1}.

Reacted Powder (RP): In an effort to produce higher purity Ti_2AlC, a two-step process was employed in which Ti_2AlC MAX phase powders were synthesis in-house followed by sintering in SPS. For the Ti_2AlC powder synthesis, Ti (99.5%, -325 mesh), Al (99.5%, -325 mesh) and TiC (99.5%, 2 μm) powders, all from Alpha Aesar, USA, were used. The powders were weighed to achieve a molar ratio of Ti:Al:C = 2:1.05:0.95

[3] Less common but more appropriately referred to as Electric Current Assisted Sintering (ECAS)

and mixed by ball milling for 24 hrs. The mixture was placed in alumina boats and sintered in a high vacuum tube furnace (GSL1600X, MTI Corporation, USA) at a calibrated temperature of 1400°C under UHP argon. The sintered compact of reacted powder was then drill milled and sieved to produce -170 mesh Ti_2AlC powders and processed in SPS to produce high density samples, by sintering for 45 minutes at 1300°C. Those samples are further denoted as fine grained or RP-FG. To explore the effect of grain size while maintaining an invariant amount of impurities, samples were further subjected to 8, 24, & 72 hours (further denoted as medium grained, coarse grained and extra coarse grained, or RP- MG, RP- CG, and RP- XCG, respectively.

Sintered Composite (SC): A set of samples were fabricated in which excess aluminum and titanium powders were added to pre-reacted in-house Ti_2AlC powders to produce Ti_2AlC samples with the higher amount of $TiAl_x$ with grain sizes comparable to the CS sample. Molar amounts of Ti and Al were added to result in approximately 18 vol% formation of $TiAl_x$. After weighing, the powders were mixed by ball milling for 24 hrs and processed in SPS at 1300°C for 20 minutes at 100 MPa.

Reaction Sintered (RS- SPS*):* The same powders as in the case of RP samples were mixed to yield Ti:Al:TiC ratio of 1:1.05:0.75 and ball milled for 24 hours. The powder mixture was compacted in graphite die and reaction sintered in SPS at 1450^oC for 20 minutes, as it was described elsewhere [97].

X-ray diffraction (XRD) spectra (not shown here) for all samples were collected using a diffractometer (D8 Discover, Bruker, USA) with Cu-Kα radiation at 40 kV and 40 mA in 8o– 80^o 2θ range with 0.024^o step and rate of 3.5 o/min. In addition, the

Table 3-2: Summary of processing conditions, amount and type of impurities, grain sizes and mechanical properties of all samples tested in this study. Note PS denotes pressureless sintering.

Sample	Powder Source	Sintering Technique	Post Heat Treatment	Secondary Phases Detected			Grain Size			Compressive Stress	Strain to Failure
							Length	Thickness	AR		
			(hr)	XRD	SEM/EDS	Vol % $TiAl_x$	(µm)	(µm)		(MPa)	(%)
CS-CG	Maxthal 211	PS 1500°C 4 hr	0	$TiAl_x$; Ti_3AlC_2; $Ti_5Al_2C_3$	$TiAl_x$; Ti_3AlC_2; $Ti_5Al_2C_3$; Al_2O_3	17	22 ±22	5 ±2.6	4.4	565 ±15	1.51 ±0.03
CP-FG	Maxthal 211	SPS 1300°C 15 min	0	$TiAl_x$ Ti_3AlC_2	$TiAl_x$; Ti_3AlC_2; Al_2O_3	7	4.2 ±2.5	2.1 ±1	2.1	1260 ±45	1.15 ±0.09
RP-FG	RP	SPS 1300°C 45 min	0	-	$TiAl_x$; Al_2O_3	3	6.1 ±2.8	4.6 ±2.2	1.4	1040 ±10	1.25 ±0.05
RP-MG	RP	SPS 1300°C 45 min	8	-	$TiAl_x$; Al_2O_3	3	13.9 ± 8	7.3 ±2.4	1.9	820 ±10	0.99 ±0.03
RP-CG	RP	SPS 1300°C 45 min	24	-	$TiAl_x$; Al_2O_3	3	17.4 ± 9.7	8.2 ±2.9	2.2	640 ±30	1.04 ±0.20
RP-XCG	RP	SPS 1300°C 45 min	72	-	$TiAl_x$; Al_2O_3	3	44.7 ±39.2	13.8 ±7.5	3.2	430 ±60	0.76 ±0.03
SC	RP + Ti + Al	SPS 1300°C 20 min	0	$TiAl_x$	$TiAl_x$; Al_2O_3	17	7.8 ±2.9	4.3 ±1.9	1.4	1110 ±20	1.40 ±0.08
RS- SPS	Ti + Al + TiC	SPS 1450°C 15 min	0	-	$TiAl_x$;	5	6.9 ±	4.5 ±	1.5-	1200 ±55	-

microstructure of the samples was characterized using a field emission scanning electron microscope (Quanta 600 FEG, FEI, USA) equipped with back-scattered electron detector (BSE) and Energy-Dispersive Spectroscopy (EDS) system (Oxford Instruments, UK). The volume percent of intermetallic impurities on the samples was calculated by performing Image Analysis (Image J software) of BSE SEM micrographs of polished, but unetched surfaces to avoid dissolution of intermetallic during etching process. The volume percent of $TiAl_x$ impurities was determined using:

$$Vol_{TiAl}\% = \left(\frac{Area_{TiAl}}{Area_{Total}}\right) * 100 \qquad (3.1)$$

In this study only titanium intermetallic phases $TiAl_x$ were accounted for because that was major impurity phases in all samples. In addition, since the MAX phase grains are plate-like, the length and thickness of more than 100 grains was measured in each of processed set of samples from SEM micrographs of polished and etched samples using Image J software. The density of the samples was measured by the alcohol (200 proof ethanol) immersion method based on Archimedes' principle that is described in more detail elsewhere [79, 80]. Relative density (not shown here) was found to exceed 98% for all sample.

Cylindrical samples, 5 mm diameter by 8 mm in length were cut by wire electron discharge machining (Wire-EDM) for quasi-static compression testing. The samples were tested in a servo-hydraulic testing machine (MTS-810, MTS, USA) under a constant crosshead displacement rate chosen to result in an initial strain rate of 10^{-4} s^{-1}. A high temperature axial extensometer (632.59, MTS, USA) was attached to WC spacers

placed between sample and pushrod. Since the extensometer was not placed directly on the sample, the strain in the sample was corrected using $\varepsilon_{eff}=\frac{GL*\varepsilon_{ext}}{L_o}$ where ε_{eff} is the effective strain in the sample, GL is the gauge length of the extensometer (15.24 mm), ε_{ext} is the strain measured by extensometer, and L_o is the sample's initial length. This simple correction assumes zero contraction of the spacers as well as perfect contact between sample and spacers, so the values of the strains reported are only approximations of the strain magnitudes experienced by the sample.

Cyclic compression testing was perform on all but the SC sample following the procedure outlined in more details in Section 2.3 [100], whereby cylindrical samples, 9 mm diameter by 16.5 mm in length were cut by Wire-EDM and tested on a servo-hydraulic testing machine (MTS-810, MTS, USA) at a frequency of 0.5 Hz. Strains were measured with an axial extensometer (632.13E-23, MTS, USA) directly attached to the sample while the sample was loaded and unloaded twice in each testing step to prescribed maximum load. A preload of 5 MPa was maintained while the stress amplitude was increased for 50 MPa in each testing step to failure. Resonant ultrasound spectroscopy (RUS) was used to measure the changes in Young's modulus after each testing step as described elsewhere [100] with the goal to determine the onset of its decrease due to microcracking of the samples.

3.4 Results and Discussion

3.4.1 Microstructure of As-Processed Samples

Representative BSE micrographs of polished and etched surfaces in Figure 3-2a-e illustrate different grain morphologies and sizes of selected samples in their as-processed state. Those and similar micrographs for other samples not shown in Figure 3-2a-e were used to measure length and thickness of more than 100 grains for each sample. The arithmetic mean values and standard deviation of grain lengths and thicknesses are listed in Table 3-2 for all as-processed samples, together with average aspect ratios (AR). Those results show that grain size in as-processed samples varied from 4.2 x 2.1 μm to 44.7 x 13.8 μm and that generally samples with larger grain sizes have a higher aspect ratio. Note that the grain size in RP samples increases from 6.1 x 4.6 μm in as processed sample (RP-FG) to 44.7 x 13.6 μm in the sample that was heat treated for 72 hour after sintering (RP-XCG). In addition, the aspect ratio in those samples increases monotonically with increasing grain size, as it is expected in MAX phases due to their anisotropic grain growth in which faster growth in the direction of basal planes is observed [3]. It is important to note that the grain size variation, as measured by the standard deviation increases with grain size. The larger the grain size, the higher the probability of finding a few grains much larger than the reported grain size such that the distribution of grain size would best approximated with log-normal distribution.

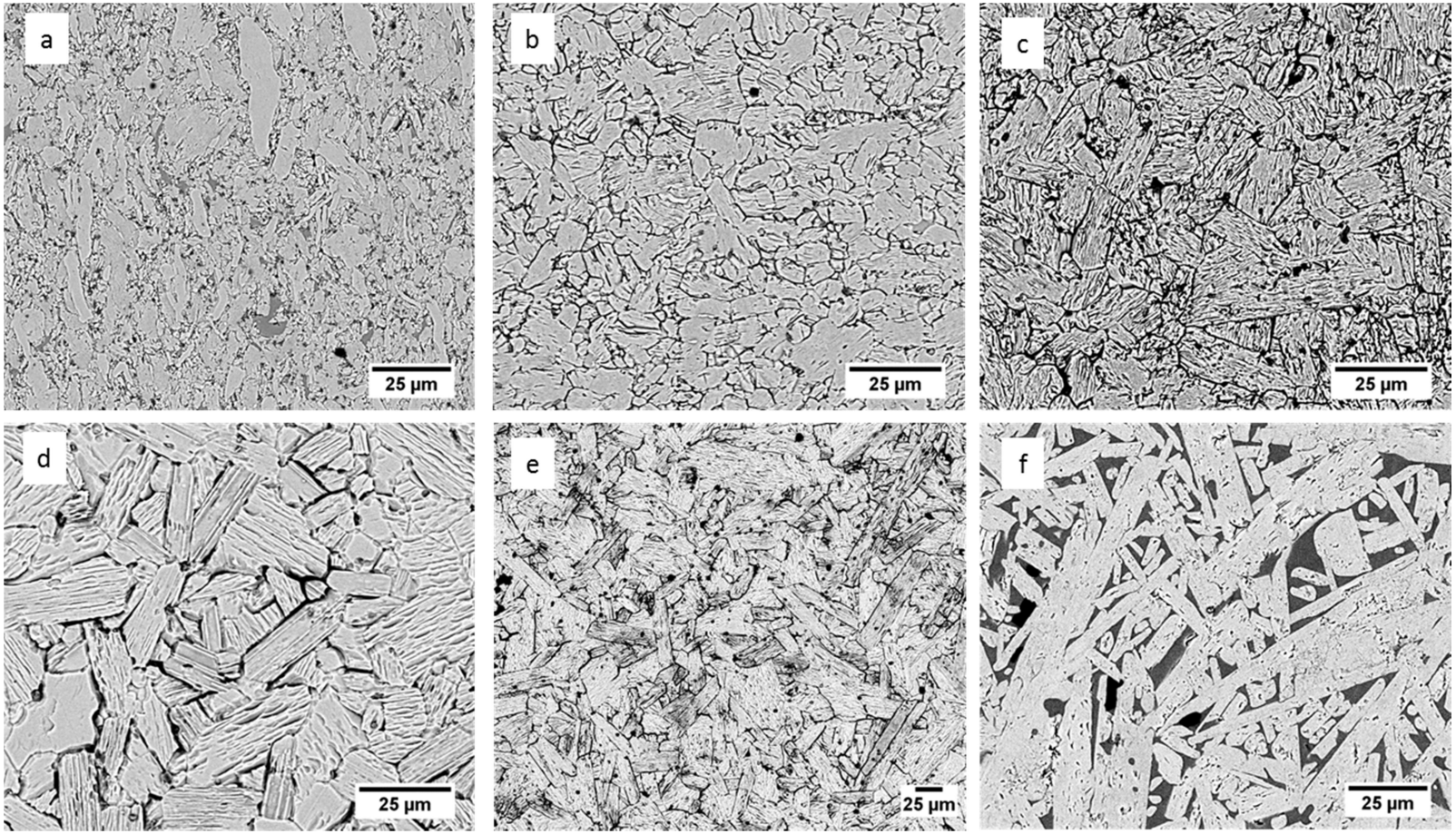

Figure 3-2: Selected but typical backscatter electron micrographs of examined samples: (a) etched CP-FG; (b) etched RP-FG; (c) etched RP-MG; (d) etched RP-CG; (e) etched RP-XCG and (f) unetched CS-CG where dark gray phase between Ti_2AlC grains in was identified by EDS as $TiAl_x$;.

XRD results (not shown here) did not reveal presence of any other phase but Ti_2AlC in most samples, Table 3-2. The only exceptions are CS-CG, CP-FG and SC samples in which different secondary phases, such as $TiAl_x$, Ti_3AlC_2 and $Ti_5Al_2C_3$ were also identified by XRD. Additional analysis of polished but unetched surfaces using BSE and EDS, revealed the presence of small amounts of other secondary phases, identified by EDS to be closest to Al_2O_3, $TiAl_x$, Ti_3AlC_2, and/or $Ti_5Al_3C_2$, even in XRD pure samples, Table 3-2. Since $TiAl_x$ was identified to be the major non-MAX phase[4] impurity in most of the samples (note that amount of Al_2O_3 in all samples was <1-2%), its amount was determined from BSE images of polished and unetched surfaces, such that shown in Figure 3-2f, using procedure described earlier. Results of that analysis listed in Table 3-2, shows that amount of $TiAl_x$ in processed samples varied between 3 vol% in RP-SPS samples to 17 vol% in CS-CG and SC samples.

3.4.2 Stress-Strain Response in Quasi-Static Compression

Selected but typical stress-strain curves in Figure 3-3, as well as average values of compressive strengths and strains at failure in Table 3-2, clearly illustrate large variations among mechanical responses of samples with different microstructures, i.e. processed using different routes**.** While at very low stresses (below 100-200 MPa) all samples behave almost identically in nearly linear-elastic manner, at higher stresses their

[4] Ti_3AlC_2 and $Ti_5Al_3C_2$ also belongs to the family of MAX phases and cannot be easily distinguished from Ti_2AlC on BSE images

mechanical behavior is quite different. In the case of the CP-FG sample, which has the smallest grain size, this behavior is brittle-like with failure at very small strains. Moreover, the CP-FG samples failed violently in brittle manner by shattering into

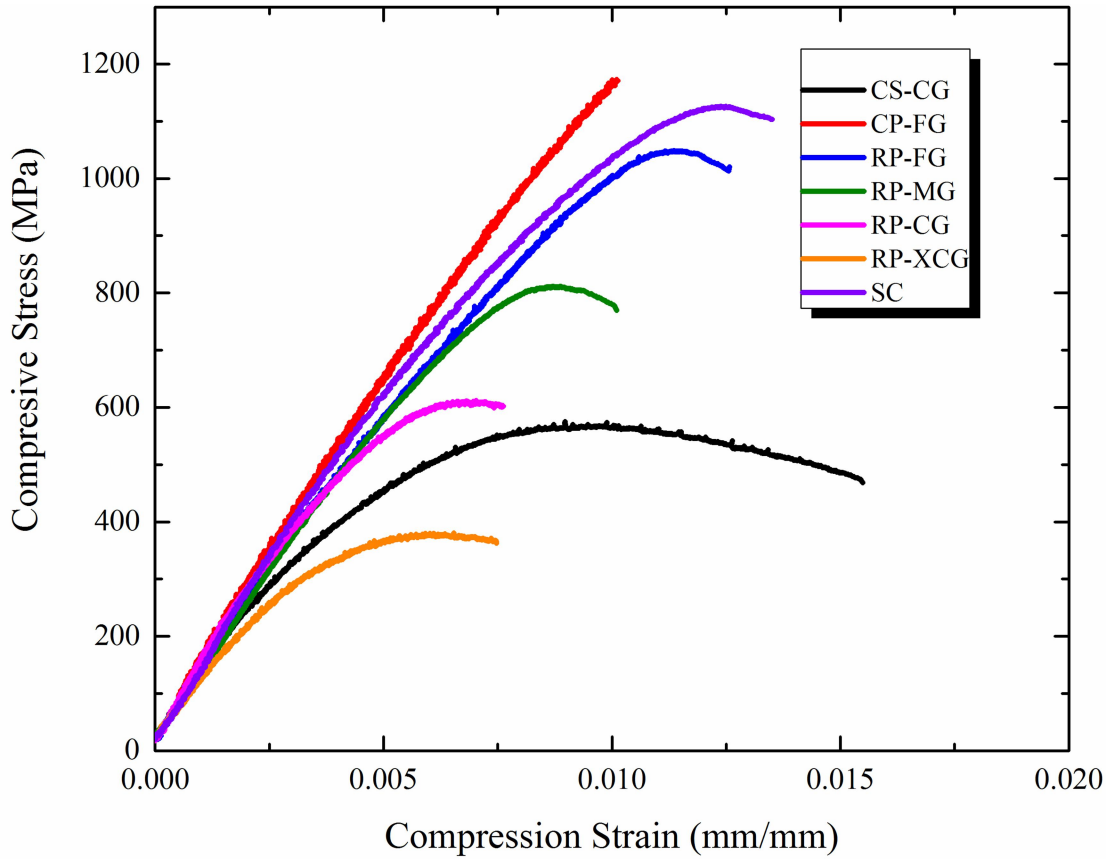

Figure 3-3: Selected but typical stress-strain curves obtained in quasi-static loading to failure.

many small pieces. However, the average compressive strength of 1260 MPa for CP-FG samples is the highest measured in this study and the highest ever reported for Ti_2AlC. In the other extreme are samples with very coarse grain structures, namely CS-CG and RP-XCG that have more quasi-ductile behavior and significantly lower compressive

strengths. These samples usually fracture into two pieces, with typical fracture occurring close to 45° relative to the direction of applied load, indicating failure by shear band formation [20, 101]. In addition, in the samples with the two largest grain sizes, the two fracture pieces remained weakly attached to each other after failure. The latter is attributed to the effect of crack bridging that has been previously observed in coarse grain MAX phases structures [43]. Note that CS-CG shows the most gracefully failure and largest strains to failure, for the reasons that are discussed in more detail at the end of this section. The mechanical responses of all other samples (Figure 3-2 and Table 3-2) lie in between those two extremes (i.e. very fine and very coarse grained structures) and they show some moderate softening before final graceful failure.

The average compressive strengths of all samples tested in this study are plotted in Figure 3-4 as a function $1/\sqrt{l}$ and $1/\sqrt{t}$ where l and t are average grain length and thickness, respectively, from Table 3-2**.** For comparison, previous reported values of compressive strengths listed here in Table 3-1 are also plotted in Figure 3-4, only if average grain length and thickness were reported in original work. A linear regression fitting of only the results obtained in this study is plotted in Figure 3-4a using Hall-Petch type of relationship between compressive strength (σ_f) and the average grain length and of the following form:

$$\sigma_f = \sigma_0 + k_f * l^{-1/2} \qquad (3.2)$$

yields Hall-Petch constant of σ_0 = 70.5 MPa and k_f = 2633 MPA/$\sqrt{\mu m}$ with R^2 = 0.95. However, no correlation was found between the compressive strength and average grain

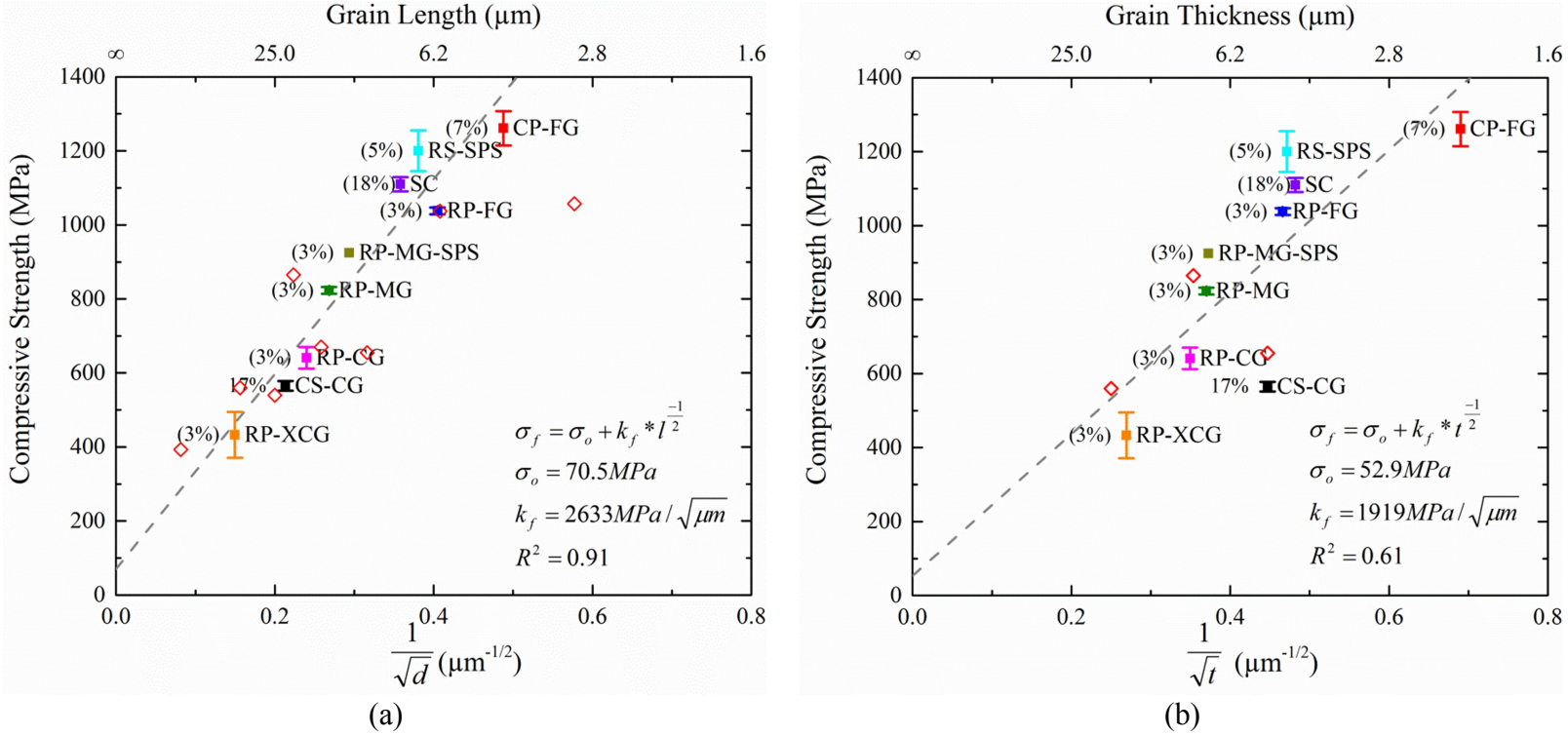

Figure 3-4: Average compressive strength of Ti_2AlC plotted in Hall-Petch manner as a function of (a) $1/\sqrt{l}$ where l is the average length and (b) $1/\sqrt{t}$ where t is average grain thickness . Error bars indicate standard deviation in compressive strengths. Dashed line represent best fitting line of results obtained in this study. Numbers in parenthesis denote vol% of $TiAl_x$ impurities in each sample. For comparison, some reference values published before and listed in Table 3-2 are also plotted as open red symbols.

thickness, t. Fitting results in Figure 3-4b using similar Hall-Patch relationship, i.e. $\sigma_f = \sigma_o + k_f * t^{-1/2}$ yields very low value of R^2=0.61, suggesting no correlation between compressive strength and thickness of the grains. The possible underlying failure mechanisms responsible for the observed Hall-Petch type relationship between compressive strengths and grain lengths in Ti_2AlC are discussed in more details in the next section.

At the end of this section effect of $TiAl_x$ impurities on mechanical behavior of Ti_2AlC in compression has to be addressed in more details. Results in Figure 3 together with good fitting results using Hall-Petch type equations, clearly shows that amount of $TiAl_x$ impurities (up to 17 vol%) does not affect significantly the compressive strength. However, that the presence of higher amount of $TiAl_x$ contributes the larger strains to failure. For example, the CS-CG sample and SC sample both with high (≈ 17 vol% $TiAl_x$) exhibit the higher strains to failure. Note that $TiAl_x$ is less stiff (E=176-184 GPa, G = 70-76 GPa [102]) and rather ductile [103] compared to Ti_2AlC and has the potential to enhance the strain to failure by plastically deforming. Moreover it has been shown that cracks do not propagate through $TiAl_x$ when present on other MAX phases [104] . It is important to note that this response is not observed on the CP-FG sample, is probably due to its fine grain size and the fact that $TiAl_x$ in these samples is limited to isolated pools thereby hindering its ability to shield damage.

3.4.3 Cyclic Compression Testing

In general, Hall-Petch relationship, such as that in Equation (3.2), is usually used to describe the relationship between: (i) yield stress and grain size in dislocation-based ductile material when yielding is controlled by dislocation glide in multiple slip systems and hindered by grain boundaries; and (b) strength and grain size in brittle materials with limited number of slip systems and/or high CRSS when strength is controlled by microcracks having sizes close to the grain size [105-108]. However, in MAX phases, taking a middle ground between ductile metals and brittle ceramics, the nature of this relationship is much more complex. It has been recently showed [100], that mechanical behavior of Ti_2AlC is characterized by three micro-yielding stresses, namely $\sigma_{I\text{-}II}$, $\sigma_{II\text{-}III}$, and $\sigma_{III\text{-}IV}$, as it is briefly described in introduction of this section.

Following the very same procedure used in the previous section [100], selected samples from Table 3-2, namely CS-CG, CP-FG, RP-FG, RP-MG, RP-CG, RP-XCG, were exposed to series of cyclic loading test in compression and complemented by elastic modus measurements by RUS. Results of this exercise are summarized for select samples in Figure 3-5 showing changes of energy dissipated per each loading cycle per unit volume (W_d), opening of the first loop or irrecoverable strain ($\Delta\sigma_{PL}$) after each subsequent loading to higher stress, and relative Young's modulus (relative is defined as the ratio of Young's' modulus of untested sample to Young's modulus of stressed sample) with σ^2, where σ is maximum stress in each loading cycle. Those results were used to determine following characteristic stresses:

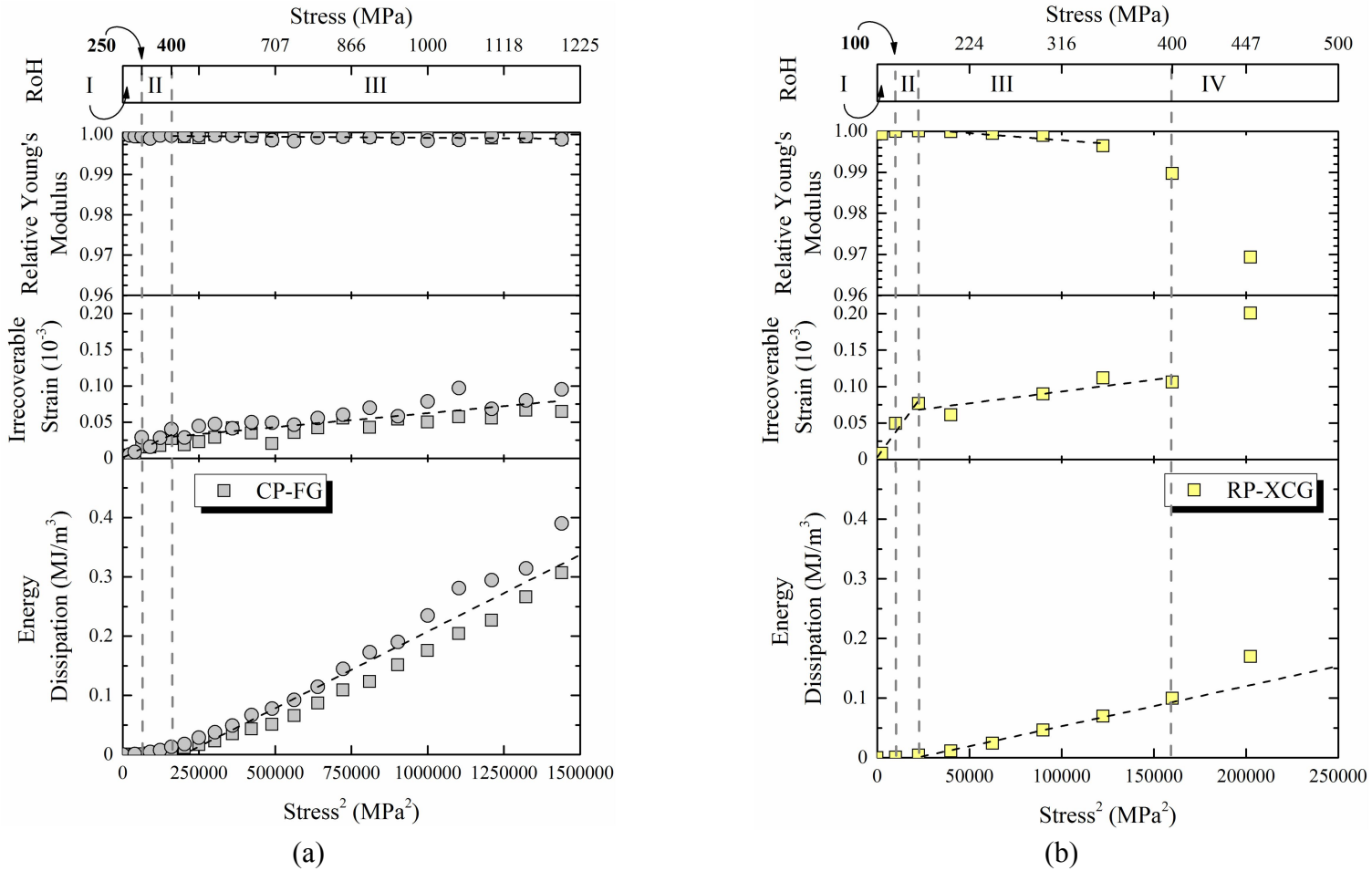

Figure 3-5: Selected but typical results of cyclic testing in compression of (a) sample CP-FG and (b) sample RP-XCG. Bottom plots: W_d as a function of σ^2; Middle plots: $\Delta\sigma_{PL}$ as a function of σ^2; Top plots: Relative Young's modulus as a function of σ^2. Topmost scales indicate stress regions with different mechanical behavior observed in this study, while dash lines denote micro-yielding stresses $\sigma_{I\text{-}II}$, $\sigma_{II\text{-}III}$, and $\sigma_{III\text{-}IV}$. Squared and circular symbols denote results obtained using two different samples for both microstructures.

- $\sigma_{I\text{-}II}$ as an onset Region II in characterized by small hysteresis loops and steep increase in $\Delta\sigma_{PL}$ with σ^2;
- $\sigma_{II\text{-}III}$ as an onset of Region III in which W_d scales linearly with σ^2 as predicted by KNE model [28, 61, 62], while cyclic hardening causes much gradual increase in $\Delta\sigma_{PL}$ with σ^2 than in Region II;
- $\sigma_{III\text{-}IV}$ as an onset of Region IV characterized by elastic modus drop of approximately more than 0.2% with σ^2 as a result of microcracking and pronounce upward deviation of W_d from the predict linear dependence with σ^2;
- σ_f as maximum compressive strength after series of cyclic loading;

The four characteristic stresses $\sigma_{I\text{-}II}$, $\sigma_{II\text{-}III}$, $\sigma_{III\text{-}IV}$ and σ_t are plotted as a function of $1/\sqrt{l}$ and $1/\sqrt{t}$ in Figure 3-6, to explore if they follow a Hall-Petch type relationship. Note that the characteristic stresses plotted in Figure 3-6 were calculated as average values determined from testing two samples of each microstructure. In addition, results of linear regression fitting assuming Hall-Patch type relationship are also denoted by dashed lines in Figure 3-6**,** together with the corresponding fitting equations and R^2 values. Those results clearly indicate that all characteristic stresses plotted as a function of grain length in Figure 3-6a, follow a Hall-Petch type relationship as all R^2 values exceed 0.9. However, it seems that only $\sigma_{I\text{-}II}$ and $\sigma_{II\text{-}III}$ show Hall-Petch type dependence on grain thickness as indicated by high R^2, refer to Figure 3-6b. Once again, $\sigma_{III\text{-}IV}$ and σ_f correspond to the onset of microcracking and failure, do not scale with grain thickness.

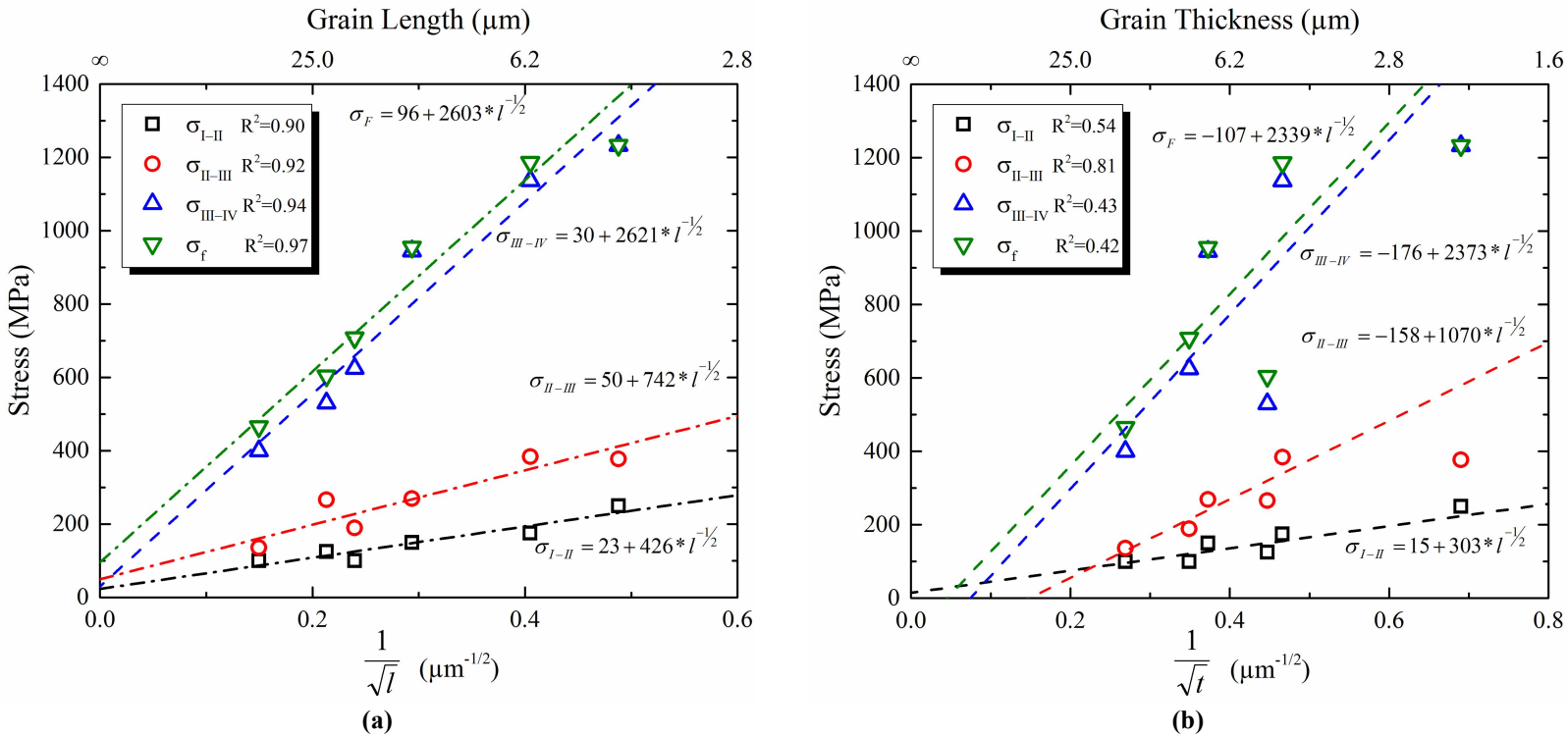

Figure 3-6: Characteristic stresses for the stress Regions as function of inverse square root of (a) grain length and (b) grain thickness. Corresponding Vol% of $TiAl_x$ in each sample is labeled next to the each data-point.

As it was discussed in more detail in section 2.4.2 and in [100], $\sigma_{I\text{-}II}$ denotes the onset of plastic flow in soft grains by dislocation glide in basal planes. The latter is accommodated by the development of elastic residual stresses in hard grains in the similar way as it is proposed by the RF model [37]. Basal plane dislocations in soft grains pile up against grain boundaries with hard grains, and in MAX phases the size of the planes scale with the length of the grain. Following original works of Hall and Patch [106, 109-111], it is reasonable to assume that the micro-yielding stress $\sigma_{I\text{-}II}$ in polycrystalline Ti_2AlC can be expressed as:

$$\sigma_{I\text{-}II} \approx M \cdot \tau_{HP} = M \cdot \left(\tau_{PN} + k_{I\text{-}II} * l^{-1/2}\right) = \sigma^0_{I\text{-}II} + k'_{I\text{-}II} * l^{-1/2} \qquad (3.3)$$

where M is Taylor factor, τ_{PN} is Peierls-Nabarro stress (assumed here to be equal to CRSS for basal plane), $k_{I\text{-}II}$, $k'_{I\text{-}II}$, and $\sigma^0_{I\text{-}II}$ are constants. Since the best fitting result yields $\sigma^0_{I\text{-}II}$=23 MPa, it can me shown τ_{PN}=7.7 MPa, assuming M =3 for polycrystalline material with random distribution of orientation of grains. Note that CRSS is much lower than that of ≈ 24 MPa estimated for Ti_2AlC using the KNE model [28], or that ≈ 36 MPa measured in compressive testing of Ti_3SiC_2 quasi-single crystals [20]. The constant $k'_{I\text{-}II}$ can be expressed as [105]:

$$k'_{I\text{-}II} = M \cdot \sqrt{\frac{2Gb\tau_c}{k\pi}} \qquad (3.4)$$

where G and b are shear modulus and Burgers vector, respectively, k is constant equal to 1 for screw and (1 - ν) for edge dislocations, ν is Poisson's ratio, and τ_c is effective stress at the head of the pile-up acting on the grain boundary. Since k'_{I-II}=425.77 MPa/$\sqrt{\mu m}$, it can be shown that τ_c yields of 2.6 GPa for screw and 2.2 GPa edge dislocation pile-ups, assuming M = 3, G = 120 GPa, b = 3.05 x 10^{-4} μm and ν = 0.17 [3]. Note that those values are well below theoretical strength (σ_{th}) that can be estimated to be $\sigma_{th} \approx E/10$=28 GPa. Furthermore, the number of dislocations in the pile-up can be calculated as $n = \frac{\pi l \tau_C}{2Gb}$ for calculated values of τ_c [105]. Therefore, it can be shown that n is equal to 477 for screw and 405 for edge dislocations assuming grain length of 10 μm. Furthermore, those numbers yield reasonable dislocation densities (ρ_{dis}) in soft grains of 1.2 x 10^{13} m/m^3 for screw and 1.0 x 10^{13} m/m^3 for edge dislocations, if their length is equal to the grain length l in soft grains having size of 10 x 5 μm.

The micro-yielding stress σ_{II-III} denotes the onset of Region III [100], in which geometrically necessary dissociations (GND) are generated in all grains, including those with hard orientation, to accommodate basal slip in the soft grains, as proposed elsewhere [112, 113]. Previous Electron-Backscatter Diffraction (EBSD) studies [100], show that most of them arrange in straight DWs or loops resembling IKBs. Assuming that those dislocations form as proposed in kinking model originally developed by Orowan [15] Frank and Stroh's [16] kinking model, and further incorporated into the KNE model for the MAX phases [61, 63-65], the relationship between stress and grain size in this region can be expressed as:

$$\sigma_{II\text{-}III} \approx M \cdot \tau_{FS} = M \cdot \left(k_{II\text{-}III} * t^{-1/2}\right) = M \cdot \sqrt{\frac{4G^2 b\gamma_c}{\pi^2} \ln\left(\frac{b}{\gamma_c w}\right)} \cdot t^{-1/2} = k'_{II\text{-}III} \cdot t^{-1/2} \quad (3.5)$$

where τ_{FS} is critical stress to nucleate kinks [16], γ_c is critical kinking angle, w is dislocation core width, $k_{II\text{-}III}$ and $k'_{II\text{-}III}$ are constants, and the other symbols have their usual meaning. Note that Equation (3.5) is derived assuming that IKB length (2α) is equal to the grain thickness, as it is done in the KNE model [61, 63-65], and thus $\sigma_{II\text{-}III}$ should be a function of t, and not l, as in Region II. Following the KNE model, the critical kinking angle in Equation (3.5) can be calculated to be $\gamma_c \approx \frac{3\sqrt{3}(1-\upsilon)}{8\pi e}\left(\frac{b}{w}\right) = 0.013$ rad assuming w = 5·b [28]. For that critical angle and M = 3, $k'_{II\text{-}III}$ in Equation (3.5) yields value of 737 MPa$\sqrt{\mu m}$, which is in reasonably good agreement with the slope of 630 MPa$\sqrt{\mu m}$ obtained by fitting $\sigma_{II\text{-}III}$ vs. $t^{-1/2}$ data in Figure 3-6b. Also note that fitting of those results yields the negligibly small intercept stress of -1.8 MPa at $t^{-1/2}$=0, essentially approximated to be zero. The latter is also in good agreement with the model depicted in Equation (3.5).

At stresses exceeding transition stress $\sigma_{III\text{-}IV}$, stress concentrations due to dislocation pile-ups on grain boundaries or DWs lead to the formation of Zener-Stroh type cracks [67-69]. These cracks cause the sudden drop of relative elastic modulus and contribute to the energy dissipated in per cycle, as it discussed in more details in the previous section [100]. Following the treatment given by Davidge [114], the stress to

open cracks at the grain boundary can be expressed in the form of the Hall-Petch relationship as:

$$\sigma_{III\text{-}IV} \approx M \cdot \tau_{III\text{-}IV} = M \cdot \left(\tau_{PN} + k_{III\text{-}IV} * l^{-1/2}\right) = \sigma^{0}_{III\text{-}IV} + k'_{III\text{-}IV} * l^{-1/2} \qquad (3.6)$$

where $\sigma^{0}_{III\text{-}IV}$ and $k'_{III\text{-}IV}$ are constants. The latter can be further expressed as:

$$k'_{III\text{-}IV} = M \cdot \sqrt{\frac{E \cdot b \cdot \sigma_{th}}{2(1+\nu)}} \qquad (3.7)$$

here σ_{th} is theoretical strength. Equations (3.6) and (3.7) were derived assuming that the failure stress is a result of stress concentration caused by edge dislocation pileup on a grain boundary, and that when such pileup (under stress) produces a tensile stress equal to or greater than the theoretical fracture strength, σ_{th}, then fracture occurs [114]. Note that expressing stress as a function of l in Equation (3.6), dislocations can pile up only along basal planes and that their length scales with grain length l. Since $\sigma^{0}_{III\text{-}IV}$ = 30 MPa from fitting results in Figure 3-6a, τ_{PN} can be calculated to be 10 MPa from Equation (3.6) assuming M = 3. This value is in good agreement with τ_{PN} of 7.7 MPa that was obtained from Hall-Petch treatment of $\sigma_{I\text{-}II}$ micro-yielding stress using Equation (3.2). In addition, best fitting $\sigma_{III\text{-}IV}$ stresses plotted in function of $l^{-1/2}$ in Figure 3-6a, gives value of $k'_{III\text{-}IV}$ = 2621.4 MPa$\sqrt{\mu m}$. For this value of $k'_{III\text{-}IV}$ and M = 3, Equation (3.7) gives σ_{th} of ≈ 21 GPa which is close, but below that estimated earlier to be $\sigma_{th} \approx E/10 = 28$ GPa. Since Ti_2AlC phases are layered compounds that usually fracture

along basal plans with "weaker" Ti-Al bonds when compared to Ti-Ti or Ti-C bonds, it is reasonable to conclude that the theoretical strength determined earlier from E gives slightly overestimate values for fracture along basal planes.

Figure 3-6a also shows that fracture stress σ_f obtained after cyclic loading testing in compression is just slightly higher than that $\sigma_{III\text{-}IV}$, suggesting that once microcracks forms in the stress Region III, they propagate quite rapidly with increasing stress resulting in final failure. Note here that constants σ_0 and k_f in Figure 3-6a that were determined by fitting σ_f vs. $l^{-1/2}$ data from cyclic compressive testing using Hall-Patch type equation (Equation (3.2), yields values close to those given in Figure 3-4 for quasi-static testing. Latter suggest that loading history does not affect significantly strength of Ti_2AlC, and even more importantly confirms once again that microcracks most likely do not form and propagate during cyclic loading to stresses below $\sigma_{III\text{-}IV}$.

Note that excellent fitting of result in Figure 3-6 has been achieved using different Hall-Petch like relationships for micro-yielding stresses as it is indicated by high R^2 values[5], regardless of the fact that the two samples contained relatively large amount of $TiAl_x$ impurities, namely 7 and 17 vol%. This indicates that presence of $TiAl_x$ does not affect significantly values of ether micro-yielding stresses or compressive strength. The latter does not mean that $TiAl_x$ does not affect hysteretic behavior of Ti_2AlC.

[5] the only exceptions are plots of σ_{III-IV} and σ_t vs. $t^{-1/2}$ in Figure 5b for the reasons that were discussed in more detail earlier.

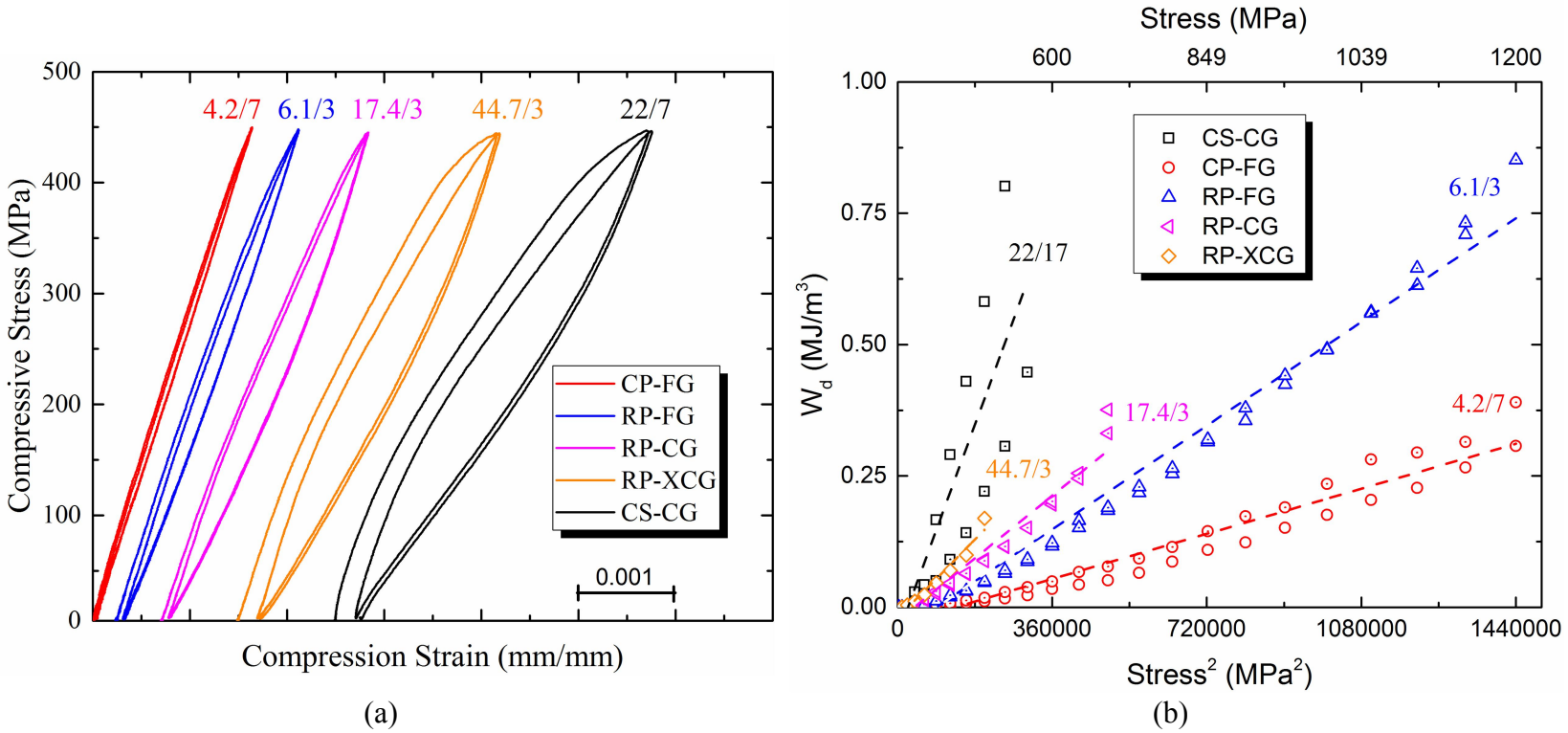

Figure 3-7: (a) Selected but typical cyclic stress-strain response samples with different microstructures load to a maximum stress of 450 MPa; (b) W_d vs. σ^2 plot with linear regression fitting for samples with different microstructure. Labels on both plots shows grain length in μm / vol% of $TiAl_x$ for different samples.

Figure 3-7 clearly shows that that both the opening of the first loop ($\Delta\varepsilon_{PL}$) and the area of subsequent hysteresis loops (i.e. W_d) increase with the grain size, which is in good agreement with previous results and current understanding of underlying hysteric mechanisms in MAX phases [100]. This figure also illustrates the significant effect that the amount of $TiAl_x$ impurity has on $\Delta\varepsilon_{PL}$ and W_d. For example, sample CS-CG containing 17 vol% $TiAl_x$ of has significantly smaller grain size that sample RP-XCG containing only 3 vol% of $TiAl_x$, yet it has largest opening of the first loop and dissipates significantly much more energy per cycle.

Analysis of the results such as those shown in Figure 3-5 for all samples tested here[6], yield a similar conclusion. This finding is also in good agreement with previously publish studies on hysteretic behavior of MAX phase – metal composites, such as Ti_2AlC-Mg [33, 34, 77] and Ti_3SiC_2-NiTi [35]. Although this observation is not fully understood at this moment, it is reasonable to conclude here that the addition of less stiff and more ductile phase results in higher both irrecoverable and recoverable strains during loading, and thus large hysteresis loops when compared to pure MAX phase.

3.4.4 Conclusions

Ti_2AlC samples with a wide range of different microstructures, i.e. different grain sizes and amount of $TiAl_x$ impurities, were tested in compression at room

[6] Note that only some typical but selected results are highlighted in Figure 3-5 because of the limited space.

temperatures. It was found that the room temperature cohesive strength scales with $l^{-1/2}$, where l is grain length, obeying Hall-Petch type relationship. No correlation was found between the compressive strength and grain thickness. Coarse grain structures and the contents of well dispersed $TiAl_x$ were found to enhance the strain to failure and fail in more graceful manner.

This work also confirms that stress-strain hysteresis in Ti_2AlC can be divided into four stress Regions, each with distinct underlying mechanism that show different dependence on grain size. Results presented here show that magnitude of micro-yielding stress σ_{II-III}, dividing Region I with linear elastic behavior from Region II with hysteretic stress strain behavior, depends on the grain length as it is expected assuming a Hall-Patch relationship. This microyield stress marks the onset of basal plane dislocation glide in soft grains, i.e. grains that are favorably oriented for easy slip relative to applied load. Transition stress σ_{II-III}, dividing stress Regions II and III with greatly different hysteretic behaviors, shows linear increase with $t^{-1/2}$, where t is average thickness of the grains. Results of the analysis provided herein, suggest that above this stress, geometrically necessary dislocation forms in all grains, including those with hard orientation, to accommodate initial plastic flow in soft grains. Assuming that those dislocations forms as predicted by kinking model that was proposed originally by Orowan [15] and Frank and Stroh [16], and further employed in KNE model by Barsoum [28, 29, 33, 61, 62] to explain hysteretic behavior of MAX phases, results in very good agreement between experimentally determined change σ_{II-III} with grain size

predictions of the KNE model. At even higher stresses exceeding transition stress σ_{III-IV}, a reasonably good agreement between observed changes of σ_{III-IV} with grain length and models based on formation of Zener-Stroh crack is reached, suggesting that this onset stress of stress Region III is stress at which microcracking stars. This finding is in good agreement with previous results [100], that show a significant drop in elastic modulus within Region III as a result of damage accumulation. Last but not least, critical resolve shear stress of ≈ 8 - 10 MPa was determined from two different Hall-Perch type relationships independently, that relating σ_{I-II} and σ_{III-IV} to the grain length.

Last but not least, results of this study clearly showed that the amount of $TiAl_x$, a common impurity in Ti_2AlC, does not affect significantly the magnitude of micro-yielding stresses σ_{I-II}, σ_{II-III} and σ_{III-IV} up to amount of at least 17 vol%. However, larger amounts of $TiAl_x$ where found to results in higher values of irrecoverable strains after micro-yielding and much larger stress-strain hysteresis loops.

4 HIGH TEMPERATURE MECHANICAL PROPERTIES

4.1 Synopsis

This section investigates the compressive strength of Ti_2AlC from room temperature to 1100°C. A Hall-Petch like relationship was observed between the compressive length and the grain lengths that decreases monotonically with temperature and that deviate above the brittle to plastic transition temperature BPTT. Results from post-mortem EBSD analysis reveal the complex development of microstructure in both fine and coarse grain samples during loading at different temperatures. The pronounced drop in compressive strength for fine grain structures through the BPTT is in part attributed to grain reorientation for easy slip as detected by EBSD. Significant grain refinement was also observed for both the fine grain and the coarse grain structures as a function of the deformation temperature. In coarse grain structures, the refinement is observe to begin even at room temperature and is attributed to the higher incompatibility stresses that get relaxed in the form of KB and delamination resulting only on a gradual degradation of strength and pseudoductile failure.

4.2 Introduction

Mechanically, the MAX phases can be hardly classified as typical metals or ceramics since they show pseudoductile behavior in constrained deformation modes, in highly oriented microstructures, and at higher temperatures while in unconstrained

deformation, especially in tension and at lower temperatures, they behave more like typical brittle ceramics [2-4, 26]. It is fairly well established (see previous sections) that understanding the nature of the dislocations in the MAX phases --- how they form, assemble and annihilate --- is essential for understanding their response to applied stress. The majority of transmission electron microscopy (TEM) studies show that the dislocations in MAX phases are numerous, but constrained to the basal and only the basal planes with Burgers vector of $b = \frac{1}{3}\langle 11\bar{2}0\rangle$ [19, 115, 116]. In addition, basal plane dislocations can arrange themselves either in dislocation walls (DWs), e.g., as low-angle (LAGB) or high-angle grain boundaries (HAGB), normal to the basal planes, or in arrays parallel to the basal planes or dislocation pile ups (DP) [19, 116]. The fact that dislocations in MAX phases are numerous and mobile, but constrained only to the basal planes, renders MAX phases highly plastically anisotropic. Therefore, large internal stresses and incompatibility stress states rapidly develop in polycrystalline MAX phases under applied stress, as the favorably oriented, or soft grains deform easily by dislocations glide in basal planes. The latter in turn rapidly transfers the load to the hard grains, i.e., those grains not favorably oriented for slip relative to the direction of the applied load [21, 37, 100, 117, 118]. However, what makes the MAX phases different from the other brittle materials with limited number of slip systems is that they can deform additionally by kinking and formation of kink boundaries (KB). The latter are believed to first nucleate as incipient kink bands (IKB), and then, further grow to fully developed KBs consisting of pairs of DWs of opposite sign [4, 14, 17, 27]. The end result of this process is the formation of two regions of lattice curvature in the grains

deformed by kinking that are separated from each other by well-defined kink boundaries. Therefore, MAX phases do not fail very rapidly due to the buildup of incompatibility stresses and the rapid formation of Zener-Stroh type crack [67-69] in boundaries between the hard and the soft grains like other brittle materials with limited number of slip system, but rather gracefully in pseudoductile manner, especially coarse-grained ones in which the KB form easier and at lower applied stresses [4].

Another implication of the plastic anisotropy of MAX phases is their room temperature hysteretic stress-strain behavior which is quite unusual for elastically stiff materials. It is well documented that when MAX phases are subjected to cyclic loading at room temperature, regardless if it is in tension or compression, their stress-strain response is non-linear elastic and hysteretic, with all but the first stress-strain hysteresis loops being closed, reversible and reproducible [26-30, 100, 117]. At low applied stresses, their hysteretic behavior can be attributed to the easy buildup of residual elastic lattice strains in the hard grains upon initial loading as a result of the anisotropic deformation and the easy yielding and flow of only the soft grains. These residual strains are sufficient to drive the reverse plastic flow of the soft grains, giving rise to very small permanent or plastic strain in the first loading-unloading cycle, and small hysteresis loops in any subsequent loading cycle [21, 37, 100, 117]. At high applied stresses, numerous DWs and KBs form during first loading cycle, even in grains with hard orientation, leading to some cyclic hardening and a much larger energy dissipation per loading cycle most likely as a result of movement (bowing) of dislocations in DWs, IKBs or KBs [100, 117].

At higher temperatures, all the MAX phases tested to date show a strain-rate dependent brittle-to-plastic transition, usually at temperature between 900 – 1100°C [119]. Above brittle to plastic transition temperatures (BPTT), they can be deform to strains exceeding 25%, in both tension and compression, and their stress-strain response becomes highly strain rated dependent [26]. This, together with the fact that all MAX phases tested to date exhibit a well-established secondary creep regime with constant creep rate, suggests that their mechanical response above the BPTT can, in a nutshell, be explained as controlled by the competition between the rate at which internal stresses accumulate and the rate at which they relax [7, 41, 46, 120]. In other words, similar to some other plastically anisotropic materials, such as hexagonal ice [121], when loaded fast essentially brittle failure occurs at very low strains even above the BPTT; however when loaded slowly, they creep and can deform to large strains before failure. In general, the origin of internal (incompatibility) stresses can be traced back to their plastic anisotropy and the formation of dislocation pile ups, DWs and KBs, as it is described earlier [100, 117]. The latter also leads to cyclic hardening with increasing number of loading cycles that was observed above the BPTT while cyclic loading to the same amplitude stress [27, 45]. However, the nature of the relaxation of internal stresses is still a subject of debate. Based on the fact that the fracture toughness of MAX phases drops above the BPTT, unlike other typical materials exhibiting brittle-to-ductile transition due to the activation of additional slip systems, Barsoum and co-workers proposed that those stresses are relaxed by temperature dependent grain boundary decohesion and/or delamination [4, 27, 42, 122]. This conclusion was further supported by the fact that a

significant fraction of the large strains observed during loading above the BPTT can be attributed to the accumulated damages [26, 120]. Most recently, Guitton et al. [21], showed evidence of cross-slip in prismatic and pyramidal planes in post mortem TEM studies of Ti_2AlN loaded at 900 ^oC, and proposed that an increase of available glide systems at high temperature (basal, prismatic and pyramidal planes) is likely to promote significant ductility at high temperatures. They also concluded that the activation of cross-slip must play a key role in the appearance of the brittle-to-plastic transition temperature. Last but not least, although grain boundary sliding was proposed as a possible mechanism for relaxation of internal (incompatibility) stresses [4], there is no experimental evidence that it occurs above the BPTT in any of the MAX phases.

The current understanding of high-temperature mechanical behavior of MAX phases comes mostly from the work carried out on Ti_3SiC_2, which is the most characterized compound out of the more than 70 MAX phases known to date [2]. However, over the last couple of years, Ti_2AlC was identified as one of the most promising MAX phases for high temperature applications due to a self-forming, protective, and self-healing α-Al_2O_3 layer in both in air and high humidity environments [8-13, 50]. Although a recent work showed that the mechanical response observed in Ti_3AlC_2 both below and above the BPTT can be, in many aspects extended qualitatively to Ti_2AlC, it was also demonstrated that the microstructure of Ti_2AlC plays an important role in the mechanical behavior above the BPTT, since its creep rate scatters within an order of magnitude for samples prepared using different processing routes [7]. In this section, the mechanical response of high purity Ti_2AlC of various grain size and those

containing some $TiAl_x$ impurities were systematically studied under compression at temperatures ranging from room temperature to 1100 ^oC. Selected samples were also studied by electron backscatter diffraction (EBSD) to elucidate the development of microstructure after loading at different temperatures.

4.3 Experimental Methods

Two different Ti_2AlC powder sources were used to prepare samples in this study, namely commercial powders (MAXthal 211, Sandvik Heating Technology, Sweden) and in-house reacted powders. The commercial powders were densified by spark plasma sintering (SPS) [7] at 1300°C for 15 minutes under UHP Argon and with applied pressure of 100 MPa to yield samples with fine grain size and of high density. The in-house reacted powders (further denoted as RP) were prepared by mixing elemental powders of Ti (99.5%, -325 mesh) Al (99.5%, -325 mesh) and TiC (99.5%, 2μm) (all from Alpha Aesar, USA) in molar ratio of Ti:Al:TiC = 1.00:1.05:0.95. The powder mixtures were pressureless sintered in a tube furnace (GSL1600X, MTI Corporation, USA) at 1400°C under UHP argon and subsequently drill milled and sieved to produce -170 mesh Ti_2AlC powders. The RP powders were densified using by SPS at 1300 ^oC, for 45 minutes, with some samples additionally heat treated for 8 or 24 hours at 1300°C in the tube furnace and under Argon atmosphere to produce samples with coarse grain size. In addition, one set of samples (denoted as CS) was prepared by cold compaction followed by

[7] Less commonly but more accurately referred to as Electric Current Assisted Sintering (ECAS)

pressureless sintering of MAXthal 211 at 1500 ^{o}C for 4 hour under vacuum of 10^{-2} torr. Processing details of the full set of samples is summarized in Table 4-1.

The density of the samples was measured by the alcohol immersion method, utilizing 200 proof ethanol, based on Archimedes' principle using the procedure outlined elsewhere [79, 80]. X-ray diffraction (XRD) spectra were collected with a diffractometer (D8 Discover, Bruker, USA) to complement phase identification and quantification. The XRD spectra were acquired with Cu-Kα radiation at 40 kV and 40 mA in 8o– 80^{o} 2θ range with 0.024^{o} step and rate of 3.5 o/min. Microstructural characterization of polished and etched samples was carried out using field emission scanning electron microscopy (Quanta 600 FEG, FEI, USA) equipped with back-scattered electron detector (BSE) and energy-dispersive spectroscopy (EDS) system (Oxford Instruments, UK). The grain sizes and the volume percent of $TiAl_x$ intermetallic impurities in all samples were determined from their BSE micrographs using Image J software.

Table 4-1: Summary of processing conditions, amount and type of impurities, and grain sizes of all samples tested in this study. Note PS denotes pressureless sintering and SPS denotes spark plasma sintering.

Sample	Powder Source	Sintering Technique	Post Heat Treatment	Secondary Phases Detected			Grain Size		
							Diameter	Thickness	AR
			(hr)	XRD	SEM/EDX	Vol % $TiAl_x$	(μm)	(μm)	
CS-CG	Maxthal 211	PS 1500°C 4 hr	0	$TiAl_x$; Ti_3AlC_2; $Ti_5Al_2C_3$	$TiAl_x$; Ti_3AlC_2; $Ti_5Al_2C_3$; Al_2O_3	17	22 ±22	5 ±2.6	4.4
CP- FG	Maxthal 211	SPS 1300°C 15 min	0	$TiAl_x$ Ti_3AlC_2	$TiAl_x$; Ti_3AlC_2; Al_2O_3	7	4.2 ±2.5	2.1 ±1	2.1
RP-FG	RP	SPS 1300°C 45 min	0	-	$TiAl_x$; Al_2O_3	3	6.1 ±2.8	4.6 ±2.2	1.4
RP-MG	RP	SPS 1300°C 45 min	8	-	$TiAl_x$; Al_2O_3	3	13.9 ± 8	7.3 ±2.4	1.9
RP-CG	RP	SPS 1300°C 45 min	24	-	$TiAl_x$; Al_2O_3	3	17.4 ± 9.7	8.2 ±2.9	2.2

In addition, the microstructures of two sample sets, RP-FG and RP-CG in the as-sintered condition and after loading at 20 ^{o}C, 700 ^{o}C and 1100 ^{o}C (see below), were examined by EBSD analysis. Those samples were polished down to 60 nm to provide a smooth finish and secured in pre-tilted 70^{o} specimen holders to provide the high tilt angle required for EBSD. The EBSD maps were collected using a field emission gun SEM (Zeiss Ultra Plus, Carl Zeiss, Oberkochen, Germany) operating with an accelerating voltage of 20kV. An area of 250 μm x 250 μm was scanned for each sample with a step size of 0.2 μm. Data acquisition and analysis were performed using Oxford Instrument's AZTecHKL and HKL Tango and Mambo software.

Room and high temperature uniaxial quasi-static compression tests were performed on cylindrical samples with dimensions of 5 mm in diameter by 8 mm in length cut by wire electron discharge machining (Wire-EDM). The samples were tested in a servo-hydraulic testing machine (MTS-810, MTS, USA) equipped with a vertical split furnace and SiC pushrods. The tests were conducted at a fixed crosshead displacement rate set to yield an initial strain rate of 10^{-4} s^{-1}. A high temperature axial extensometer (632.59E-77, MTS, USA) was attached to SiC spacers while the sample's temperature was monitored with a K-type thermocouple that was placed in direct contact with the said spacers. Heating rates were limited to less than 600 °C hr^{-1} and a soaking time of 15 minutes was used to allow the sample to equilibrate to the testing temperature.

4.4 Results and Discussion

4.4.1 Microstructure of As-Processed Samples

BSE micrographs of as-processed samples with different microstructures like those shown in Figure 4-1 were used to measure the length and thickness of over 100 grains in each sample. The results of the grain size measurements, summarized in Table 4-1, show that the average grain length and thickness varied from 4.2 ±2.5 to 44.7 ±39.2 μm and from 2.1 ±1 to 13.8 ±7.5 μm, respectively in samples fabricated using different processing routes. Similar BSE micrographs of polished but unetched samples, similar to Figure 4-1e, were used together with EDS analysis to determine vol% of $TiAl_x$ as $Vol_{TiAl}\% = \left(\frac{Area_{TiAl}}{Area_{Total}}\right) * 100\%$ in all microstructures. The results are summarized in Table 4-1. Note that $TiAl_x$ was determined to be the major impurity phase in all samples and can be easily distinguished from Ti_2AlC as a dark gray phase in BSE images, as it is denoted by arrows in Figure 4-1e. XRD results (not shown here) are also summarized in Table 4-1, show that all samples prepared from RP were pure, while those prepared from commercial powders contained not only $TiAl_x$, but also Ti_3AlC_2 and $Ti_5Al_2C_3$. Additional phase composition studies of the samples processed from RP using EBSD (not shown here) also confirmed their high purity since less than 3.3 % of Al_2O3, 1.4% of $TiAl_x$, and 0.16% of TiC were detected in all examined samples.

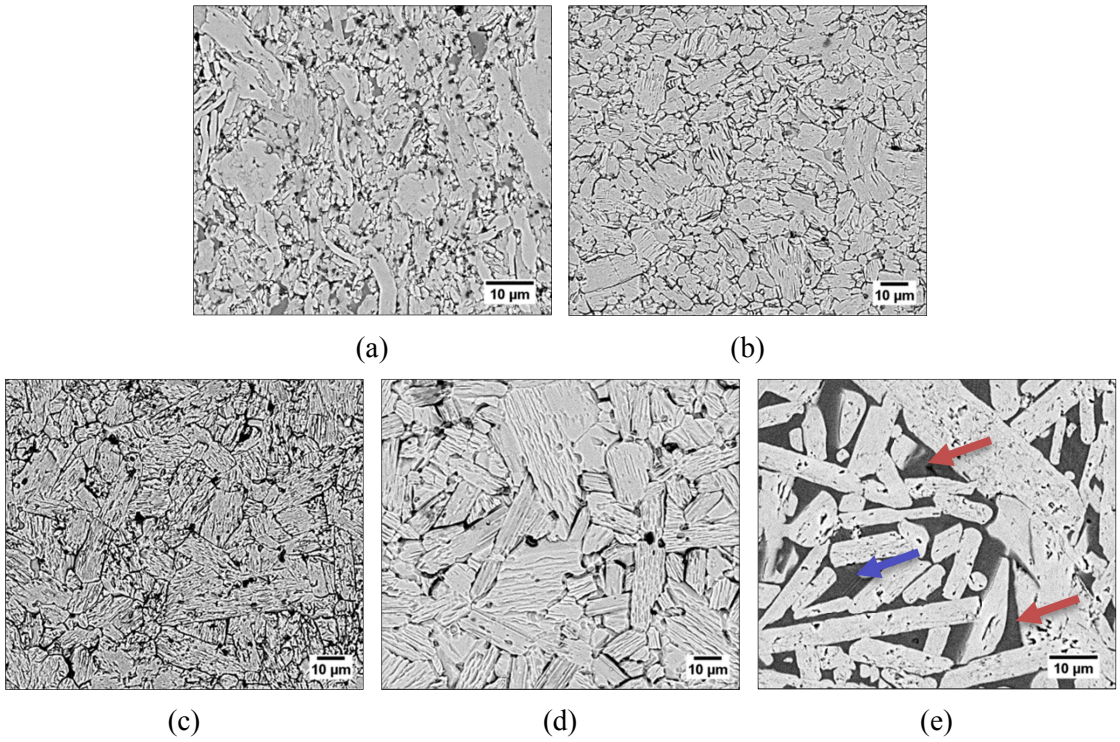

Figure 4-1: Selected but typical backscatter electron micrographs of examined samples: (a) etched CP-FG; (b) etched RP-FG; (c) etched RP-MG; (d) etched RP-CG; and (e) unetched CP-PS where dark gray phase between Ti_2AlC grains denoted by arrows was identified by EDS as $TiAl_x$;

4.4.2 Compressive Testing

Figure 4-2 shows selected but typical stress-strain curves obtained from compression testing at different temperatures. The mechanical response of all the Ti_2AlC samples tested are qualitatively very similar to those previously reported for Ti_2AlC and other MAX phases [5, 26, 39, 47, 123]. Below the BPTT, the fine grained samples exhibit higher compressive strengths. All samples fail in essentially brittle manner with very small amount of softening before failure. At 700 ^{o}C, both the fine and the

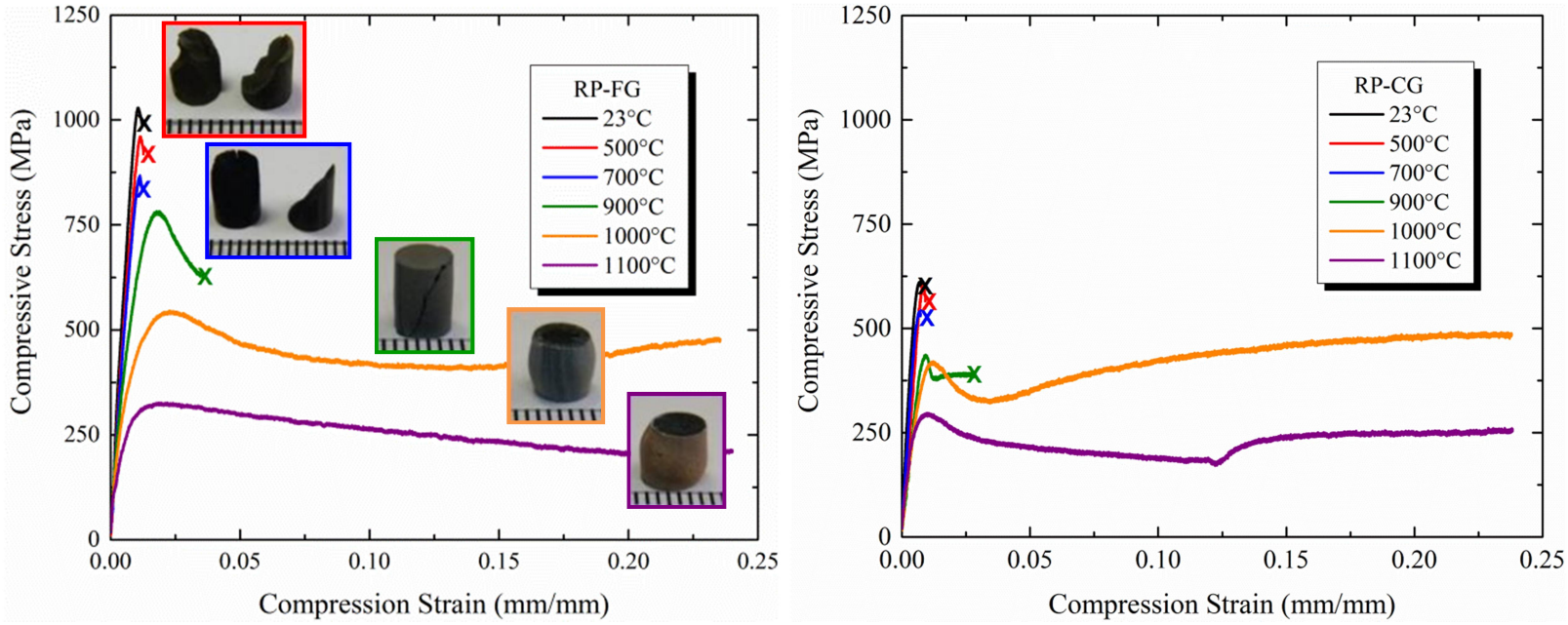

a) b)

Figure 4-2: Selected but typical stress-strain curves obtained from compressive testing of (a) RP-FG and (b) RP-CG samples at different temperatures. Note samples tested at 1000 °C and 1100 °C were interrupted before samples failed.

coarse grained samples show more graceful failure as it is showed with the larger "tail" or softening between maximum and failure stresses. At 1000 ^{o}C and 1100 ^{o}C, all samples are deformed plastically up to ≈23% strains and the differences in compressive strength between the fine and the coarse grained structures seem to diminish. The samples tested above the BPTT did not fail at those large stresses because the tests were interrupted as the measured strains reached the upper limit of extensometer. After reaching a maxima in stress above the BPTT, they show some softening as the stress decreases with increasing strain, after which they show small hardening. The transition point between the softening and the hardening range shift towards higher strains with increasing temperature and decreasing grain size. Since all samples tested above the BPTT exhibited extensive lateral strains and barreling, the interpretation of this transition from softening to hardening requires additional experimental studies before any conclusion about nature of that transition can be drawn.

To further analyze the brittle-to-plastic transition temperature, the average strain to failure was plotted vs. testing temperatures for all in Figure 4-3. The results show that the BPTT lies somewhere between 700 ^{o}C and 1000 ^{o}C is similar to the reported values of 800 ^{o}C – 900 ^{o}C [48]. Note that this temperature seems to depend also on the microstructure as the sample with the finest microstructure (CP-FG) and 7 vol.% of $TiAl_x$ shows a transition at much lower temperatures. The effect microstructures on mechanical response of Ti_2AlC in compression, can be also observed on Figure 4-4a where compressive stresses are plotted vs. testing temperature. Those results show that,

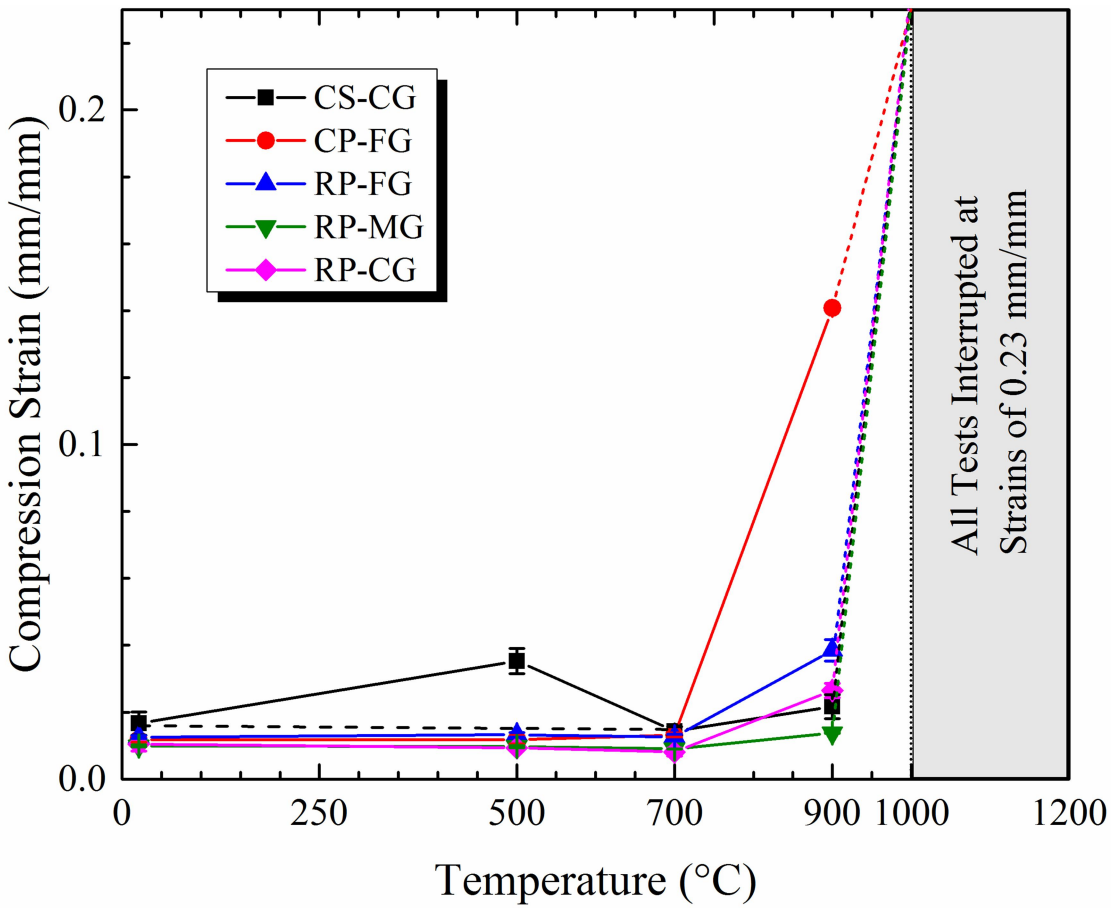

Figure 4-3: Average compression strain as a function of temperature. The maximum strain recorded at and above 1000°C is 0.23 mm/mm for all samples since tests were interrupted. Moreover, the data point at 500°C for CS-CG is suspected outlier from the expected trend observed from all other samples.

similar to Ti_3SiC_2 [26, 45], the compressive strength is quite a strong function of grain size below the BPTT, with the fine grain structures having higher compressive strengths. However, as the testing temperature increases, the compressive strength decreases more rapidly in samples with smaller grain sizes. Above the BPTT, the difference between the average compressive strengths of the samples with different microstructures seem to

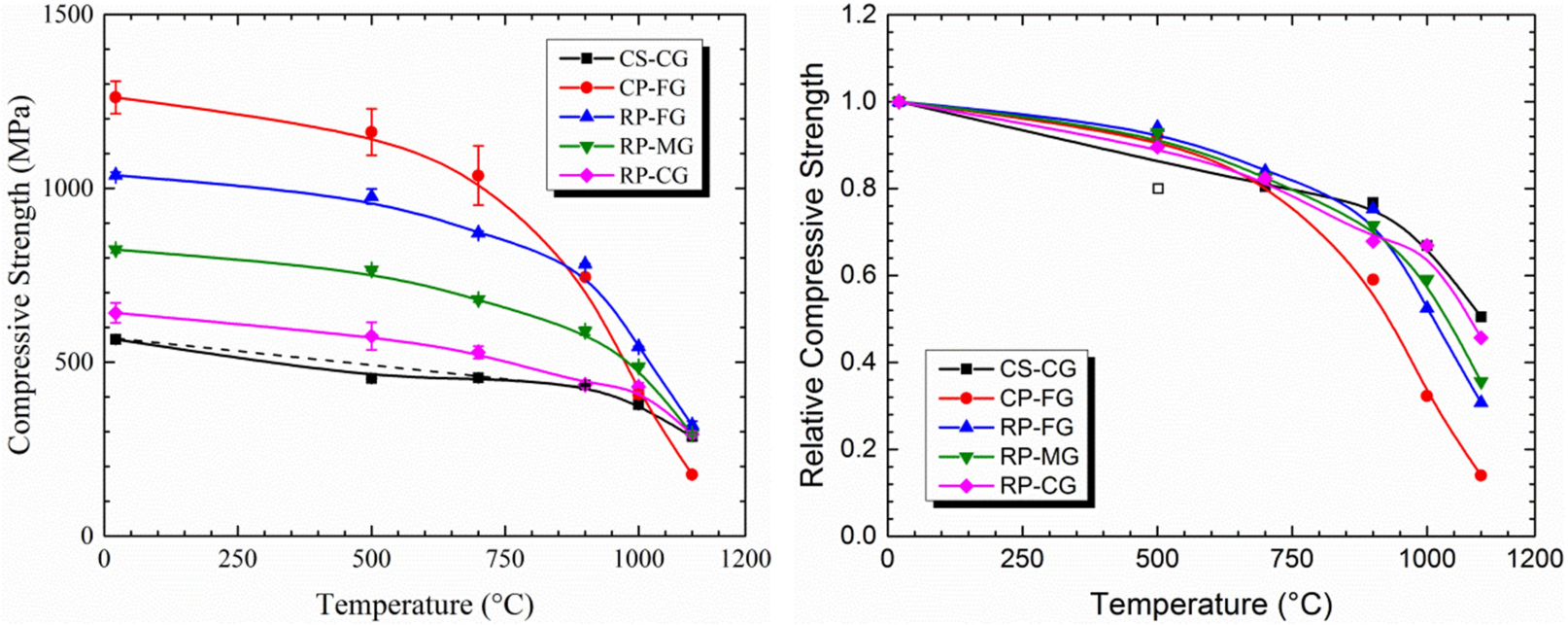

(a) (b)

Figure 4-4: (a) Average compressive strength as function of temperature samples and (b) relative compressive strength as a function of temperature for all samples tested.

diminish. However, as it is shown in Figure 4-4b, the relative compressive strength – defined as the compressive strength at any temperature divided by the compressive strength at room temperature – does not depend on the microstructure below the BPTT, while it drops more steeply with temperature in the samples with finer grain size. At first sight, this observation seems to be in contradiction with results in Figure 4-4a, showing that the compressive strength depends on the grain size much stronger below the BPTT than above it.

However, when the compressive strength is plotted as function of $1/\sqrt{l}$, where l is the grain length, as in Figure 4-5, the underlying reason for trends observed in Figure 4-4 becomes more obvious. Below 900 ^{o}C all samples show a Hall-Petch type relationship between the strength and the grain size. Note that the slopes of the best fit lines in Figure 4-5 seem to be almost identical for the different temperatures below the BPTT. As it was outlined in the previous chapter, the Hall-Patch type relationship between strength and grain length can be associated with the failure caused by dislocation piling up on grain boundaries between soft and hard grains that in turn leads to high stress concentrations and the formation of Zener-Stroh type cracks or Mode II fracture [117]. Since this model predicts that the slope of the Hall-Petch lines depend on the theoretical strength and elastic modulus, it is not surprising that it does not change significantly with increasing temperature. However, around and above the BPTT different trends can be observed, i.e. the slope of the best fitting lines in Figure 4-5 decreases significantly and at 1100 ^{o}C it becomes equal to zero for coarse grained sizes, and even negative (inverse Hall-Petch effect) for fine grained Ti_2AlC.

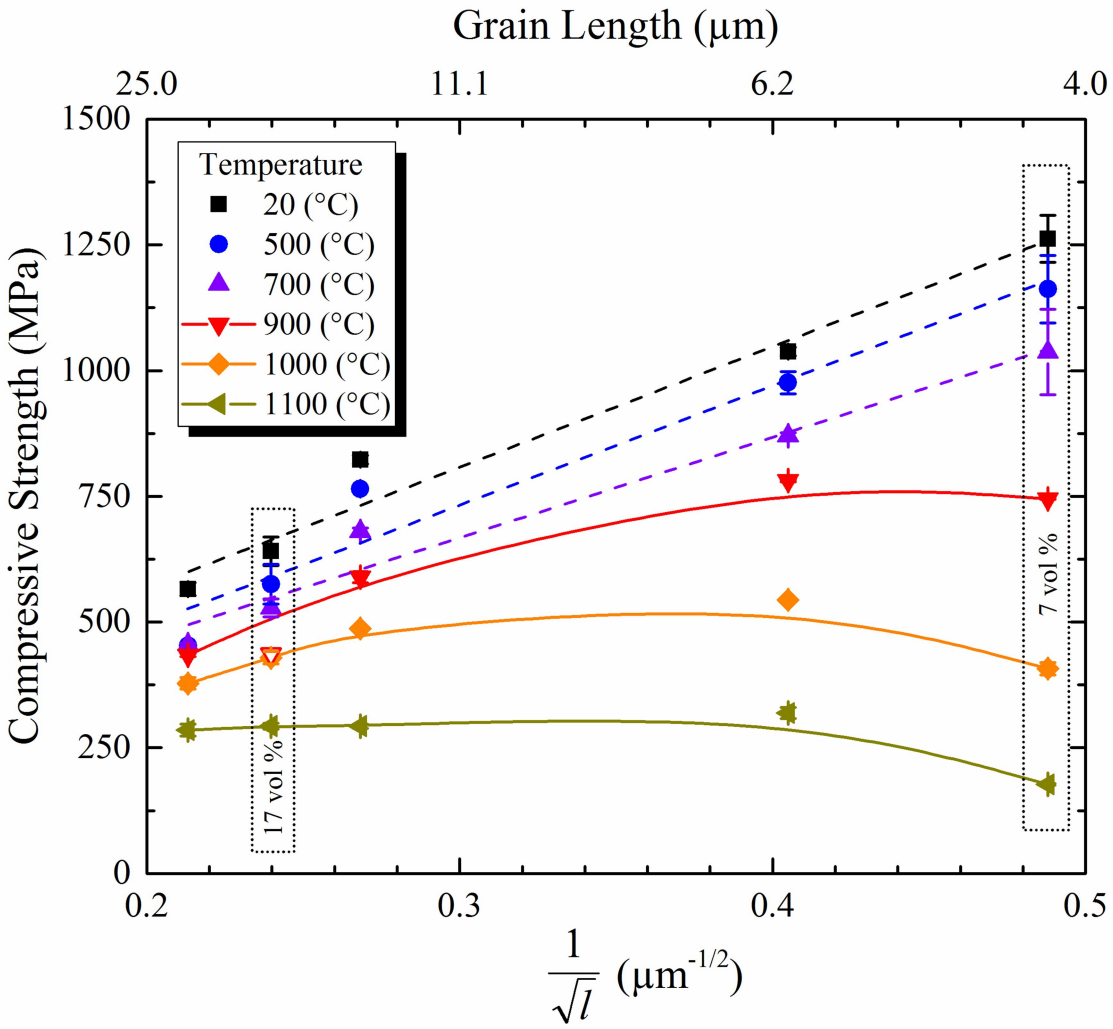

Figure 4-5: Compressive strength plotted in the Hall-Petch manner as a function of $1/\sqrt{l}$. The black, blue, and violet dashed lines are linear regressions, while the solid red, orange and dark yellow are from B-spline connecting data point.

Although more work is needed to fully understand the deviation from the Hall-Petch relationship between the strength and the grain size above the BPTT, it is worth noting here that the $TiAl_x$ impurities does not affect significantly this trend, at least not in coarser microstructures, since the behavior of the sample with the highest amount of $TiAl_x$ of 17 vol.% does not deviate from the observed trends up to 1100 ^{o}C, Figure 4-5.

On the other hand, the larger drop in the compressive strength is also observed in the sample with larger amount of $TiAl_x$ of 7 vol.% but this sample has the smallest grain size.

4.4.3 Electron Back Scattered Diffraction

To study the effects of the microstructure on the BPTT of Ti_2AlC and its evolution during loading at different temperatures, EBSD analysis was performed on RP-FG and RP-CG samples after testing at 700 °C (below the BPTT) and 1100°C, the latter chosen to be above the BPTT and where the peak compressive strengths of the FG and CG samples seem to converge, see Figure 4-4. The results of this exercise are summarized in Figure 4-6 for RP-FG and Figure 4-7 for RP-CG samples. For comparison, some of the previously reported EBSD results for as-processed samples and samples loaded to 500 MPa at room temperature are also shown in Figure 4-6 and Figure 4-7 [100]. Results in the figures are organized into four columns where:

- IPF column shows inverse pole figure maps;
- GBs column shows low angle grain boundaries (LAGB) maps with misorientation angles across boundary ranging from 2^o to 10^o as red lines, together with high angle grain boundaries (HAGB) defined by misorientation exceeding 10^o as black lines;
- BC+UI shows band contrast maps and unindexed area indicating quality of the EBSD results;
- SF+GB shows Schmid factor maps together with LAGB as red lines and HAGB as black lines.

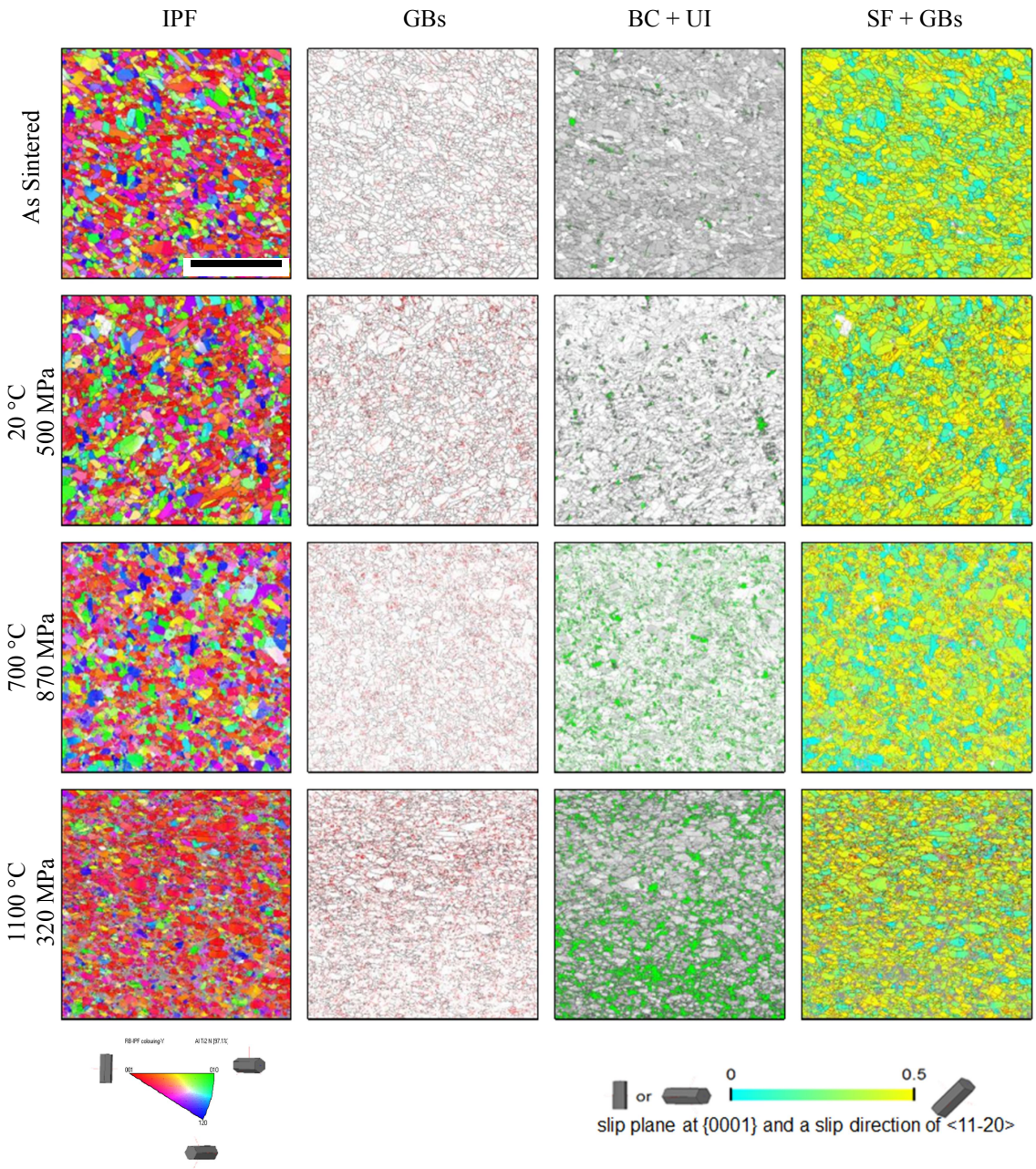

Figure 4-6: EBSD maps for RP-FG sample. Columns from left to right are labeled: (IPF) for Inverse pole figures maps; (GBs) for grain boundary map with black indicating high angle grain boundaries where misorientation exceeds 10° and in red for low angle grain boundaries for those less than 10°; (BC + UI) for band contrast map and unindexed area in green; (SF + GBs) for Schmid factor maps with blue indicating zero and yellow indicating the maximum of 0.5 and with grain boundaries showing with the before mentioned criteria. The rows indicate history of sample and from top to bottom are for as-sintered sample; sample loaded to 500 MPa at 20 °C,; sample loaded to failure at 700 °C that exhibited 870 MPa peak stress; and for sample loaded at 1100°C and exhibited peak stress of 320 MPa but no macroscopic failure.

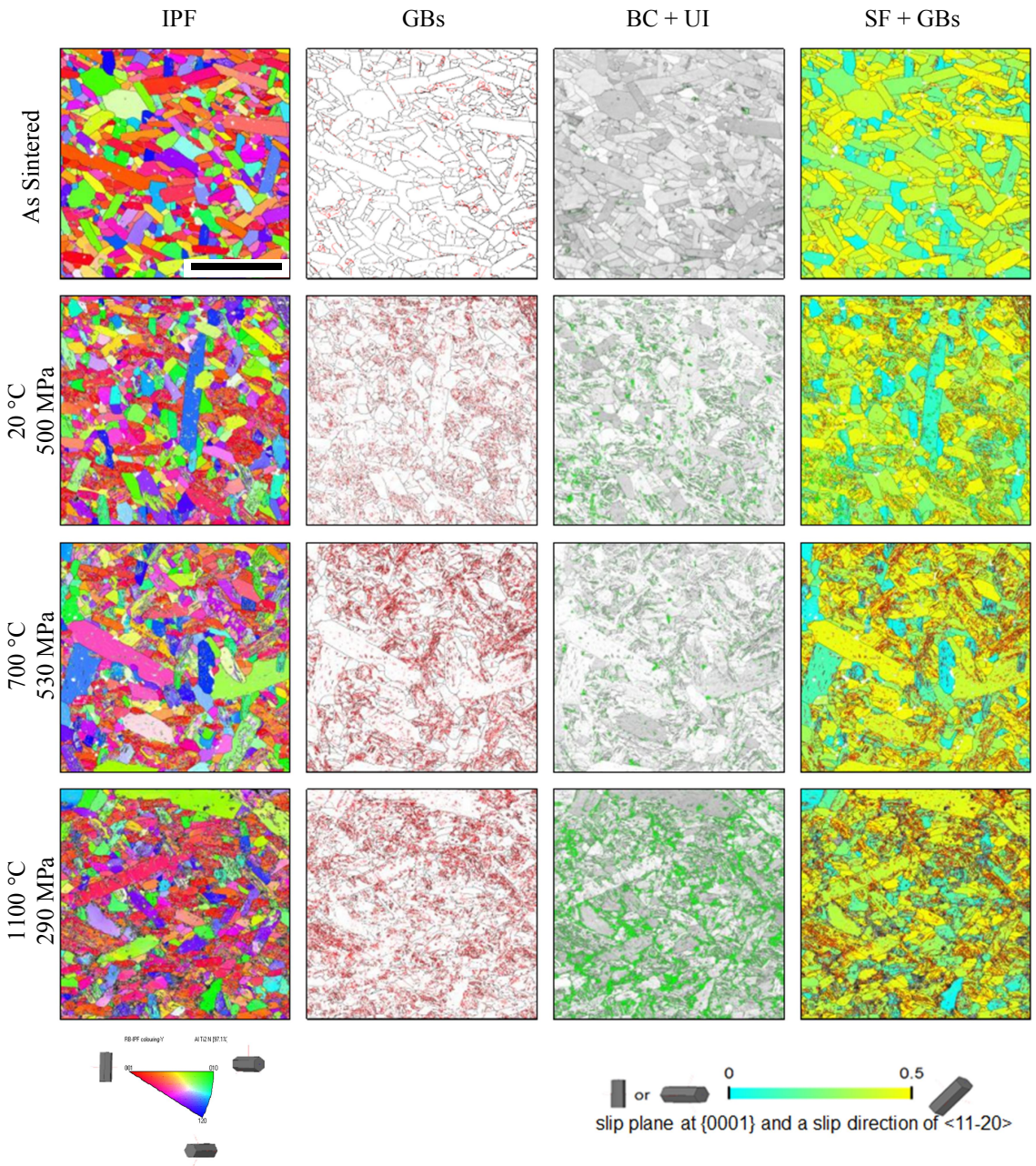

Figure 4-7: EBSD maps for RP-CG sample. Columns from left to right are labeled: (IPF) for Inverse pole figures maps; (GBs) for grain boundary maps with black indicating high angle grain boundaries where misorientation exceeds 10° and in red for low angle grain boundaries for those less than 10°; (BC + UI) for band contrast map and unindexed area in green; (SF + GBs) for Schmid factor map with blue indicating zero and yellow indicating the maximum of 0.5 and with grain boundaries showing with the before mentioned criteria. The rows indicate history of sample and from top to bottom are for as-sintered sample; sample loaded to 500 MPa at 20 °C,; sample loaded to failure at 700 °C that exhibited 530 MPa peak stress; and for sample loaded at 1100°C and exhibited peak stress of 290 MPa but no macroscopic failure.

As it is illustrated in Figure 4-8 and Figure 4-9, and discussed in more details in section 2.4.3 [100], those walls have configurations of close and open loops, or straight lines that span across grains from one grain boundary to another one. The latter indicates that the amount of the plastic deformation in individual grains increases with increasing temperature. Note that a significant amount of grain refinement was observed in some coarse grains (Figure 4-9a) due to the combination of kinking, delamination and formation of DWs. The latter is in good agreement with EBSD and TEM result reported previously on the microstructural evolution in Ti_3SiC_2 during creep [83] that show more complex deformation in CG structure. Similar to what can be seen in Figure 4-6 to Figure 4-9, that study also showed that the deformation in the CG structure is less homogeneous, wherein basal plane slip leads to the formation of numerous KBs combined with delamination, and that the deformation of FG structure is more uniform with very few KBs or DWs located in almost every grain .

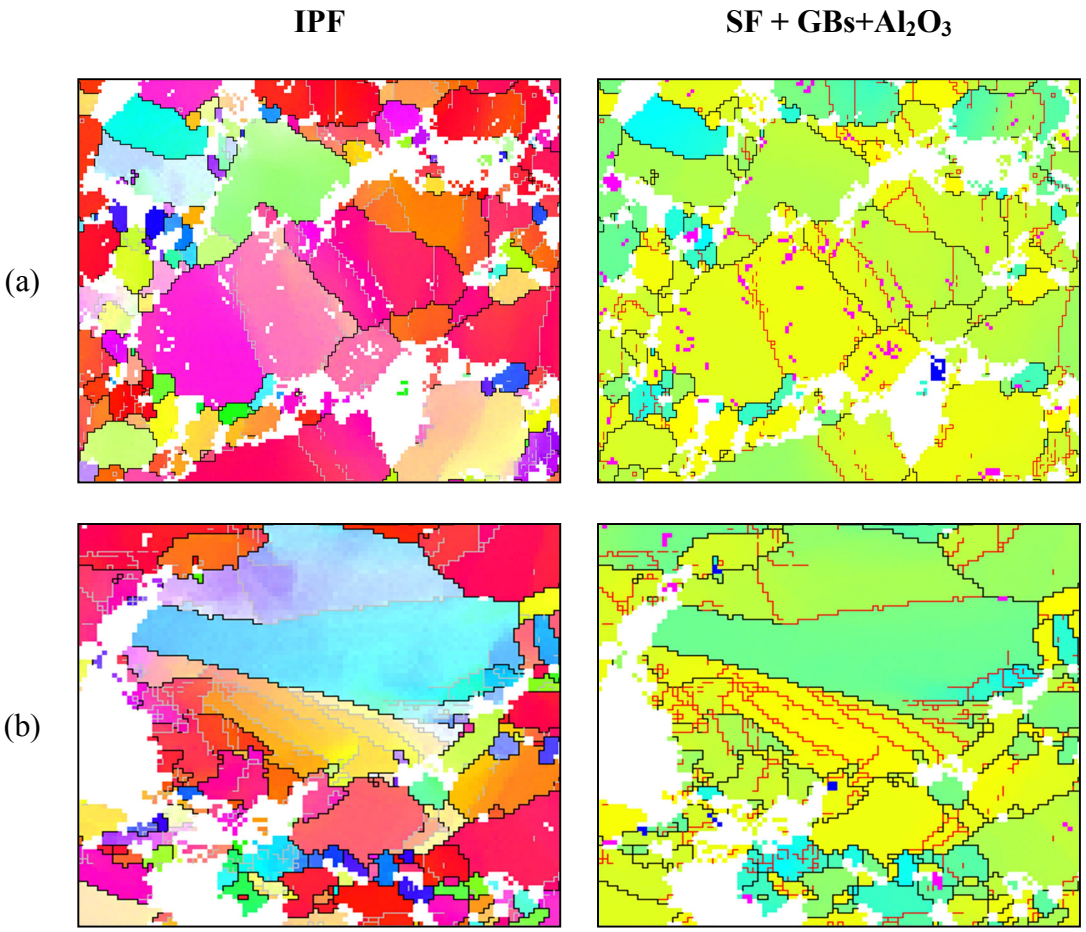

Figure 4-8: Select area from EBSD maps for RP-FG after testing in copression at 1100°C showing (IPF) inverse pole figure maps and (SF + GBs +Al_2O_3) Schmid factors, grain boundaries as in previous figures, and alumina formation in magenta. Note that low Schmid factor grains, aqua and green have little or no LAGBs within, while the high Schmid factor grains have large number of LAGBs with some transitioning to HAGBs resulting in grain refinement.

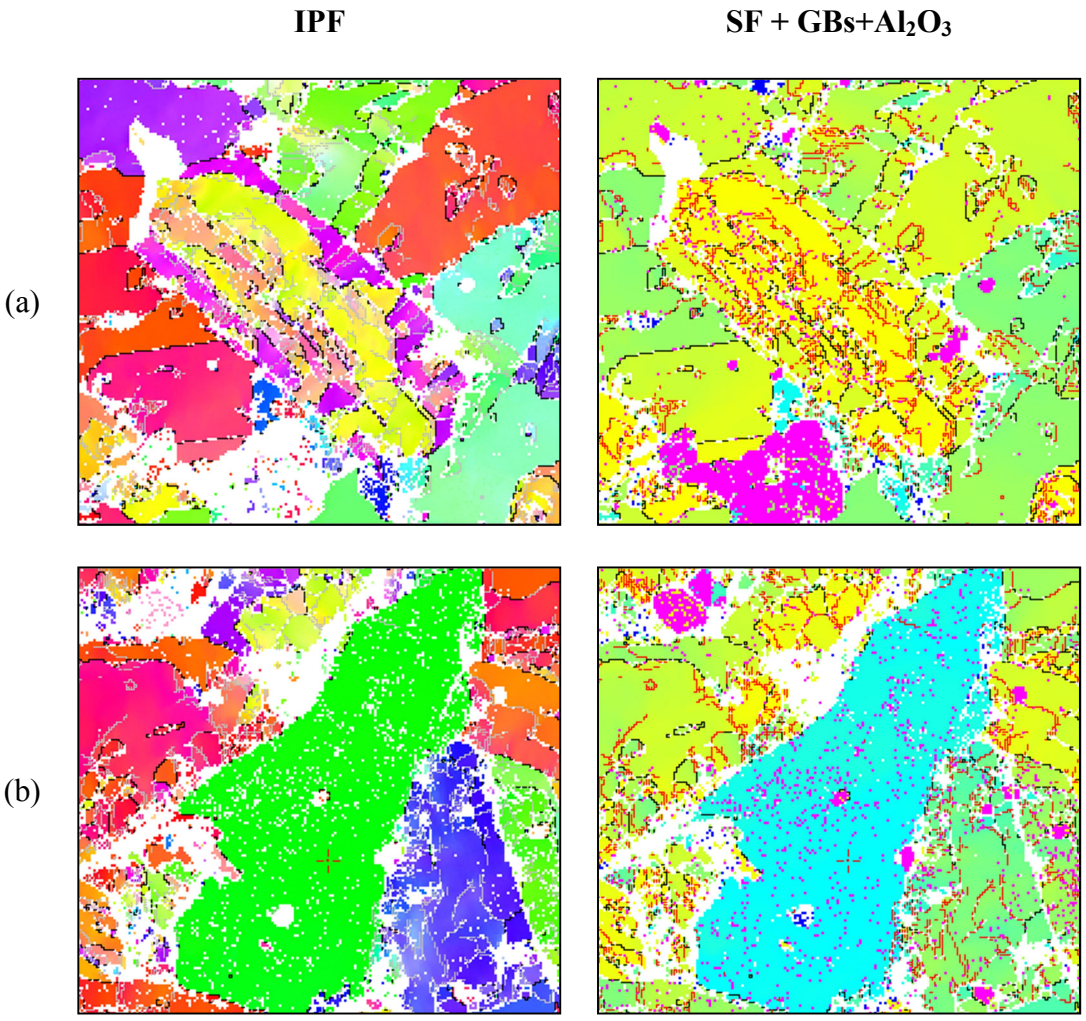

Figure 4-9: Select area from EBSD maps for RP-CG 1100 °C showing (IPF) inverse pole figure maps and (SF + GBs +Al_2O_3) Schmid factor, and grain boundaries as in previous figures and alumina formation in magenta. Note that grain refinement occurs within the grain for grains with high Schmid factors while grains with low Schmid factors appear clean of LAGBs.

In addition, comparison of the results in the BC+UI column (Figure 4-6 and Figure 4-7) shows that fraction of unindexed area, in general, increases with increasing loading temperature. The UI area is a good indication of damages in the form of intergranular pores, microcracks and delamination of examined samples, but it cannot be directly related only to damages as some of the unindexed areas might be result of

heavily deformed microstructure. When compared with previously published results on the damage accumulation observed during thigh temperature loading of Ti_3SiC_2 [26, 41, 46, 120], it is reasonable to conclude that a significant amount of damages initiates around the BPTT. In the FG structure this occurs even below the BPTT. The latter can be accounted to certain extent by the earlier drop in compressive strength observed close to the BPTT in FG structure when compared to CG structure. This can sound contra intuitive because dislocation glide that is limited only to basal planes would lead to larger incompatibility stress in the CG structure and consequently easier damage accumulation, especially intergranular and triple point cracks. However, it has to be taken into account that those stresses can also be relaxed to a greater extent in CG structure, since the formation of KBs in hard grains is easier for the CG structures. Note that the KB formation and associated delamination would cause only moderate softening or drop in strengths as KBs effectively arrest delamination cracks [4].

Additional evidence for this can be found in Figure 4-10 where the number of grains in the 250 x 250 μm^2 area plotted for each sample. Note that the number of grains does not change in the fine grain structure during loading below the BPTT, but it increases significantly above it. However, the number of grains increases much more dramatically in the CG structure than in the FG, even below the BPTT. The latter is associated with easier formation of KBs and corresponding delamination as it was previously discussed in [100]. Above the BPTT, easier slip promotes grain refinement by KB formation, but much more pronounced in the CG structure than in the FG.

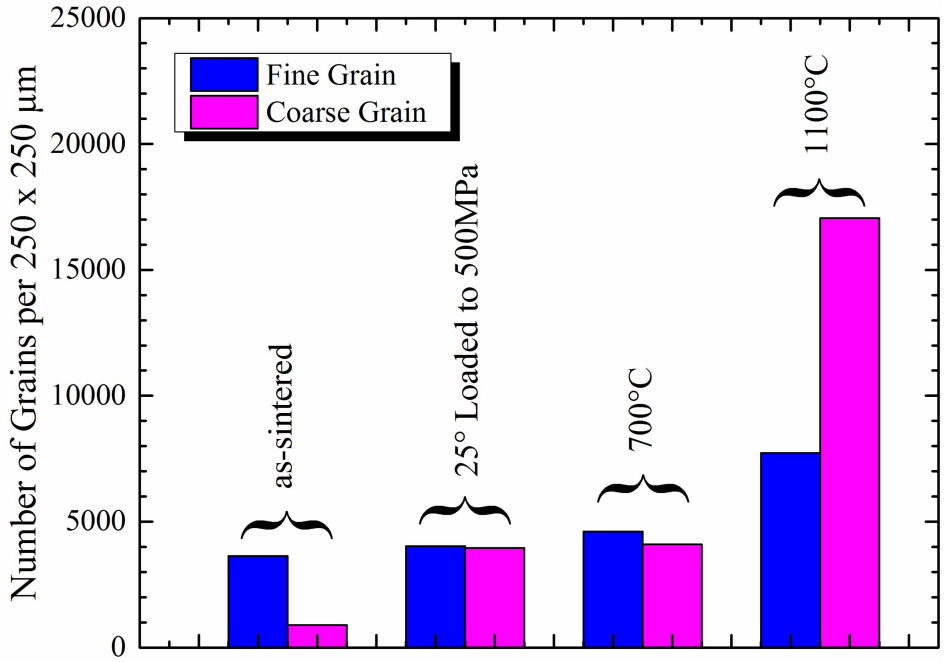

Figure 4-10: The number of grains per 250 µm by 250 µm scanned are computed by EBSD for fine grain in blue and coarse grain in magenta.

Last but not least, IPFs maps in Figure 4-6 and Figure 4-7 suggest a strong development of texture in the FG structure above the BPTT. The latter is seen even better on contoured pole figures in Figure 4-11. The pole figures clearly show no significant texture development in the CG structure, while the FG structure is highly textured after loading above the BPTT with more grains oriented for easy slip. This observation is in good agreement with the greater softening observed in the FG microstructure above the BPTT.

Figure 4-11: Contoured pole figures with fixed multiples of uniform density (MUD) value of 5 for RP-FG samples (left) and RP-CG (right) for samples, from top to bottom, in as-sintered condition; loaded to 500 MPa at 20 °C; loaded to failure at 700 °C and loaded at 1100°C without macroscopic failure.

RP-FG

RP-CG

As Sintered

20 °C – 500 MPa

700 °C

1100 °C

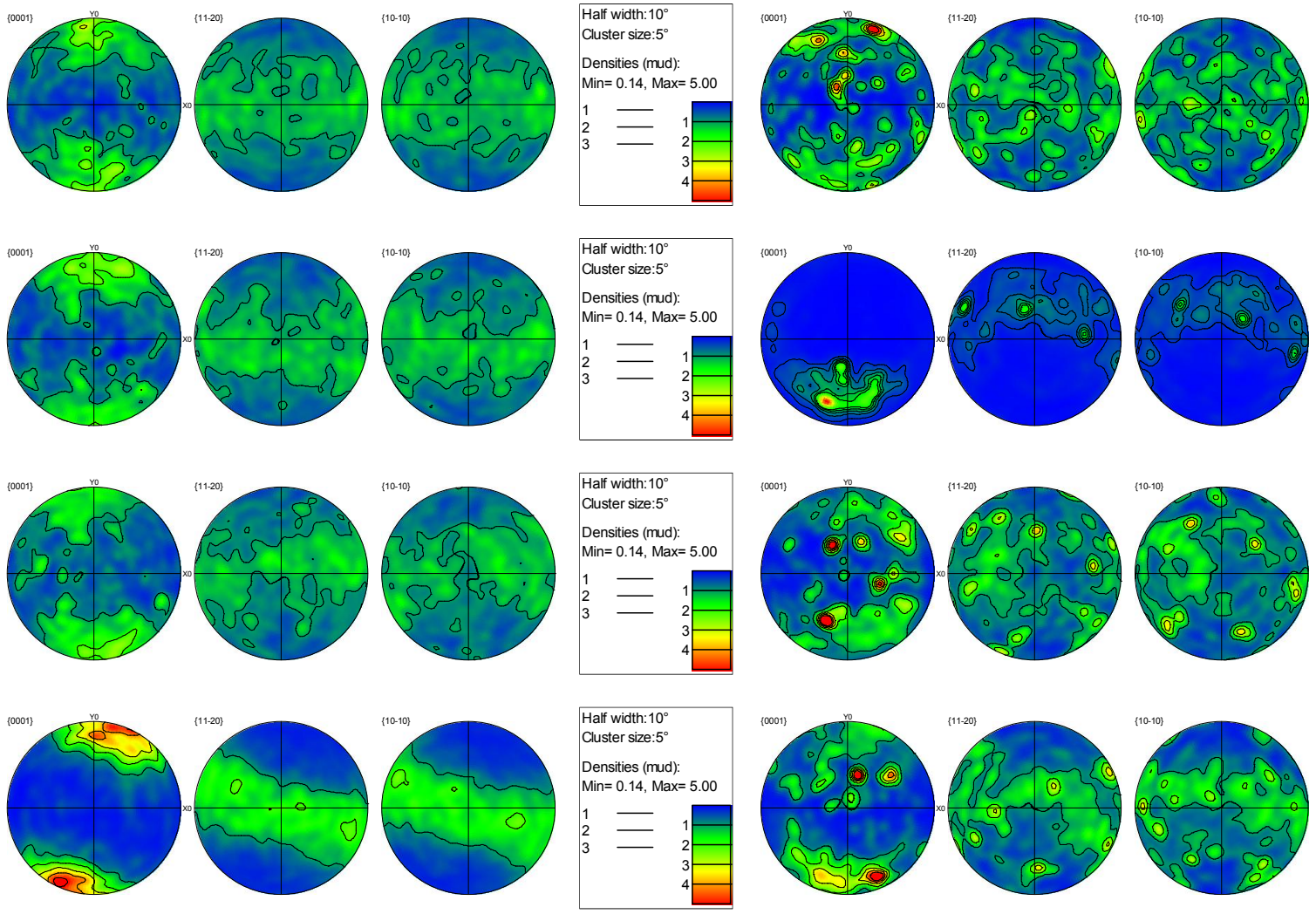

4.5 Summary & Conclusions

Results from high temperature experiments on FG and CG Ti_2AlC show that the BPTT temperature is heavily dependent on grain size. Below the BPTT, the compressive strength decreases monotonically with increasing grain size in a Hall-Petch manner. However, above the BPTT, the relationship between stress and grain size is more complex and deviates from the Hall-Petch relationship; even leading to even inverse Hall-Petch effect for finest grain sizes.

EBSD results demonstrate a complex development of microstructure in both FG and CG sized samples during loading at different temperatures. In the FG microstructures loaded below the BPTT no significant grain refinement was observed while the amount of accumulated damage increases more monotonically with increasing temperature. Above the BPTT, the grain refinement and texture development becomes more pronounced as more grains reorient for the easy slip orientation. At all testing conditions, the deformation in the FG structure is more uniform with very few KBs in almost every grain. However, in the CG structure, a significant grain refinement was observed after loading even below the BPTT as a result of highly inhomogeneous deformations of some of the grains, with the grain refinement becoming even more dramatic above the BPTT. In addition, no significant texture development was observed in the CG structure.

When the results presented are combined with the fact that the plastic deformation of MAX phases is highly anisotropic, since critical resolves shear stress for dislocation glide in basal planes is very low and that the other deformation mechanisms

available in MAX phases, i.e. kinking and KB formation are much easier in CG structure, the following can be concluded about the underling mechanism for the BPTT. During loading of the CG structure, huge incompatibility stresses develop as basal plane dislocation glide is less hindered by grain boundaries. However, since the CG microstructure can deform easier by KB formation, those stresses can be also relaxed much easier in CG structure. As a result, significant grain refinement occurs in CG structure due to KB formation associated KB delamination, even below the BPTT. As a result, the CG structure has a low strength below the BPTT. However, since KBs effectively arrest delamination cracks, they do not propagate immediately, but rather accumulate with increasing load and thus CG structures fail more in pseudoductile manner. Because of basal plane slip and KB formation becomes gradually easier with increasing temperature, the above described scenario will result approximately only on a monotonic decrease of strength.

However, although the magnitude of incompatibility stresses that develop in the FG samples as a result easy basal plane slip is rather smaller than in CG structure, the FG can hardly relax by KB formation as kinking of FG with low aspect ratio is more difficult. The latter results in the more uniform deformation observed in the FG structure and no significant grain refinement due to the formation of KB below the BPTT. Thus as the incompatibility stresses are smaller in the FG structure, once they reach a critical magnitude they cannot be easily relaxed by activation of kinking; instead, intergranular cracks of the Zener-Stroh type form. Since those cracks are not effectively blocked by KBs, like in the case of CG structure, the strength of the samples, although initial very

high, start to decrease dramatically even at lower temperatures than in the CG structure, as CRSS in soft grains drops down. At and above the BPTT, the formation of intergranular cracks together with easier grain boundary sliding results in grain reorientation that favors easier dislocation slip in basal planes and therefore a more significant drop in strength when compared to CG structure. The reorientation of grains for easier slip also makes formation of KBs much easier leading to some refinement of the microstructure. Note that although the grain size decreases more rapidly in CG structure than in the FG, due to easier KB formation and associated delamination in CG, this will not promote grain boundary sliding as in the case of FG structure. The grain boundaries formed as a result of kinking are quite immobile, when compared to the original grain boundaries. The latter also suggest that more systematic studies on grain boundary chemistry and structure has to be done to further understand the effects of microstructure on the high temperature mechanical behavior of MAX phases and the nature of the BPTT.

5 SUMMARY

This study investigated the effects of microstructure, mainly grain size and $TiAl_x$ impurities on the mechanical properties of Ti_2AlC. Key findings are summarized below.

Section 2 reports on the results from room temperature cyclic compression testing of Ti_2AlC in combination with resonant ultrasound spectroscopy and electron backscatter diffraction. It was shown that neither of proposed single-mechanistic models currently found in literature, namely Kinking Non-Linear Elastic, Microcracking and Reversible Flow model can be single-handedly implemented to describe the complex mechanical behavior of MAX phases over the entire range of stresses. Instead the mechanical response of both fine (FG) and course (CG) grain Ti_2AlC can be divided into four different stress regions (Region I – IV) with substantially different underlining deformation mechanisms:

- **Region I** is characterized completely by linear elastic behavior;
- **Region II** displays a small amount of energy dissipation per cycle that can be attributed to the development of complex incompatibility stresses as a result of elastic/plastic anisotropy, and the reversible glide of basal plane dislocations, similar to the RF model[37].
- **Region III** has higher energy dissipated per loading cycle than Region II. EBSD results show a large number of dislocation walls (DWs) in straight, curved, and looped configurations that also result in cyclic hardening. The reversible movement

(or bowing) of LAGBs --- related to those proposed by KNE model [28, 61, 62]--- was proposed as the major energy dissipation mechanism in this region.

- **Region IV** shows a drop in elastic modulus assumed to be due to damage accumulation, in the form of microcracks. The friction of the microcracks' surfaces ,as in [36], contributes to the energy dissipated in each loading cycle, in addition to other above mentioned mechanisms.

In addition, EBSD results of Section 1 provide the first experimental evidence of IKB-like features and proof that the microstructure evolves during loading showing that the formation of low angle grain boundaries as the origin of the hardening observed.

The results presented in Section 3 show the Ti_2AlC fine grain structures fabricated in this study exhibit the highest strength reported to date for Ti_2AlC. In addition, the room temperature cohesive strength scales with $l^{-1/2}$, where l is grain length, obeying a Hall-Petch type relationship. No correlation with the grain thickness was observed. Moreover, $TiAl_x$ impurity contents of up to 18 vol %, do not affect the compressive strength but enhance the amount of strain to failure, especially on coarse grain structures with well dispersed $TiAl_x$. Also the transition stresses between stress regions, as identified in Section 2 --- also referred to as microyielding stresses --- were found to be a strongly dependent on grain size. The magnitude of micro-yielding stress $\sigma_{I\text{-}II}$, dividing Region I, with linear elastic behavior, from Region II, with hysteretic stress strain behavior, mark the onset of basal plane dislocation glide in soft grains and was found to depend on the grain length following a classical Hall-Patch relationship. Micro-yielding stress $\sigma_{II\text{-}III}$, dividing stress Regions II and III with greatly different

hysteretic behaviors shows linear increase with $t^{-1/2}$, where t is average thickness of the grains and a good agreement between experimentally determined $\sigma_{II\text{-}III}$ with grain size predictions of KNE model was observed. The highest transition stress $\sigma_{III\text{-}IV}$, varies with grain length and is in agreement with models based on formation of Zener-Stroh cracks further suggesting that $\sigma_{III\text{-}IV}$ is stress at which microcracking initiates. Finally the critical resolve shear stress of ≈8 to 10 MPa was determined from Hall-Perch type relationships of $\sigma_{II\text{-}III}$ and $\sigma_{III\text{-}IV}$ on the grain length.

In section 4, high temperature quasi-static compression testing show that the compressive strength of the fine grain structures degrades more than the coarse grain structures, regardless of the presence of $TiAl_x$ impurities. Below the BPTT, the compressive strength decreases monotonically with increasing grain size in a Hall-Petch manner. However, above the BPTT, the relationship between stress and grain size is more complex and deviates from Hall-Petch relationship; even leading to an inverse Hall-Petch effect for the finest grain sizes. Post-mortem EBSD analysis shows no grain refinement in fine grain microstructures below the BPTT and that damage accumulation increases with testing temperature. Above the BPTT, grain refinement and grain reorientation for easy basal slip occurs in the fine grain structure. As opposed to coarse grain, the fine grain structures show more uniform deformation with few KBs or DWs in each grain. The coarse grain samples show inhomogeneous deformation with grain refinement concentrated heavily on few grains and no significant texture evolution above the BPTT. It is concluded that the coarse grain structures can more easily relax incompatibility stresses through KB formation and the associated delamination, even

below the BPTT. This, in addition to the fact that KB are delamination crack arresting features, is responsible for the lower strengths and pseudoductile behavior of coarse grain below the BPTT and their near monotonic decrease in strength with temperature.

In light of the new understanding of MAX phase behavior the following recommendations on future studies are suggested to further increase the understanding of these materials and/or expand and accelerate their real world applications.

- All the mechanical testing in this study was performed under compression loading but the behavior under tension and other loading modes remained to be studied; The applicability of the concepts presented in this study, such as the microyielding stresses, to other modes of deformation should be investigated.
- Explore a wider range of sintering aids, in addition to $TiAl_x$, to allow Ti_2AlC to be processed more economically and without the need for specialized equipment like, spark plasma sintering or hot isostatic presses.
- Explore the idea of using $TiAl_x$ or similar materials for welding of Ti_2AlC as the ability to repair components in the field rather than replacement would increase their use in industry.
- Further development MAX phase – Metallic composites to tailor their density, energy dissipation, and failure strains is encouraged to expand potential applications.
- Interrupted high temperature tests in combination with EBSD to further understand the texture evolution of Ti_2AlC, especially in fine grain microstructures is proposed.

- Meticulous TEM work to investigate the existence of grain boundary impurities and their contribution to the BPTT.
- Since alumina forms on Ti_2AlC, careful elemental analysis before and after high temperature deformation to investigate if aluminum is leaching out and its potential contribution as lubricant for grain boundary sliding at the BPTT and above.

REFERENCES

[1] M.W. Barsoum, T. El-Raghy. Synthesis and characterization of a remarkable ceramic: Ti3SiC2, Journal of the American Ceramic Society 79 (1996) 1953-1956.

[2] M. Radovic, M.W. Barsoum. MAX phases: Bridging the gap between metals and ceramics, American Ceramic Society Bulletin 92 (2013) 20-27.

[3] M.W. Barsoum. MAX phases : properties of machinable ternary carbides and nitrides, Weinheim, Germany : Wiley-VCH Verlag GmbH & Co. KGaA, 2013.

[4] M.W. Barsoum, M. Radovic. Elastic and mechanical properties of the MAX phases. Annual Review of Materials Research, vol. 41, 2011. p.195-227.

[5] M.W. Barsoum, M. Ali, T. El-Raghy. Processing and characterization of Ti2AlC, Ti2AlN, and Ti2AlC0.5N0.5, Metallurgical and Materials Transactions A: Physical Metallurgy and Materials Science 31 (2000) 1857-1865.

[6] F.L. Meng, Y.C. Zhou, J.Y. Wang. Strengthening of Ti2AlC by substituting Ti with V, Scripta Materialia 53 (2005) 1369-1372.

[7] D.J. Tallman, M. Naguib, B. Anasori, M.W. Barsoum. Tensile creep of Ti 2AlC in air in the temperature range 1000-1150°C, Scripta Materialia 66 (2012) 805-808.

[8] S. Basu, N. Obando, A. Gowdy, I. Karaman, M. Radovic. Long-term oxidation of Ti 2AlC in air and water vapor at 1000-1300°C temperature range, Journal of the Electrochemical Society 159 (2012) C90-C96.

[9] X.H. Wang, Y.C. Zhou. High-temperature oxidation behavior of Ti2AlC in air, Oxidation of Metals 59 (2003) 303-320.

[10] J.W. Byeon, J. Liu, M. Hopkins, W. Fischer, N. Garimella, K.B. Park, M.P. Brady, M. Radovic, T. El-Raghy, Y.H. Sohn. Microstructure and residual stress of alumina scale formed on Ti 2AlC at high temperature in air, Oxidation of Metals 68 (2007) 97-111.

[11] H.J. Yang, Y.T. Pei, J.C. Rao, J.T.M. De Hosson, S.B. Li, G.M. Song. High temperature healing of Ti2AlC: On the origin of inhomogeneous oxide scale, Scripta Materialia 65 (2011) 135-138.

[12] D.J. Tallman, B. Anasori, M.W. Barsoum. A Critical Review of the Oxidation of Ti2AlC, Ti3AlC2 and Cr2AlC in Air, Materials Research Letters 1 (2013) 115-125.

[13] J.L. Smialek, A. Garg. Microstructure and Oxidation of a MAX Phase/Superalloy Hybrid Interface. NASA/TM—2014-216679, Cleveland, 2014.

[14] M.W. Barsoum, L. Farber, T. El-Raghy. Dislocations, kink bands, and room-temperature plasticity of Ti3SiC2, Metallurgical and Materials Transactions A: Physical Metallurgy and Materials Science 30 (1999) 1727-1738.

[15] E. Orowan. A type of plastic deformation new in metals, Nature 149 (1942) 643-644.

[16] F.C. Frank, A.N. Stroh. On the theory of kinking, Proceedings of the Physical Society. Section B 65 (1952) 811-821.

[17] M.W. Barsoum, D. Brodkin, T. El-Raghy. Layered machinable ceramics for high temperature applications, Scripta Materialia 36 (1997) 535-541.

[18] T. El-Raghy, A. Zavaliangos, M.W. Barsoum, S.R. Kalidindi. Damage mechanisms around hardness indentations in Ti3SiC2, Journal of the American Ceramic Society 80 (1997) 513-516.

[19] L. Farber, I. Levin, M.W. Barsoum. High-resolution transmission electron microscopy study of a low-angle boundary in plastically deformed Ti3SiC2, Philosophical Magazine Letters 79 (1999) 163-170.

[20] M.W. Barsoum, T. El-Raghy. Room-temperature, ductile carbides, Metallurgical and Materials Transactions A: Physical Metallurgy and Materials Science 30 (1999) 363-369.

[21] A. Guitton, S. Van Petegem, C. Tromas, A. Joulain, H. Van Swygenhoven, L. Thilly. Effect of microstructure anisotropy on the deformation of MAX polycrystals studied by in-situ compression combined with neutron diffraction, Applied Physics Letters 104 (2014).

[22] I. Salama, T. El-Raghy, M.W. Barsoum. Synthesis and mechanical properties of Nb2AlC and (Ti,Nb)2AlC, Journal of Alloys and Compounds 347 (2002) 271-278.

[23] N.I. Medvedeva, A.N. Enyashin, A.L. Ivanovskii. Modeling of the electronic structure, chemical bonding, and properties of ternary silicon carbide Ti3SiC2, Journal of Structural Chemistry 52 (2011) 785-802.

[24] E.N. Hoffman, D.W. Vinson, R.L. Sindelar, D.J. Tallman, G. Kohse, M.W. Barsoum. MAX phase carbides and nitrides: Properties for future nuclear power plant in-core applications and neutron transmutation analysis, Nuclear Engineering and Design 244 (2012) 17-24.

[25] D.J. Tallman, E.N. Hoffman, E.N. Caspi, B.L. Garcia-Diaz, G. Kohse, R.L. Sindelar, M.W. Barsoum. Effect of neutron irradiation on select MAX phases, Acta Materialia 85 (2015) 132-143.

[26] M. Radovic, M.W. Barsoum, T. El-Raghy, S.M. Wiederhorn, W.E. Luecke. Effect of temperature, strain rate and grain size on the mechanical response of Ti3SiC2 in tension, Acta Materialia 50 (2002) 1297-1306.

[27] M.W. Barsoum, T. Zhen, S.R. Kalidindi, M. Radovic, A. Murugaiah. Fully reversible, dislocation-based compressive deformation of Ti 3SiC2 to 1 GPa, Nature Materials 2 (2003) 107-111.

[28] A.G. Zhou, M.W. Barsoum. Kinking nonlinear elastic deformation of Ti3AlC2, Ti2AlC, Ti3Al(C0.5,N0.5)2 and Ti2Al(C0.5,N0.5), Journal of Alloys and Compounds 498 (2010) 62-70.

[29] G.P. Bei, G. Laplanche, V. Gauthier-Brunet, J. Bonneville, S. Dubois. Compressive behavior of Ti3AlC2 and Ti 3Al0.8Sn0.2C2 MAX phases at room temperature, Journal of the American Ceramic Society 96 (2013) 567-576.

[30] M. Radovic, M.W. Barsoum, A. Ganguly, T. Zhen, P. Finkel, S.R. Kalidindi, E. Lara-Curzio. On the elastic properties and mechanical damping of Ti3SiC2, Ti3GeC2, Ti3Si0.5Al0.5C2 and Ti2AlC in the 300-1573 K temperature range, Acta Materialia 54 (2006) 2757-2767.

[31] M. Fraczkiewicz, A.G. Zhou, M.W. Barsoum. Mechanical damping in porous Ti3SiC2, Acta Materialia 54 (2006) 5261-5270.

[32] A.G. Zhou, S. Basu, M.W. Barsoum. Kinking nonlinear elasticity, damping and microyielding of hexagonal close-packed metals, Acta Materialia 56 (2008) 60-67.

[33] S. Amini, M.W. Barsoum. On the effect of texture on the mechanical and damping properties of nanocrystalline Mg-matrix composites reinforced with MAX phases, Materials Science and Engineering A 527 (2010) 3707-3718.

[34] B. Anasori, S. Amini, V. Presser, M.W. Barsoum. Nanocrystalline Mg-matrix composites with ultrahigh damping properties, Magnesium Technology (2011) 463-468.

[35] A.D. Kothalkar, R. Benitez, L. Hu, M. Radovic, I. Karaman. Thermo-mechanical Response and Damping Behavior of Shape Memory Alloy-MAX Phase Composites, Metallurgical and Materials Transactions A: Physical Metallurgy and Materials Science (2014) 1-13.

[36] B. Poon, L. Ponson, J. Zhao, G. Ravichandran. Damage accumulation and hysteretic behavior of MAX phase materials, Journal of the Mechanics and Physics of Solids 59 (2011) 2238-2257.

[37] N.G. Jones, C. Humphrey, L.D. Connor, O. Wilhelmsson, L. Hultman, H.J. Stone, F. Giuliani, W.J. Clegg. On the relevance of kinking to reversible hysteresis in MAX phases, Acta Materialia 69 (2014) 149-161.

[38] X. Tong, T. Okano, T. Iseki, T. Yano. Synthesis and high temperature mechanical properties of Ti3SiC2/SiC composite, Journal of Materials Science 30 (1995) 3087-3090.

[39] T. El-Raghy, M.W. Barsoum, A. Zavaliangos, S.R. Kalidindi. Processing and mechanical properties of Ti3SiC2: II, Effect of grain size and deformation temperature, Journal of the American Ceramic Society 82 (1999) 2855-2860.

[40] M. Radovic, M.W. Barsoum, T. El-Raghy, J. Seidensticker, S. Wiederhorn. Tensile properties of Ti3SiC2 in the 25-1300°C temperature range, Acta Materialia 48 (2000) 453-459.

[41] M. Radovic, M.W. Barsoum, T. El-Raghy, S. Wiederhorn. Tensile creep of fine grained (3-5 μm) Ti3SiC2 in the 1000-1200°C temperature range, Acta Materialia 49 (2001) 4103-4112.

[42] J.F. Li, W. Pan, F. Sato, R. Watanabe. Mechanical properties of polycrystalline Ti3SiC2 at ambient and elevated temperatures, Acta Materialia 49 (2001) 937-945.

[43] D. Chen, K. Shirato, M.W. Barsoum, T. El-Raghy, R.O. Ritchie. Cyclic Fatigue-Crack Growth and Fracture Properties in Ti3SiC2 Ceramics at Elevated Temperatures, Journal of the American Ceramic Society 84 (2001) 2914-2920.

[44] Z.M. Sun, Z.F. Zhang, H. Hashimoto, T. Abe. Ternary compound Ti3SiC2: Part II. Deformation and fracture behavior at different temperatures, Materials Transactions 43 (2002) 432-435.

[45] T. Zhen, M.W. Barsoum, S.R. Kalidindi. Effects of temperature, strain rate and grain size on the compressive properties of Ti3SiC2, Acta Materialia 53 (2005) 4163-4171.

[46] T. Zhen, M.W. Barsoum, S.R. Kalidindi, M. Radovic, Z.M. Sun, T. El-Raghy. Compressive creep of fine and coarse-grained T3SiC2 in air in the 1100-1300 °c temperature range, Acta Materialia 53 (2005) 4963-4973.

[47] D.T. Wan, F.L. Meng, Y.C. Zhou, Y.W. Bao, J.X. Chen. Effect of grain size, notch width, and testing temperature on the fracture toughness of Ti3Si(Al)C2 and Ti3AlC2 using the chevron-notched beam (CNB) method, Journal of the European Ceramic Society 28 (2008) 663-669.

[48] Y. Bai, X. He, R. Wang, Y. Sun, C. Zhu, S. Wang, G. Chen. High temperature physical and mechanical properties of large-scale Ti2AlC bulk synthesized by self-propagating high temperature combustion synthesis with pseudo hot isostatic pressing, Journal of the European Ceramic Society 33 (2013) 2435-2445.

[49] A. Guitton, A. Joulain, L. Thilly, C. Tromas. Evidence of dislocation cross-slip in MAX phase deformed at high temperature, Sci. Rep. 4 (2014).

[50] S. Li, G. Song, K. Kwakernaak, S. van der Zwaag, W.G. Sloof. Multiple crack healing of a Ti 2AlC ceramic, Journal of the European Ceramic Society 32 (2012) 1813-1820.

[51] B.J. Pedimonte, G. Bei, D. Pourjafar, T. Fey, P. Greil. Oxidative crack healing in Al2O3 composites loaded with Ti2AC (A = Al, Sn) repair fillers, Journal of Ceramic Science and Technology 5 (2014) 63-68.

[52] A.S. Farle, C. Kwakernaak, S. van der Zwaag, W.G. Sloof. A conceptual study into the potential of Mn+1AXn-phase ceramics for self-healing of crack damage, Journal of the European Ceramic Society 35 (2015) 37-45.

[53] X.H. Wang, Y.C. Zhou. Intermediate-temperature oxidation behavior of Ti2AlC in air, Journal of Materials Research 17 (2002) 2974-2981.

[54] Z.J. Wei, H.W. Wang, W.B. Fang, S.Y. Zeng. Oxidation behavior of Ti2AlC/TiAl composites, Transactions of Nonferrous Metals Society of China (English Edition) 13 (2003) 218-222.

[55] Y. Yue, H. Yin, Y. Qu, T. Su, H. Wu. Study on the oxidation properties of Ti2AlC/TiAl composites at high temperatures, Xiyou Jinshu Cailiao Yu Gongcheng/Rare Metal Materials and Engineering 36 (2007) 853-856.

[56] Z.J. Lin, M.S. Li, J.Y. Wang, Y.C. Zhou. Influence of water vapor on the oxidation behavior of Ti3AlC2 and Ti2AlC, Scripta Materialia 58 (2008) 29-32.

[57] Y.L. Yue, N. Zhao, X.F. Jiang, Y. Li, H.T. Wu, M. Wen. Oxidation resistance of Ti2AlC/TiAl composite by rapid heat treatment, Cailiao Rechuli Xuebao/Transactions of Materials and Heat Treatment 30 (2009) 6-9.

[58] M. Sonestedt, J. Frodelius, M. Sundberg, L. Hultman, K. Stiller. Oxidation of Ti2AlC bulk and spray deposited coatings, Corrosion Science 52 (2010) 3955-3961.

[59] G.M. Song, S.B. Li, C.X. Zhao, W.G. Sloof, S. van der Zwaag, Y.T. Pei, J. De Hosson. Ultra-high temperature ablation behavior of Ti2AlC ceramics under an oxyacetylene flame, Journal of the European Ceramic Society 31 (2011) 855-862.

[60] H. Zhu, X. Qian, H. Wu, J. Lei, Y. Song, X. He, Y. Zhou. Cyclic oxidation of ternary layered Ti2AlC at 600-1000°C in air, International Journal of Applied Ceramic Technology 12 (2015) 403-410.

[61] A.G. Zhou, M.W. Barsoum, S. Basu, S.R. Kalidindi, T. El-Raghy. Incipient and regular kink bands in fully dense and 10 vol.% porous Ti 2AlC, Acta Materialia 54 (2006) 1631-1639.

[62] M.W. Barsoum, T. Zhen, A. Zhou, S. Basu, S.R. Kalidindi. Microscale modeling of kinking nonlinear elastic solids, Physical Review B - Condensed Matter and Materials Physics 71 (2005) 1-8.

[63] M.W. Barsoum, M. Radovic, T. Zhen, P. Finkel, S.R. Kalidindi. Dynamic elastic hysteretic solids and dislocations, Physical Review Letters 94 (2005) 1-4.

[64] S.R. Kalidindi, T. Zhen, M.W. Barsoum. Macroscale constitutive modeling of kinking nonlinear elastic solids, Materials Science and Engineering A 418 (2006) 95-98.

[65] A.G. Zhou, S. Basu, G. Friedman, P. Finkel, O. Yeheskel, M.W. Barsoum. Hysteresis in kinking nonlinear elastic solids and the Preisach-Mayergoyz model, Physical Review B - Condensed Matter and Materials Physics 82 (2010).

[66] A. Zhou, M.W. Barsoum. Nonlinear elastic deformation of MAX phases, Key Engineering Materials 434-435 (2010) 149-153.

[67] C. Zener. The macro-mechanism of fracture, Fracturing of Metals (1948) 3.

[68] A. Stroh. The formation of cracks in plastic flow. II, Proceedings of the Royal Society of London. Series A. Mathematical and Physical Sciences 232 (1955) 548-560.

[69] A. Stroh. The formation of cracks as a result of plastic flow, Proceedings of the Royal Society of London. Series A. Mathematical and Physical Sciences 223 (1954) 404-414.

[70] J.B. Walsh. The effect of cracks on the uniaxial elastic compression of rocks, Journal of Geophysical Research 70 (1965) 399-411.

[71] B.R. Lawn, D.B. Marshall. Nonlinear stress-strain curves for solids containing closed cracks with friction, Journal of the Mechanics and Physics of Solids 46 (1998) 85-113.

[72] J.W. Hutchinson. Elastic- plastic behavior of polycrystalline metals and composites, Proc Roy Soc Ser A Math Phys Sci 319 (1970) 247-272.

[73] P. Turner, C. Tomé, C. Woo. Self-consistent modelling of nonlinear visco-elastic polycrystals: an approximate scheme, Philosophical Magazine A 70 (1994) 689-711.

[74] P.A. Turner, C.N. Tomé. A study of residual stresses in Zircaloy-2 with rod texture, Acta Metallurgica Et Materialia 42 (1994) 4143-4153.

[75] J.D. Eshelby. The determination of the elastic field of an ellipsoidal inclusion, and related problems, Proceedings of the Royal Society of London. Series A. Mathematical and Physical Sciences 241 (1957) 376-396.

[76] J. Eshelby. The elastic field outside an ellipsoidal inclusion, Proceedings of the Royal Society of London. Series A, Mathematical and Physical Sciences (1959) 561-569.

[77] S. Amini, C. Ni, M.W. Barsoum. Processing, microstructural characterization and mechanical properties of a Ti2AlC/nanocrystalline Mg-matrix composite, Composites Science and Technology 69 (2009) 414-420.

[78] M.W. Barsoum, T. Zhen, A. Zhou, S. Basu, S.R. Kalidindi. Microscale modeling of kinking nonlinear elastic solids, Phys. Rev. B 71 (2005).

[79] L. Hu, R. Benitez, S. Basu, I. Karaman, M. Radovic. Processing and characterization of porous Ti 2AlC with controlled porosity and pore size, Acta Materialia 60 (2012) 6266-6277.

[80] P. Gudlur, A. Forness, J. Lentz, M. Radovic, A. Muliana. Thermal and mechanical properties of Al/Al 2O 3 composites at elevated temperatures, Materials Science and Engineering A 531 (2012) 18-27.

[81] M. Radovic, E. Lara-Curzio, L. Riester. Comparison of different experimental techniques for determination of elastic properties of solids, Materials Science and Engineering A 368 (2004) 56-70.

[82] K. Flynn, M. Radovic. Evaluation of defects in materials using resonant ultrasound spectroscopy, Journal of Materials Science 46 (2011) 2548-2556.

[83] F. Barcelo, S. Doriot, T. Cozzika, M. Le Flem, J.L. Béchade, M. Radovic, M.W. Barsoum. Electron-backscattered diffraction and transmission electron microscopy study of post-creep Ti3SiC2, Journal of Alloys and Compounds 488 (2009) 181-189.

[84] Z.J. Lin, M.J. Zhuo, Y.C. Zhou, M.S. Li, J.Y. Wang. Microstructural characterization of layered ternary Ti2AlC, Acta Materialia 54 (2006) 1009-1015.

[85] P. Wang, B.-c. Mei, X.-l. Hong, W.-b. Zhou. Synthesis of Ti2AlC by hot pressing and its mechanical and electrical properties, Transactions of Nonferrous Metals Society of China 17 (2007) 1001-1004.

[86] Y. Bai, X. He, Y. Li, C. Zhu, S. Zhang. Rapid synthesis of bulk Ti2AlC by self-propagating high temperature combustion synthesis with a pseudo-hot isostatic pressing process, Journal of Materials Research 24 (2009) 2528-2535.

[87] A. Kontsos, T. Loutas, V. Kostopoulos, K. Hazeli, B. Anasori, M.W. Barsoum. Nanocrystalline Mg-MAX composites: Mechanical behavior characterization via acoustic emission monitoring, Acta Materialia 59 (2011) 5716-5727.

[88] J. Zhu, R. Pan. Synthesis and mechanical properties of (Ti, Mo)2AlC/Al 2O3 composite by a reaction hot pressing method, Ceramics International 39 (2013) 5609-5613.

[89] A. Ganguly, T. Zhen, M.W. Barsoum. Synthesis and mechanical properties of Ti3GeC2 and Ti3(SixGe1-x)C2 (x = 0.5, 0.75) solid solutions, Journal of Alloys and Compounds 376 (2004) 287-295.

[90] W. Yu, V. Gauthier-Brunet, T. Cabioc'H, S. Dubois. Synthesis and microstructural characterization of substoichiometric Ti 2Al(CxNy) solid solutions and related Ti 2AlCx and Ti2AlN end-members, Journal of the American Ceramic Society 97 (2014) 2308-2313.

[91] B. Mei, W. Zhou, J. Zhu, X. Hong. Synthesis of high-purity Ti2AlC by Spark Plasma Sintering (SPS) of the elemental powders, Journal of Materials Science 39 (2004) 1471-1472.

[92] W.B. Zhou, B.C. Mei, J.Q. Zhu, X.L. Hong. Rapid synthesis of Ti2AlC by spark plasma sintering technique, Materials Letters 59 (2005) 131-134.

[93] P. Wang, B. Mei, X. Hong, J. Zhu, W. Zhou. Fabrication of Ti2AlC by spark plasma sintering from elemental powders and thermodynamics analysis of Ti-Al-C system, Journal Wuhan University of Technology, Materials Science Edition 22 (2007) 325-328.

[94] A. Zhou, C.A. Wang, Z. Ge, L. Wu. Preparation of Ti3AlC2 and Ti2AlC by self-propagating high-temperature synthesis, Journal of Materials Science Letters 20 (2001) 1971-1973.

[95] Y. Bai, X. He, C. Zhu, G. Chen. Microstructures, electrical, thermal, and mechanical properties of bulk Ti 2 AlC synthesized by self-propagating high-temperature combustion synthesis with pseudo hot isostatic pressing, Journal of the American Ceramic Society 95 (2012) 358-364.

[96] Y. Bai, H. Zhang, X. He, C. Zhu, R. Wang, Y. Sun, G. Chen, P. Xiao. Growth morphology and microstructural characterization of nonstoichiometric Ti2AlC bulk synthesized by self-propagating high temperature combustion synthesis with pseudo hot isostatic pressing, International Journal of Refractory Metals and Hard Materials 45 (2014) 58-63.

[97] H. Gao, M. O'Neal, M. Radovic. Reaction Spark Plasma Sintering of Ti2AlC from Ti, Al and TiC, in preparation.

[98] M.A. Pietzka, J.C. Schuster. Summary of constitutional data on the Aluminum-Carbon-Titanium system, Journal of Phase Equilibria 15 (1994) 392-400.

[99] P. Finkel, A.G. Zhou, S. Basu, O. Yeheskel, M.W. Barsoum. On the observation of acousto-elastic hysteresis in kinking nonlinear elastic solids. AIP Conference, vol. 1096. Chicago, IL, 2009. p.231-237.

[100] R. Benitez, W. Hao, H. Gao, M. O'Neal, G. Proust, M. Radovic. Room temperature stress-strain hysteresis in Ti_2AlC revisited, (2015) submitted to Acta Materiala.

[101] N.V. Tzenvo, M.W. Barsoum. Synthesis and characterization of Ti3AlC2, Journal of the American Ceramic Society 83 (2000) 825-832 CTX: Correction. v883 no826 p1551 Je 2000.

[102] M.H. Yoo, C.L. Fu. Physical constants, deformation twinning, and microcracking of titanium aluminides, Metallurgical and Materials Transactions A: Physical Metallurgy and Materials Science 29 (1998) 49-63.

[103] S. Shu, B. Xing, F. Qiu, S. Jin, Q. Jiang. Comparative study of the compression properties of TiAl matrix composites reinforced with nano-TiB 2 and nano-Ti 5Si 3 particles, Materials Science and Engineering A 560 (2013) 596-600.

[104] G.P. Bei, A. Guitton, A. Joulain, V. Brunet, S. Dubois, L. Thilly, C. Tromas. Pressure-enforced plasticity in MAX phases: From single grain to polycrystal investigation, Philosophical Magazine 93 (2013) 1784-1801.

[105] J.a. Pelleg. Mechanical properties of ceramics, Cham Switzerland : Springer, 2014.

[106] T.H. Courtney. Mechanical behavior of materials, Boston : McGraw Hill, Boston, 2000.

[107] J.B. Wachtman, W.R. Cannon, M.J. Matthewson. Dislocations and Plastic Deformation in Ductile Crystals. Mechanical Properties of Ceramics. John Wiley & Sons, Inc., 2009. pp. 333-356.

[108] M.A. Meyers, K.K. Chawla. Mechanical behavior of materials, Cambridge, UK ; New York : Cambridge University Press, 2009. 2nd ed., 2009.

[109] N.J. Petch. The cleavage strength of polycrystals, J. Iron Steel Inst. 174 (1953) 25-28.

[110] E.O. Hall. The deformation and ageing of mild steel: III Discussion of results, Proceedings of the Physical Society. Section B 64 (1951) 747-753.

[111] N.J. Petch. Metallographic aspects of fracture, Fracture 173 (1968) 376-420.

[112] M.F. Ashby. Deformation of plastically non-homogeneous materials, Phil Mag 21 (1970) 399-424.

[113] M.A. Meyers, E. Ashworth. Model for the effect of grain size on the yield stress of metals, Philos Mag A 46 (1982) 737-759.

[114] R.W. Davidge. Mechanical behaviour of ceramics, Cambridge ; New York : Cambridge University Press, 1979., 1979.

[115] M.W. Barsoum, L. Farber, I. Levin, A. Procopio, T. El-Raghy, A. Berner. High-resolution transmission electron microscopy of Ti4AlN3, or Ti3Al2N2 revisited, Journal of the American Ceramic Society 82 (1999) 2545-2547.

[116] B.J. Kooi, R.J. Poppen, N.J.M. Carvalho, J.T.M. De Hosson, M.W. Barsoum. Ti3SiC2: A damage tolerant ceramic studied with nano-indentations and transmission electron microscopy, Acta Materialia 51 (2003) 2859-2872.

[117] R. Benitez, H. Gao, M. O'Neal, P. Lovelace, I. Karaman, M. Radovic. Effects of microstructure on the mechanical properties of Ti2AlC, (2015) in submission.

[118] P. Duvai, M.F. Ashby, I. Anderman. Rate-controlling processes in the creep of polycrystalline ice, Journal of Physical Chemistry 87 (1983) 4066-4074.

[119] D.T. Wan, L.F. He, L.L. Zheng, J. Zhang, Y.W. Bao, Y.C. Zhou. A new method to improve the high-temperature mechanical properties of Ti3SiC2 by substituting Ti with Zr, Hf, or Nb, Journal of the American Ceramic Society 93 (2010) 1749-1753.

[120] M. Radovic, M.W. Barsoum, T. El-Raghy, S.M. Wiederhorn. Tensile creep of coarse-grained Ti3SiC2 in the 1000-1200°C temperature range, Journal of Alloys and Compounds 361 (2003) 299-312.

[121] M.W. Barsoum, M. Radovic, P. Finkel, T. El-Raghy. Ti3SiC2 and ice, Applied Physics Letters 79 (2001) 479-481.

[122] Z.F. Zhang, Z.M. Sun. Shear fracture behavior of Ti3SiC2 induced by compression at temperatures below 1000 °C, Materials Science and Engineering A 408 (2005) 64-71.

[123] W. Tian, Z. Sun, H. Hashimoto, Y. Du. Compressive deformation behavior of ternary compound Cr2AlC, Journal of Materials Science 44 (2009) 102-107.